IMPERIAL COLLEGE LONDON

AN INVESTIGATION OF HOT FORMING QUENCH PROCESS FOR AA6082 ALUMINIUM ALLOYS

A thesis submitted to Imperial College London for the degree of

Doctor of Philosophy

By

MOHAMED SAAD KAMEL MOHAMED

Department of Mechanical Engineering

Imperial College London

London SW7 2AZ

2010

Synopsis

This thesis is concerned with the mechanical properties and microstructure evolution during the novel solution Heat treatment Forming cold die Quenching (HFQ) process. HFQ is a hot sheet forming technology which incorporates the forming and quenching stages to produce high strength and high precision Al-alloy sheet parts. The work in the thesis divided into three main sections: Firstly, viscoplastic behaviour of AA6082 at different deformation temperatures and strain rates was identified through analysis of a programme of hot tensile tests. Based on the results from the hot tensile tests, a set of unified viscoplastic-damage constitutive equations was developed and determined for AA6082, providing a good agreement with the experimental results. SEM tests were carried out to investigate the damage nucleation and failure features of the AA6082 during hot forming process and the results are discussed.

Secondly, the viscoplastic-damage constitutive equations were implemented into the commercial software ABAQUS via the user defined subroutine VUMAT for the forming process simulation. An experimental programme was designed and testing facilities were established for the validation of the FE process modelling results. A fairly good agreement between the process simulation and the experimental results was achieved. This confirms that the established FE process simulation model can be used for hot stamping of AA6082 panel parts. Further process modelling work was carried out to identify the optimal forming parameters for a simplified representation of a panel part.

Finally, a precipitation hardening model was developed to predict the post-ageing strength of AA6082 panel parts, having varying amounts of forming-induced plastic strain. The model was tested against results of experiments which were carried out to

investigate the effect of pre-deformation on the ageing kinetics of AA6082. The model is shown to fit and can be used to explain changes in the strength of the material. This set of equations was implemented in the VUMAT, in combination with the viscoplastic damage constitutive equation set, to model the whole HFQ process. The FE model was tested with experimental ageing and hardness results providing good agreements, which are discussed in light of the future development of the HFQ process.

Acknowledgements

I would like to express my gratitude to my supervisor **Prof. Jianguo Lin** for supervising my research and for his constant interest throughout the work and superb guidance and endless patience. His guidance, encouragement, and assistance have been a great help and I am indebted to him for providing the opportunity for me to develop the research presented in this dissertation.

I wish to express my gratitude to Dr. Alistair Foster; he has always been available for suggestion and advice during several steps of the research. I thank also my colleagues in my office for their support, advice, and encouragement.

I would like to express my thanking to my country Egypt for providing a scholarship for my PHD studies.

A heartfelt thank to my wife, my daughter and my mother for their patience and support throughout my study in UK.

Table of Contents

List of Figures

List of Tables

Nomenclature

- $A\#$ Material constants
- $B\#$ Material constants
- $C\#$ Material constants
- C_{ageing} Dislocation recovery parameter during ageing
- D Damage parameter
- D_1 Damage constants
- D_2 Damage constants
- d_1 Damage constants
- d_2 Damage constants
- d_3 Damage constants
- E Young's modulus (MPa)
- H dislocation/precipitates interaction modifying factor
- I Stress Invariant
- K Drag Stress (MPa)
- Q_x Activation energies ($kJ \times mol$)
- R Isotropic strain hardening (MPa)
- R_g Universal gas constant
- P Applied pressure
- T Temperature (°K unless stated as °C)
- T_m Material melting point (°C)
- t_{p_o} Peak time for undeformed sample
- k Initial yield stress (MPa)
- $k\#$ Material constants

- $n\#$ Material constant exponents
- σ Stress (MPa)
- ε_T Total equivalent strain
- ε_p Plastic equivalent strain
- ε_e Elastic equivalent strain
- ε_f Fracture strain
- $\bar{\rho}$ Normalised, averaged dislocation density
- f_r Precipitates relative Volume fraction
- f_d Damage parameter for current study
- r Precipitates average radius
- r_o Precipitates initial nuclei radius
- r_c Precipitates critical radius
- r_{co} Precipitates critical radius of undeformed sample
- r_d damage void radius
- $\gamma_\#$ Material constants
- σ_{ss} Solid solution strength
- σ_{ss0} Solution contribution in the as-quenched condition
- α Fraction of the initial solute concentration
- $\dot{\sigma}_{(ppt)sh}$ Shearable Precipitation strength
- $\dot{\sigma}_{(ppt)nsh}$ Non-shearable Precipitation strength
- σ_{dis} Dislocation strength
- σ_Y Yield strength
- HV Vickers hardness
- σ Flow stress
- σ_v Visco stress

- σ_e Equivalent stress (MPa)
- σ_H Hydrostatic stress (MPa)
- σ_1 Maximum principal stress (MPa)

Chapter 1

Introduction

1.1 Automotive lightweight requirements

The choice of material for the manufacturing of the automotive components for passenger vehicles is very crucial and is influenced by many factors. The first concerns the fuel efficiency of passenger vehicles. The Corporate Average Fuel Economy (CAFE) programme was established by The Energy Policy Conservation Act to improve the efficiency of light-duty vehicles (NHTSA, 1990; Sulaiman, 2005). This policy requires the vehicle manufacturers to meet the standard in miles per gallon (mpg) for the vehicles they produce each year. The National Highway and Traffic Safety Administration (NHTSA) found that the fuel efficiency of passenger cars after 1990 was 27.5 miles per gallon (NHTSA, 1990; Sulaiman, 2005). This level of the fuel efficiency is expected to increase further due to increasing demand for crude oil and reducing oil reserves. Automotive industrial manufacturers are normally required to add more structural elements, such as thicker body side panels, cross members, and crumple zones in order to make passenger vehicles stronger and safer. In turn, this increases the weight of automotive components. However, fuel economy is distinctly improved by reducing a vehicle's weight. Thus there is a tendency towards manufacturing lightweight vehicles that has realized fuel savings within a short period. Lightweight vehicles also provide better acceleration without increasing the engine's output, and

improve braking performance. Therefore, the production of lightweight vehicles is an important technical solution for improving performance and enhancing their appeal and this has become the second factor for material selection in automotive components (NHTSA, 1990; Burger et al., 1995; Cole and Sherman, 1995; Miller et al., 2000).

The third factor that must be considered in automotive industrial design is environmental pollution from motor vehicle's emissions. The importance of that can be seen in the fact that motor vehicles emit more than half of the carbon monoxide produced in the United States (NHTSA, 1990; Sulaiman, 2005). These emissions, including microscopic particles, can lead to breathing and heart problems. The pollution control agencies in the United States have acted with the environmental protection agency to reduce motor vehicle pollution (NHTSA, 1990). Hence, future vehicles must consume a smaller amount of fuel in order to achieve future emission targets. To reduce emissions, it is not only important to develop low emission engines, but also to use them in the most rational way possible. Reducing weight by using lightweight materials such as aluminium is a good way of reducing CO emissions from road transport (NHTSA, 1990; Sulaiman, 2005).

Materials chosen for use in the automotive industry must not only have economies of scale and high formability, they must also be strong enough to meet several automotive requirements. The contradictory demands mentioned in the previous paragraphs have forced automotive manufacturers to adopt the following strategies with regard to material selection for automotive construction, the materials must:

- be lightweight with less density to achieve fuel efficiency and reduce vehicle's emissions (NHTSA, 1990; Burger et al., 1995; Miller et al., 2000).

- have good formability and high corrosion resistance (Burger et al., 1995; Miller et al., 2000).
- be strong structurally (Burger,et al., 1995; Sulaiman, 2005).
- have economies of scale and good recyclability (Burger, et al., 1995; Miller et al., 2000).
- While materials play an influential role in terms of the quality and cost of a car, the selection of proper materials is of vital importance. Nowadays, the materials for constructing vehicles are selected to fulfil requirements in an optimal way (Wilhelm, 1993). The application potential of selected materials depends on how the materials can fulfil the requirements demanded of them (Wilhelm, 1993).

Steel has been the material of choice used to build vehicles since the 1920s (Sulaiman, 2005). However, the requirements mentioned above have become increasingly more important in the last ten years, and the automotive industry has been very cautious in fulfilling them. For example, the basic requirement for automobile sheet to deform the panel part is to have high formability, while the strength is increases when the part is painted and thermally cured. Steel is the material of choice because it has the range of formability required and it is relatively cheap compared to other ferrous or nonferrous sheet metal. In addition, after the hot-dip galvanneal coating process, it becomes resistant to corrosion (Miller et al., 2000; Sulaiman, 2005). Steel families have been used largely based on formability, cost and strength. However, there are limits to fulfilling the above requirements, particularly in terms of vehicle weight reduction (Miller et al., 2000; Sulaiman, 2005). It is essential to achieve vehicle weight reduction without reducing its size and carrying capacity, so that it will be acceptable to

consumers (Miller et al., 2000). This can be achieved by reducing the weight of automotive structures and exterior panels.

Nowadays, aluminium has emerged as the principal material for the automotive industry because of a number of advantages it has over other competitive materials (Sulaiman, 2005), including:

- Relatively lightweight;
- Relatively high tensile, compression and shear strengths;
- High specific strength (strength to weight ratio);
- High corrosion resistance;
- Ease of fabrication; and
- Recyclable.

The replacement of steel with aluminium alloys achieves a direct vehicle weight reduction of up to approximately 47% (Sulaiman, 2005; Abedrabbo et al., 2006). Further weight savings can be achieved because the lower loads in turn allow the use of lightweight components in the brakes, suspension and engine without any detrimental effect on performance. Although the density of aluminium is one third lower than that of steel, it has only a third of the strength and elastic modulus (Kleiner et al., 2003; Kleiner et al., 2006). It is vital that the use of lightweight material does not decrease the properties of the components, the specific material properties of which are shown in Table 1.1 (Kleiner et al., 2003; Kleiner et al., 2006), these should be taken into account.

Table 1-1 Materials Properties (Kleiner et al., 2003).

property	Al	Steel
Density (kg m^{-3})	2.8	7.83
Young's modulus (GPa)	70	210
Tensile strength (N mm^{-2})	150-680	300-1200
Specific strength	54-243	38-153
Specific stiffness	25	26.8

Aluminium will play a significant role in future car generations as its material properties have many advantages and open the way for new applications in the automotive industry (Hodkinson and Fenton, 2000; Kleiner et al., 2003; Sulaiman, 2005; Kleiner et al., 2006; Jeswiet et al., 2008). Indeed, developments in the aluminium industry, including improving the mechanical properties of aluminium alloys by adding various alloying elements has opened a wide field of applications for these alloys, particularly in the automotive and aerospace industries (Hodkinson and Fenton, 2000; Kleiner et al., 2003).

The application of aluminium alloy in the automotive industry has increased more than 80% in the past 5 years (Miller et al., 2000). In 1996 a total of 110 kg of aluminium alloys were used in a vehicle (Miller et al., 2000). This amount is predicted to increase to 250 or 340 kg regardless of the structural applications (Miller et al., 2000). The development of aluminium consumption for automotive applications in Europe increased significantly from 675 kton in 1994 to 1900 kton in 2005, as shown in Figure

1.1 (Miller et al., 2000). Typical uses of aluminium castings for various automobile parts have been increasing for a long time. The material for engine blocks has changed from cast iron to aluminium, resulting in a significant weight reduction (Miller et al., 2000). Aluminium castings are also used for about 100% of pistons, 75% of cylinder heads, and 85% of intake manifolds and transmission in the automotive power train. They are used for chassis applications, about 40% of wheels, and for brackets, brake components, suspension (control arms, supports), steering components (air bag supports, steering shafts, housings, wheels) and instrument panels.

New developments in aluminium alloys have opened a wide range of applications of wrought aluminium in place of aluminium castings. Wrought aluminium alloys are produced from cast ingots which are prepared for subsequent mechanical processing (Polmear, 1995). The microstructures and mechanical properties of wrought aluminium alloys are significantly dependent on various working operations and thermal treatments. For automotive applications, the most used aluminium alloy series is the non-heat treatable Al-Mg (AA5xxx series) and the heat-treatable Al-Mg-Si (AA6xxx series) alloys. Due to the variations in chemical composition and processing, AA5xxx are optimized for strength and corrosion resistance in vehicle chassis and AA6xxx are optimized for high formability and age hardening response in autobody sheets panels. The current 6xxx alloys used for autobody sheets are AA6016 and AA6111 and, more recently, AA6181 and AA6082 were added for recycling aspects. AA6111 and AA6082 are usually used for the outer body panels which combine high strength with good formability (Hodkinson and Fenton, 2000). Applications of wrought aluminium alloys in the automotive industry have achieved vehicle weight reductions of up to 50% compared to the use of steel constructions (Hodkinson and Fenton, 2000; Miller et al., 2000; Kleiner et al., 2003; Kleiner et al., 2006; Sulaiman, 2005; Kleiner et al., 2006;

Jeswiet et al., 2008). The applications of wrought aluminium alloys in the automotive components of a passenger car are shown in Figure 1.2 (Miller et al., 2000). Impact energy absorption behaviour and good deep drawing are the most important factors for choosing the material in structural sheet applications (Miller et al., 2000). However, for skin sheet material, achieving good formability and strength after the paint-bake are the most important properties. Therefore, the age hardening 6xxx alloys are the primary choice for these applications (Polmear, 1995; Miller et al., 2000).

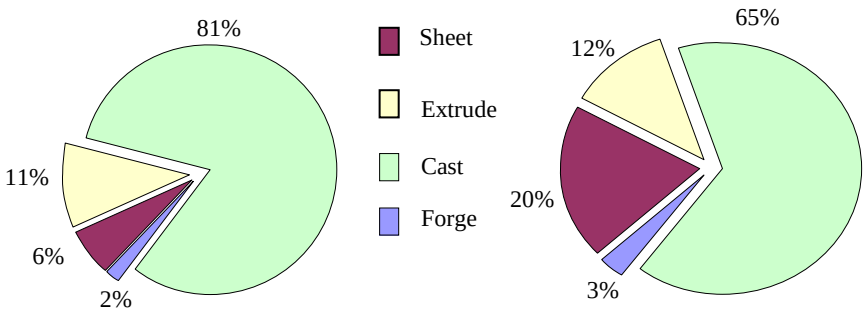

Figure 1-1 Development of aluminium consumption for application in Europe (Miller et al., 2000).

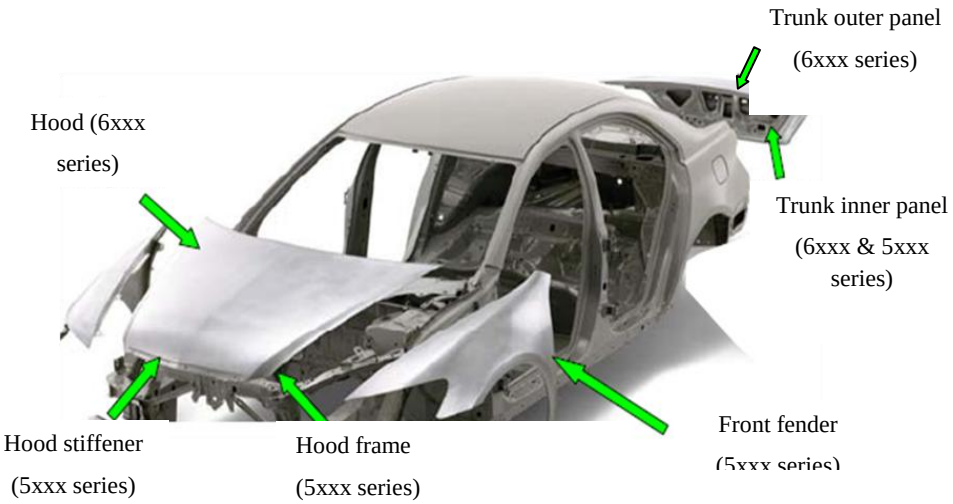

Figure 1-2 Applications of aluminium alloys in the automotive components of a typical passenger car (www.autoaluminum.org).

1.2 Forming of aluminium alloy panel components

Automotive body panels are traditionally made from cold-rolled steel sheet. In the past few years, automotive manufacturers have attempted to use AA6xxx aluminium alloys in manufacturing automotive components in order to reduce the weight of their models. Age hardened aluminium alloy sheet components are normally cold, formed either in the T4 condition (solution heat treated and quenched), followed by artificial ageing for higher strength, or in the T6 condition (solution heat treated, quenched and artificially aged). Figure 1.3 shows the temperature profile for material preparation and for traditional forming methods of automotive panels. In this process, the material is heated to its Solution Heat Treatment (SHT) temperature and then held for a sufficient period of time, and all precipitates are taken into the matrix giving one single phase. The heat-treated material is rapidly cooled to room temperature to freeze this super-saturated state within the material. Once the material has been thermally treated and modified to the required mechanical properties, it is cold-deformed in the T6 condition into the required shape (Foster et al., 2008).

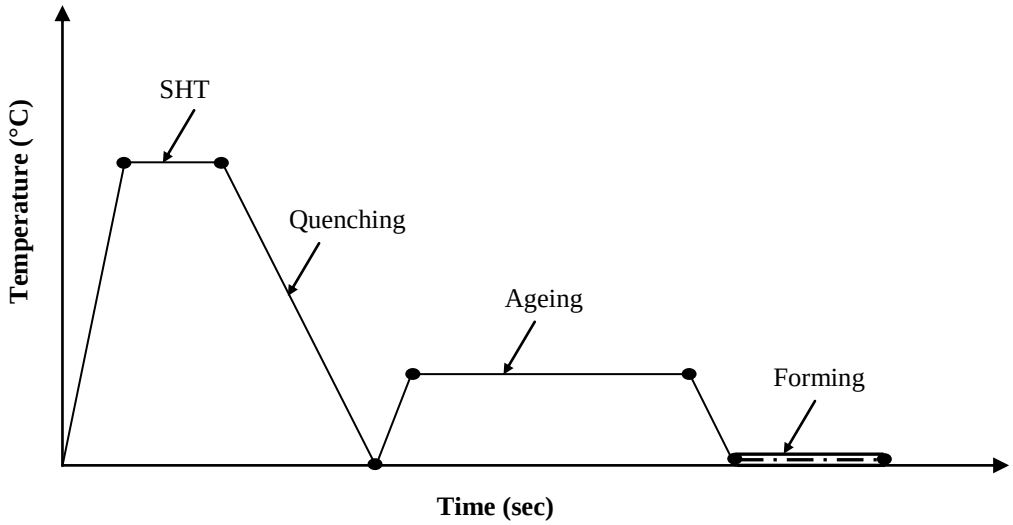

Figure 1-3 Temperature profile for the traditional forming method of automotive panels.

The advantages of the traditional method are:

- The process is relatively simple, and the equipment needed for the process is readily available.
- The separation of the material processing and forming stages means the material supplier can fully prepare the material before it goes to locations where components are formed.
- The die is relatively in expensive, since there is no temperature control requirement.

The disadvantages of the traditional method are:

- The formability of the material is very low due to the hardening and strengthening processes carried out on the material, even in T4 forming, as shown in Figure 1.4, and T6 forming (Foster, 2008).
- After forming, if young's modulus is low, the component is more likely to be affected by springback and wrinkling problems. This means extra effort is needed to compensate for these problems.
- The presswork can also cause unwanted changes in the microstructure and hence adversely affect the material properties of the material.
- The use of a separate process also means the total cost of the component may be greater due to the extra equipment, workforce and time needed throughout the stage.

Figure 1-4 Low formability of cold forming T4 Al-alloy in a hemispherical punch test (Foster, 2008).

These disadvantages are also encountered in forming engineering components using other materials. In an effort to overcome them, various efforts have been made and special processes have been invented to address particular problems in forming specific types of components.

It is generally accepted that the ductility of the aluminium alloys is obtained from the SHT stage (T4 treatment), however, the strength is obtained from the ageing stage (T6 treatment) (Garrett et al., 2005; Mohamed et al., 2008). The typical solution of the ductility problem when manufacturing such components as automotive panels is hot forming. At high temperature the flow stress is decreased and in turn the required forming force is decreased, however, the ductility of the material is increased. As more and more sheet metal blanks of aluminium alloys are used to reduce the product weight, the formability limits can be extended by increasing forming temperature (Garrett et al., 2005; Mohamed et al., 2008). In the hot forming process, the material is heated to

deform the component, and then heat treatment is carried out on the deformed component. Some distortion is caused after the heat treatment for the features of the deformed component. Therefore, the component is taken for another deforming stage and, finally, the deformed heat treated component will be hardened throughout the ageing stage.

The advantages of this method are:

- High formability can be achieved.
- Low springback is achieved.

The disadvantages of this method are:

- Distortion is caused after heat treatment of the deformed component.
- The extra forming stage increases the cost of manufacturing the component.
- The shape accuracy of the deformed component is not good enough.
- The second forming process, i.e. the presswork can cause unwanted changes to the microstructure and hence adversely affect the material properties after ageing.

1.3 Introduction to the HFQ process

To overcome all of the above problems, a novel process, known as solution Heat treatment Forming and cold die Quenching (HFQ) has been developed. In this process the forming and quenching processes are combined together in one stage. This process can be used for forming complex-shaped components in one operation with high strength as well.

The thermal profile of the newly developed HFQ process is shown in Figure 1.5. The aluminium blank is first heated to its SHT temperature (e.g. 525°C for AA6082) and subsequently held at the solution heat treatment (SHT) temperature for a specified period to dissolve all precipitates in the primary α-Al matrix (Garrett et al., 2005; Mohamed et al., 2008).

The fully solution heat treated aluminium blank is then transferred to a press and formed between a set of cold dies, and subsequently held within the cold dies to quench the metal. There are two reasons for holding the formed part in the cold dies: one is that rapid quenching prevents the formation of coarse β-phase precipitates, particularly at grain boundaries; the second is to avoid thermal distortion of the formed part during quenching. The formed part is subsequently aged to enable the precipitates to be formed in a controlled way.

Increased ductility implies that increased formability can indeed be achieved by forming at high temperature. Hence, more complicated components can be manufactured, with features such as large draw depths and sharp corners. In addition, multi-part assemblies can be consolidated. The ductility, compared with traditional cold forming processes, can be increased about six times (Foster et al., 2008). The process time is significant. It is much faster (about 30-100 times faster) than superplastic forming (Foster et al., 2008).

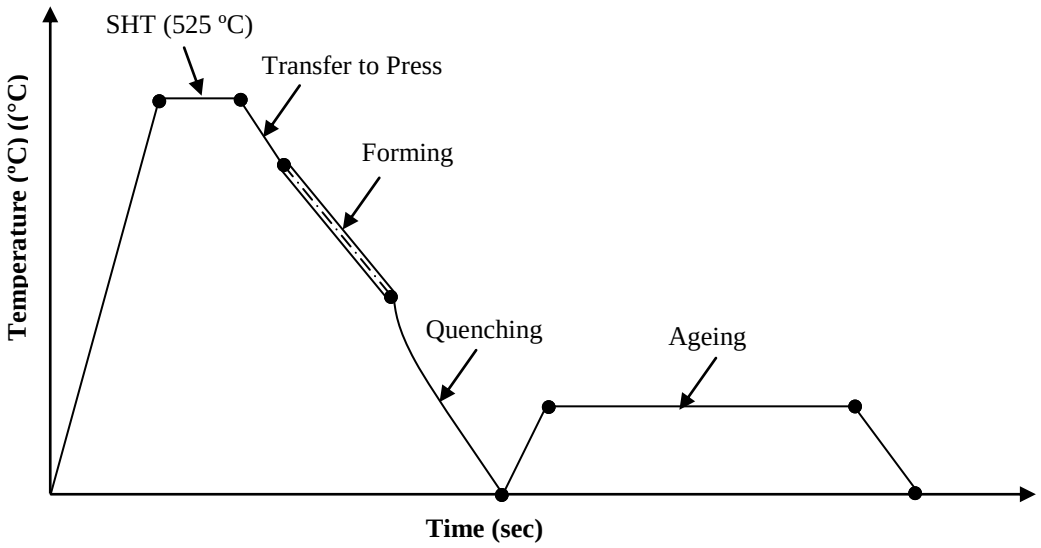

Figure 1-5 The temperature profile of a typical HFQ process.

The advantages of this novel method include:

- The reduction of the number of individual steps means there are fewer opportunities for contamination of the metal within each process, and uncontrolled air-cooling.
- Less energy is needed due to the reduction in the number of times the material is reheated.
- The formability of the material is higher, due to the hardening stages being performed during or after the forming stage.
- Springback can also be reduced by the combination of quenching and forming stages as shown in Figure 1.5. This, in turn, increases the geometrical tolerances of the component, allowing components to be assembled easily.
- Distortion of the component is also limited due to the quenching stage being contained in the cold die (Foster, 2008).

- The time of production for each component is reduced, because the component no longer has to be transferred between as many different items of process equipment. This consequently leads to financial savings.

1.4 Aims and structure of the thesis

The objective of the work reported here was to design experimental procedures and develop modelling tools to investigate and accurately describe a newly developed HFQ process, for AA6082 series aluminium alloy. To complement this, the mechanical and microstructural properties of AA6082 aluminium alloys were investigated and modelled.

The objective has been fulfilled through the completion of the targets outlined:

- Determination of the optimum thermal heat treatment process parameters in terms of SHT, quenching and ageing.
- Determination of the mechanical properties of AA6082 at different deformation and heat treatment conditions using SEM (microstructure examination) and indentation hardness tests.
- Design and setup of an experimental programme to run experimental tests, using a Gleeble materials simulator (3800 series), to evaluate the influence of HFQ parameters on the viscoplastic material response under conditions typical of the industrial process.
- Development of a set of unified viscoplastic constitutive equations based on the experimental data sets and observed microstructure features.
- Description of the experimental and numerical tools used to calibrate and validate the FE model, as implemented to simulate hot forming operations.

- Design and setup of an experimental test to investigate the sheet formability and to determine material failure features, thus determining the process window at elevated temperature.
- Development of a physically based precipitation-hardening model including the effect of pre-strain on the ageing kinetics and precipitation-hardening.
- Implementation of the precipitation hardening constitutive equations into an FE model to predict the material hardness under hot stamping conditions.

In order to achieve the above aims, the thesis should be structured to mirror the work sequences of this study. This thesis has been divided into eight chapters. The first chapter contains a short introduction of the research, the requirements for automotive lightweight manufacturing and in turn the new trends in the automotive industry. Introduction and description of the Hot Forming Quenching process as a novel process is presented in this chapter. In Chapter 2, the current and potential future forming technology contributions to the manufacture of lightweight components and structures are presented. Advanced forming techniques, including superplastic forming, hydroforming, and hot stamping and cold die quenching to achieve high formability of lightweight materials are investigated. Microstructure evolution during hot stamping and cold die quenching process is studied in order to attain the required mechanical properties of the material.

In Chapter 3, a detailed description of the experimental method designed to investigate the feasibility of the novel HFQ process for AA6082 and also includes test facility design and descriptions and test sample preparation was investigated. Chapter four contains a detailed discussion and analysis of the experimental results obtained from the experimental programme described in the Chapter three. Chapter five contains a

detailed description of formulating the viscoplastic-damage behaviour of fully solutionised AA6082 at, and below, the Solution Heat Treatment (SHT) temperature.

Chapter six contain the implementation of the constitutive equations into commercial software ABAQUS via the user defined subroutine VUMAT for the forming process simulation and process parameters optimization. The development of the precipitation hardening constitutive equations and implementation into commercial software ABAQUS via the user defined subroutine VUMAT to predict the post-strength of the AA6082 at hot stamping conditions and artificial ageing are presented in Chapter seven. Final conclusions, recommendations and future work are presented in the eighth Chapter.

Chapter 2

Advanced Forming Techniques

2.1 Introduction

This chapter contains the current and potential future forming technology contributions to the manufacture of lightweight components and structures. Lightweight materials are often associated with limited formability. Hence, there is difficulty manufacturing complex components from lightweight material. To overcome this problem, advanced forming techniques, including superplastic forming, hydroforming, and hot stamping and cold die quenching are investigated. In addition, to achieve a complex shape component, the desired material properties are very important. In order to attain the required mechanical properties of the material, microstructure evolution during the hot stamping and cold die quenching process is studied.

2.2 Manufacturing of lightweight components by metal forming

Lightweight material can be used in automotive applications in wrought and cast forms. Aluminium sheet has the potential to be used in vehicle components. In contrast to steel, aluminium has low formability particularly at room temperature and, in turn, is more difficult to stamp. Current research is exploring methods to improve the formability of aluminium alloys. There are a wide range of opportunities for using

aluminium in automotive powertrains, chassis, and body structures. An aluminium body structure may be manufactured in two ways: either stamped like a steel structure or a combination of many processes, including castings, extrusions, and stamping and welding as in a space frame (Cantor et al., 2008; Toros et al., 2008).

Automotive body panels, which consist of an outer and inner panel as a double structure, have gained increasing interest in order to reduce the vehicle weight (Cantor et al., 2008; Toros et al., 2008). The outer panels must have sufficient denting resistance. This can be achieved by using high strength materials. On the other hand, for inner panels, the material must have a high deep drawing capability to deform into more complex shapes (Cantor et al., 2008). In other words, different strategies in the development of aluminium body panels are carried out in different regions. For instance, there are different requirements for automobile manufacturing in Europe, North America and Japan. In Japan, higher formability alloys are required from automobile manufacturers. Therefore, special AA5xxx alloys, such as AA5022 and AA5023, were developed. On the other hand, high strength alloys are required in Europe and North America. Consequently, AA2xxx alloys, such as AA2036, and AA6xxx alloys, such as AA6061, AA6111 and AA6022, were developed (Cantor et al., 2008; Toros et al., 2008).

A wide range of aluminium applications are provided via extrusions. The complex shapes of automotive components can be achieved allowing a novel lightweight design with integrated functions. In Europe, completely new and flexible passenger car concepts (e.g. the aluminium space frame, Figure 2.1) (Jeswiet et al., 2008) and complex structures (e.g. chassis parts, bumpers, crash elements, etc) have been developed using aluminium extrusions. The potential of aluminium extrusion for

complex design and functional integration is suitable for cost-effective mass production. Formability and final strength of the material used for extrusion is controlled by subsequent heat treatment processes. Extrusions have been applied for bumper beams and crash element boxes (Figure 2.2) (Geiger et al., 2008), which are a major market for aluminium extrusions.

Figure 2-1 Profile based frame structure of the Ferrari F360 Modena (Kleiner et al., 2003; Kleiner et al., 2006; Jeswiet et al., 2008).

Figure 2-2 Aluminium extrusions in bumper beams and crash boxes (ArcelorMittal, 2008).

Achievements in forming technology by increasing the accuracy of curved profiles have contributed to lightweight frame structure forming. The precision of the shape profile in the conventional stretch bending can be improved by an adaptive process control. The profiles are usually over bent to accommodate springback. The springback varies due to different wall thicknesses as well as distinct treatments and quenching processes. By measuring the applied forces over the tool movement during the bending phase, material and springback behaviour can be estimated. As the springback is also determined by the axial tensile stress, an adaptation of the tensile force to the estimated springback behaviour improves the shape accuracy of the bent profile, as shown in Figure 2.3 (Miller et al., 2000; Kleiner et al., 2003).

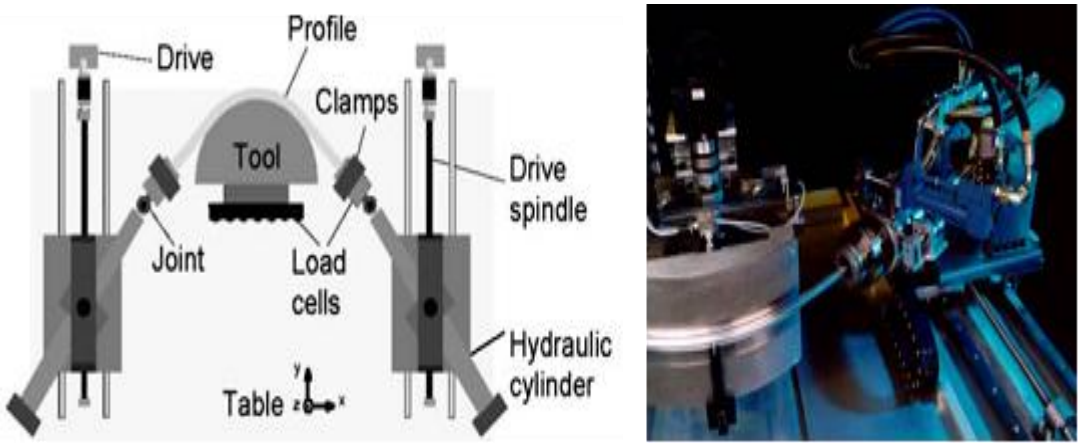

Figure 2-3 Schematic illustrations of adaptive stretch bending and the real apparatus (Miller et al., 2000; Kleiner et al., 2003).

In contrast to frame structures used for small scale production, shell structures for automotive body panels are used for large scale production. Steel is the dominant material used for shell structure components due to its cheap cost. Expensive materials, such as aluminium, are considered for replacing the steel sheet metal due to the opportunities of weight reduction. Although aluminium has the same specific strength as steel, its lower density results in a larger sheet thickness and this significantly

increases the specific dent resistance (Kleiner et al., 2003). On the other hand, with the need to decrease costs in lightweight structures, sheet metal parts have become larger. Therefore, workpieces and their forming processes are more complex and difficult, and parts with different thicknesses are joined together in the assembly to produce a single part with regions of different wall thicknesses. These parts can be used as semi-finished products, as shown in Figure 2.4 (Jeswiet et al., 2008).

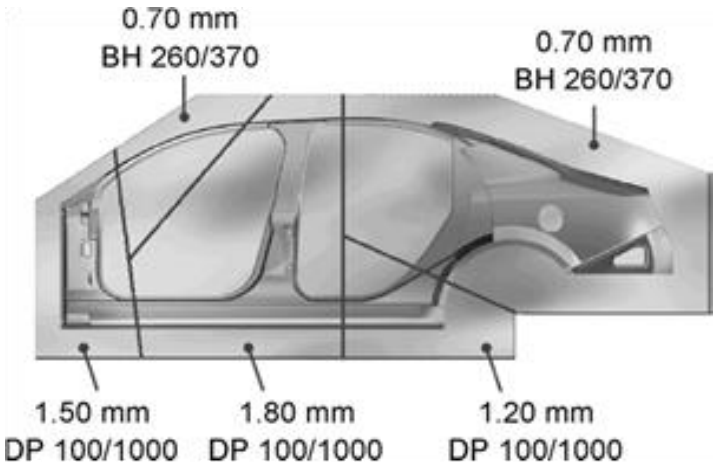

Figure 2-4 A side panel made of tailored blanks (Jeswiet et al., 2008).

2.3 Advanced techniques for achieving high formability of materials

Due to the low formability of the lightweight material, particularly at room temperature, the forming technology for this material is restricted. Therefore, advanced forming methods are needed in order to improve their formability. Al-alloy sheet components are normally cold formed either in the T4 or T6 conditions. Either

condition introduces a number of intrinsic problems, such as springback and low formability, which are difficult to solve.

As mentioned previously in Chapter 1, the usual solution for low formability problems is to deform the material at high temperatures. Increasing the temperature of the material increases ductility and also lowers the yield strength. This results in less forces being required for the deformation. Hot stamping can increase formability and reduce springback, but it destroys the desirable microstructure (Foster et al., 2008). Post-forming heat treatment (SHT) is thus required to restore the microstructure, but this will result in distortions of the formed components during quenching after SHT. These disadvantages are also encountered in forming engineering components using other sheet metals.

Various efforts have been undertaken and special processes have been invented to overcome specific problems in forming particular types of components. These are outlined in the following section.

2.3.1 Superplastic forming (SPF) of sheet metal components

Superplastic forming is a slow forming process designed to achieve a significant increase in formability. The superplastic behaviour of metals has been used to form complex shaped lightweight components, especially for aerospace applications (Serra et al., 2009). To achieve superplastic deformation fine grains equiaxed grain with average grain sizes typically around 5 μm are required. In addition, to enable the diffusion processes to occur, the temperatures in excess of 0.5 T_m are required. However, under these conditions, grain growth takes place by static diffusion controlled processes,

which can be enhanced by deformation (Serra et al., 2009). The grain growth cause the material be hard and decreases the strain-rate sensitivity and in turn decreases the elongation to failure. This is very obviously in two-phase systems, such as the titanium alloy (Ti6Al4V), the presence of the low diffusivity alpha phase, tends to constrain the growth of the higher diffusivity beta phase, thus preventing uncontrolled grain growth (Kim and Dunne, 1998).

Superplastic forming can be achieved using particular processes such as: thermoforming, blow forming, and vacuum forming. Post-forming heat treatment (e.g. SHT + Quenching + Ageing for Heat-treatable Al-alloys) is normally required to obtain an appropriate microstructure to ensure high strength (Lin et al., 2002; Khraisheh et al., 2008; Serra et al., 2009).

For aluminium alloys, the dominant deformation mechanism for this type of plastic deformation is grain rotation and grain boundary sliding (Miller et al., 2000; Kleiner et al., 2003; Foster et al., 2008; Jeswiet et al., 2008; Khraisheh et al., 2008; Serra et al., 2009). Such relative displacement of grains is accommodated by the distribution of matter within the mantle adjacent to grain boundaries (Lin et al., 2002).

The major advantage of the superplastic forming process is that large complex shapes can be deformed in one operation. The surface finish and the shape precision for the finished products are excellent. Moreover, the finished product does not suffer from springback or residual stresses (Serra et al., 2009).

However, the main disadvantage of the superplastic forming process is its slow forming rate. The forming process time varies from two minutes to a few hours. Hence, this

process is suitable only for low volume production (Serra et al., 2009).

Recently, superplasticity has been used to form components for automotive applications. In the automotive industry, aluminium alloys are deformed at a faster rate (in contrast to aerospace applications) to provide high volume production. The significant increase in the formability of aluminium alloys by using superplastic forming allows for more complex to be manufactured, as shown in Figure 2.5 (Jeswiet et al., 2008) which can, in turn, eliminate using fasteners and joints (Jeswiet et al., 2008).

Figure 2-5 Superplastic formed aluminium sheets (Jeswiet et al., 2008).

2.3.2 Hydroforming Process

Hydroforming is a manufacturing process to achieve high formability of the material. In the hydroforming process, pressure is applied to the sheet metal to form a desired

component shape. Hydroforming may be used as an alternative process to cold deep drawing (Foster et al., 2008). In contrast to tube hydroforming in which the pressure can be easily sealed, sheet hydroforming requires a rubber membrane to be used to ensure the high pressure fluid does not escape. This affects reliability and complicates tooling. The process has made a little impact in the mass-production of sheet aluminium components (Foster et al., 2008; Mohamed, 2003).

The main applications of the hydroforming process can be found in automotive industries, a specifically in exhaust parts, radiator frames, front and rear axles, engine cradles, body parts and space frames (Mohamed, 2003). The hydroforming process has been applied normally to reduce the number of required joints and increase material utilization, as shown in Figure 2.6 (Mohamed, 2003).

Figure 2-6 Conventional stamping versus tube hydroforming (Mohamed, 2003).

2.4 Development of hot stamping and cold die quenching processes

Safety critical automotive parts, such as bumper beams have conventionally been manufactured from high strength steels. Cold deformation of high strength steels can tolerate a limited volume fraction of the strength phases, such as bainite and martensite (Foster et al., 2007a). If the material includes more bainite, the ductility becomes too low, causing fracture during the forming processes. Springback is another problem in cold stamping of high strength steel, which makes it difficult to achieve the accuracy of the formed parts (Foster et al., 2007a).

A conventional bumper beam of a vehicle is bent from a flat sheet, welded, and then bent slightly into the final shape. In a bumper beam design, deep drawn beads into the cross-section are provided, as shown in Figure 2.7 (ArcelorMittal, 2008). This requires a high formability material but allows a smaller sheet thickness to be used due to higher strength and a larger cross-sectional area. At the same time, the high ductility permits absorption of more crash energy (Foster et al., 2007a). The same performance as a conventionally designed stainless steel bumper is achieved through a weight reduction of 20% attained by using AlSl 301L in cold worked condition (Foster et al., 2007a).

Figure 2-7 A high strength steel bumper beam (ArcelorMittal, 2008).

A novel forming process, known as hot stamping and cold die quenching, has been developed to address these problems (Foster et al., 2007a; ArcelorMittal, 2008). Figure 2.8 shows the hot stamping and cold die quenching process procedures for steel (Foster et al., 2007a). The novel process contains three stages, as shown in Figure 2.8: (1) the material blank is heated to an austenite temperature (e.g. 920ºC) and held for a certain short time to ensure that the material is fully transformed to austenite; (2) the sheet is transferred to a press for forming using a water cooled die set; (3) the formed part is held within the cold die set for about 10 seconds to enable rapid quenching to take place, so that the austenite is transformed to martensite - the hardest possible phase for steels. Because the formed part is held within the forming tool set during cooling, thermo-distortion can be eliminated. Springback, which is one of the difficult problems encountered in cold forming of high strength materials, can also be avoided.

The cooling rate is the critical parameter in a hot stamping and cold die quenching process. If the cooling rate obtained from cold die quenching is too slow, the materials will not sufficiently transform to martensite. Boron steel enables the material to be transformed from austenite to martensite at much lower cooling rates, typically less than 30˚C per second. Therefore, boron steel is suitable for the hot stamping cold die quenching process. An increasing number of safety critical components for passenger cars are produced using hot stamping processes, as shown in Figure 2.9 (Foster et al., 2007a; ArcelorMittal, 2008).

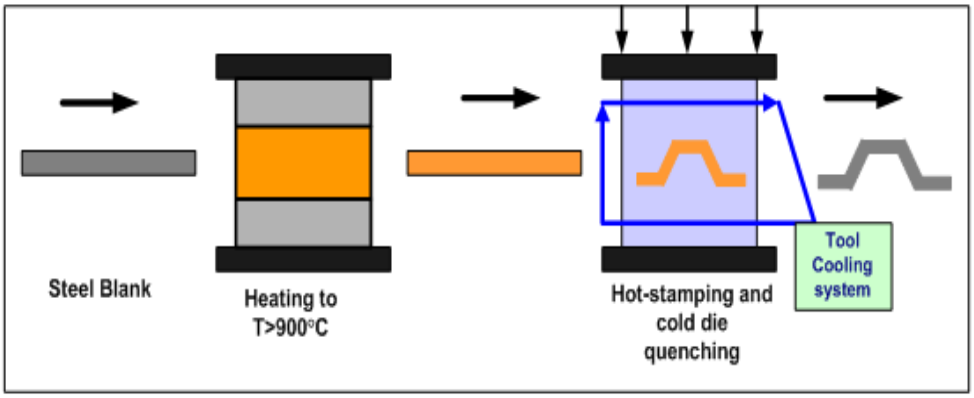

Figure 2-8 Hot stamping with cold die quenching process for steel (Foster, et al., 2007a; ArcelorMittal, 2008)

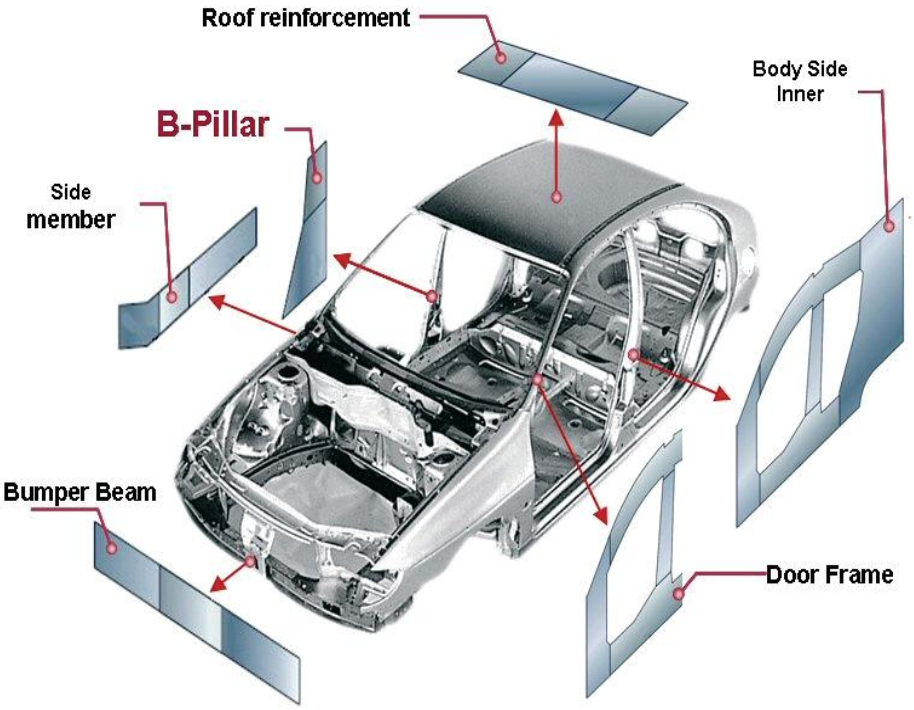

Figure 2-9 Potential applications of hot stamped laser welded blanks for several automotive applications (ArcelorMittal, 2008).

As mentioned before, aluminium will play an important role in future car generations. As a result of the developments in the aluminium industry, improving the mechanical properties of the aluminium alloys by adding various alloying elements increases the application area of these alloys in the automotive and aerospace industries (Hodkinson and Fenton, 2000; Kleiner et al., 2003). Therefore, Hot Forming and cold die Quenching can increase the formability of the aluminium alloy sheets and produce high strength and high precision Al-alloy sheet parts. From the initial investigation, it has been concluded that HFQ could be an excellent process to produce high strength, high precision, heat treatable Al-alloy sheet components and to increase the formability of leaner composition non-heat-treatable alloys.

2.5 Microstructure control

The microstructure of aluminium alloys can be controlled to provide the required properties for particular automotive applications (Toros et al., 2008). For the current study, AA6xxx, particularly AA6082, is used in the novel hot forming quenching process. This alloy contains Si and Mg as the main alloying elements. These alloying elements are partly presented in the form of intermetallic phases and partly dissolved in the primary α-Al matrix. Fe-bearing intermetallic particles such as β-Al_5FeSi and α-$Al_{12}(Fe,Mn)_3Si$ are typical of the AA6xxx alloys and have a significant influence on its formability (Mrówka-Nowotnik et al., 2005). Their morphology and nature vary depending on the chemistry and heat treatments. The brittle plate-like monoclinic β phase is associated with poor hot formability. This unfavourable effect can be improved by performing the solution heat treatment process at an elevated temperature, by which the β phase transforms to the more rounded, metastable cubic α phase (Lassance et al., 2006). Figure 2.10 shows the temperature profile illustrating the change in microstructure of AA6xxx during the hot forming quenching process.

Firstly, the material is heated to the solution heat treatment temperature. At the beginning of solution heat treatment, the solutes are presented in patches of highly concentrated precipitates of different sizes that provide barriers to dislocation flow during deformation. With time these precipitates dissolve into the matrix, diffusing throughout the whole structure (α-phase) (point X, Figure 2.10). This diffusion results in the 'flow barrier' being reduced and eliminates the chance of forming micro-voids around second phases in plastic deformation (Mrówka-Nowotnik et al., 2005; Garrett et al., 2005). This increases the ductility of the material and reduces the flow stress during hot tensile tests. If the material is held at the SHT temperature (T_{SHT}) for a certain time, this also allow such factors as irregular precipitates and residual stresses to be further reduced, giving a more homogeneous microstructure throughout the whole material, and hence a higher formability material.

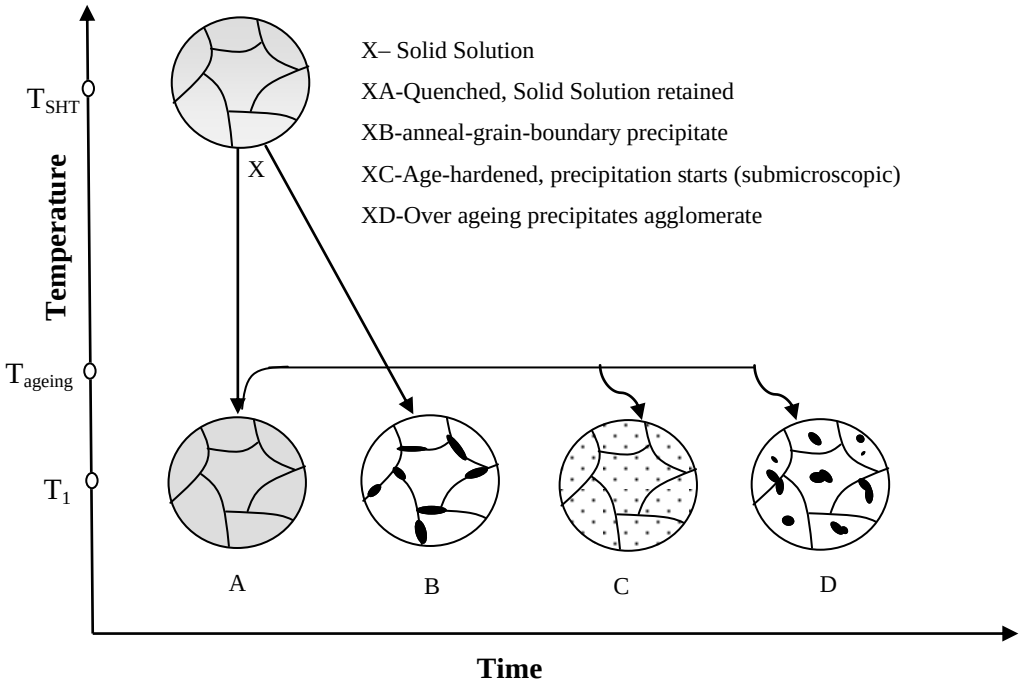

Figure 2-10 Schematic temperature profile for microstructure control of the HFQ process (www.app.eng.ubu.ac.th/edocs).

For further SHT time, diffusion of the alloying elements occurs and features such as coarsening, rounding and transforming take place, as well as the Mg_2Si phases completely dissolving. This rounding off of hard non-dissolvable particles with sharp edges also improves ductility and reduces the occurrence of holes when thin walled products are formed (Mrówka-Nowotnik et al., 2005; Garrett et al., 2005).

Once the material is solution heat treated, the material is transferred to the cold die set for forming and quenching. Hence, the quenching stage is the most critical stage in the HFQ process. The post strength of the material after ageing basically depends on the quenching rate used after solution heat treatment. The purpose of quenching is to produce a supersaturated solid solution (SSSS) of the alloying elements in the α-aluminium matrix. If the material were slowly cooled (path XB, Figure 2.10), the β phase would nucleate and grow, particularly at the grain boundary to form an equilibrium α+β structure. This inhomogeneous cooling of the deformed component produces inhomogeneous microstructures and hence causes weakness in the final components. However, for fast quenching (path XA, Figure 2.10) the precipitates have not got enough time to nucleate and it provides a microstructure known as a supersaturated solid solution. Mrówka-Nowotnik (Mrówka-Nowotnik et al., 2005) studied the effect of cooling rates on the microstructure of AA6082 after solution heat treatment as shown in Figure 2.11. From this figure, it is likely that the alloy is solution heat treated at a temperature of 570˚C. At this temperature, the transformation of the β-AlFeSi phase to a more spherical α-Al(FeMn)Si phase may occur. It is proposed that the very fine precipitates shown in Figure 2.11(a–c) are particles of the β-Mg_2Si phase. The dissolved particles of β-Mg_2Si phase will precipitate during slow cooling after homogenization. For slow (furnace cooling) the amount of β-Mg_2Si is high as shown in Figure 2.11(c) and affects the post strength of the material after artificial ageing.

However, for fast cooling (water cooling) the amount of the second phase is very small (Figure 2.11(a)) and this makes the material very strong after ageing in terms of precipitation hardening.

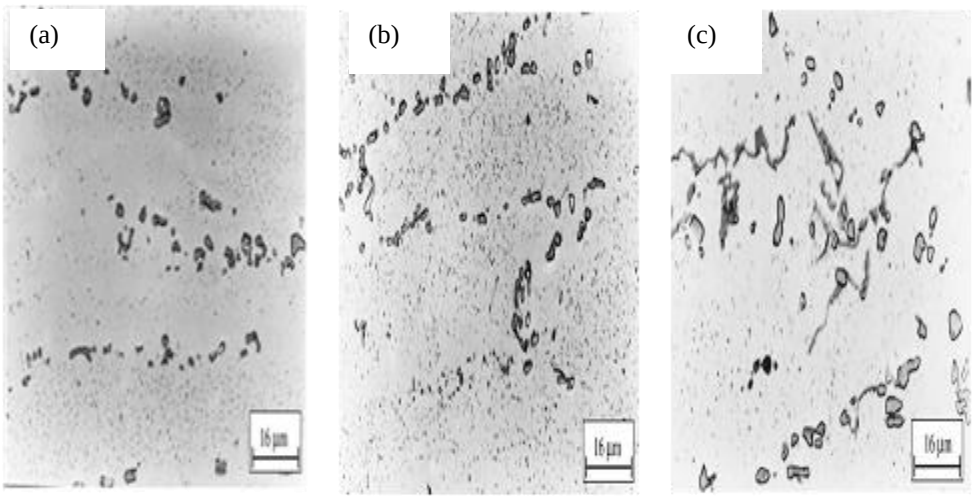

Figure 2-11 Microstructure of AA6082 alloy after homogenization at 570 ◦C/6 h and cooling in: (a) ice-water; (b) air and (c) in a furnace (Mrówka-Nowotnik et al., 2005).

The last stage of the HFQ process is the artificial ageing heat treatment. Ageing for the material takes place after the solution heat treatment in order to increase the material strength throughout a precipitation hardening process. For ageing hardening alloys such as the AA6xxx series, artificial ageing is used to promote the formation of the precipitates, as shown in Figure 2.10 (path AC). The type of precipitate that gives peak hardness of AA6xxx alloys is designated β″(Mg_6Si_5) and the shape is fine needles (point C, Figure 2.10). For further increasing ageing times, the material becomes weak. This is explained by the coarsening of the β″ phase and the transformation into other Mg-Si phases (path AD) (Roberts et al., 2000; Lin and Dean, 2005; Richard et al., 2006). Richard et al., (2006) studied the transmission electron microscopy (TEM)

images for different amounts of artificial ageing for the SHTed samples of AA6013, shown in Figure 2.12. Under-aged (UA), peak-hardness (PA), and over-aged (OA) are the three different ageing conditions. This Figure shows the dispersoid phases of the order of hundreds of nanometres, with the finer phases being the hardening phases. The UA sample contains very little visible precipitates. However, in the case of the PA sample, the microstructure contains a very fine distribution of precipitates, which coarsens as the ageing time increases as in the OA sample.

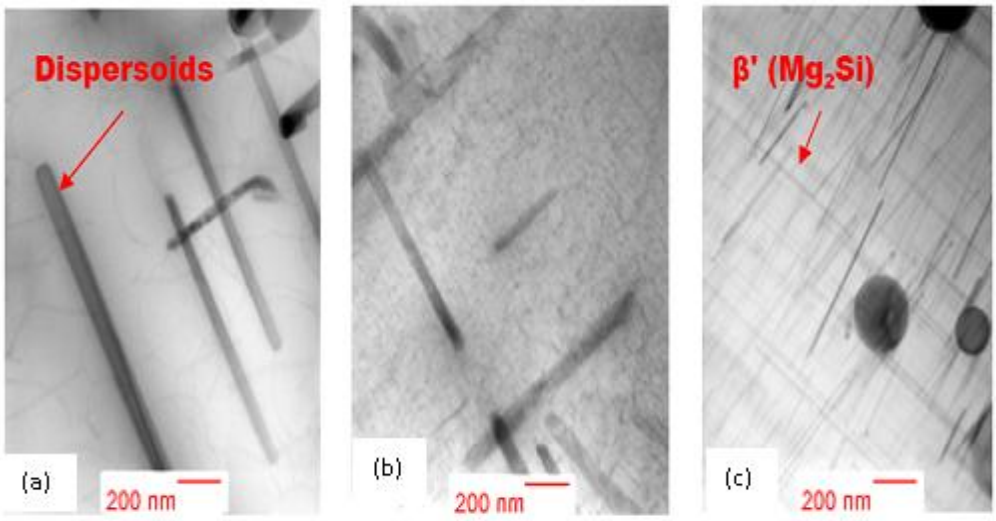

Figure 2-12 TEM images of 6013 taken from Richard et al., (2006), (a) UA, (b)PA and (c) OA .

2.6 Discussion and summary

In this chapter an overview is presented of advances and ongoing research in sheet metal forming technology to meet the demands for processing lightweight materials. Advanced metal forming processes such as sheet hydroforming, superplastic forming, and hot stamping and cold die quenching processes improve the formability of lightweight materials, thereby enhancing their use in the automotive industry. In

addition, microstructure evolution of the aluminium alloys AA6xxx is investigated in order to provide the desired mechanical properties for particular automotive requirements. Further reviews are presented in subsequent chapters, such as viscoplastic-damage modelling and precipitation hardening modelling in Chapters 5 and 7 respectively.

Chapter 3
Experimental Programme

3.1 Introduction and objectives

This chapter contains a detailed description of the experimental methods designed to investigate the feasibility of the novel HFQ process for AA6082. To implement the new process into a manufacturing environment, it must ensure that if the process is practical for its application and if so, if the desired results can be achieved in terms of material properties, microstructure, etc., for formed parts. This chapter also includes test facility design and descriptions and test sample preparation.

The experimental programme is divided into four main parts; the first is thermal testing, which is used to investigate the effect of the quenching rate on the post strength of AA6082 in the HFQ process. The second is the hot tensile test (ductility test), which is carried out to investigate the effect of high temperature deformation parameters (strain rate and deformation temperature) on the mechanical properties of AA6082. The third concerns the effect of prestrain on the ageing kinetics of AA6082 (strain ageing test). The last is the formability test which investigates the formability limit and failure features in the HFQ process. The testing facilities related to individual testing programme are introduced in the relevant sub-sections.

3.2 Test material

In all tests, the heat-treatable aluminium alloy AA6082 was used. It was originally supplied in large sheets with thickness of 1.5 and 2 mm, in a T6 condition. The recommended T6 heat treatment for AA6082 is heating to 525 °C for 30 min which ensures full dissolution of the alloying elements into the matrix, followed by ageing by heating to 190°C for 9 hrs (Garrett et al., 2005). This process is typical of commercial production of AA6xxx aluminium alloy sheet. The chemical composition of the AA6082 alloy investigated in the tests is given in Table 3.1 (Garrett et al., 2005).

Table 3-1 Chemical composition of the test material (Garrett et al., 2005).

Element	% wt
Si	0.7-1.3
Fe	0.5
Cu	0.1
Mn	0.4-1.0
Mg	0.6-1.2
Zn	0.2
Ti	0.1
Cr	0.25
Al	Balance

3.3 Experimental programme of thermal and hardness tests for quenching rate effect

The aim of this part is to investigate the effect of the quenching rate on the mechanical properties of AA6082 in the HFQ process. Rapid quenching suppresses precipitate nucleation and growth during quenching and retains the solute atoms and quenched-in vacancies in solution. Therefore, rapid quenching provides the high strength of the alloy. Rapid quenching is represented as the temperature profile (TP_i) shown in Figure 3.1. At this condition, the secondary phase has not an opportunity to grow and thus the material's single phase will be maintained intact as SSSS. If the material is quenched at an even slower rate (TP_{ii} Figure 3.1) then the material makes a large pass through the C-curve. Due to the fact that it crosses into the C-curve, a high proportion of precipitates grow. At this condition the precipitates becomes large and coarse, which result in a weaker material. Hence the quench rate affects the post strength during the subsequent ageing process.

Quenching rate is highly dependent on the quenchants used for quenching aluminium alloys, which include air, water, and cold die quenching. Water is most commonly used to quench aluminium alloys, but this quenching most often causes distortion, cracking, and residual stress problems. This is the reason for using cold die quenching in the HFQ process to avoid any of the above problems.

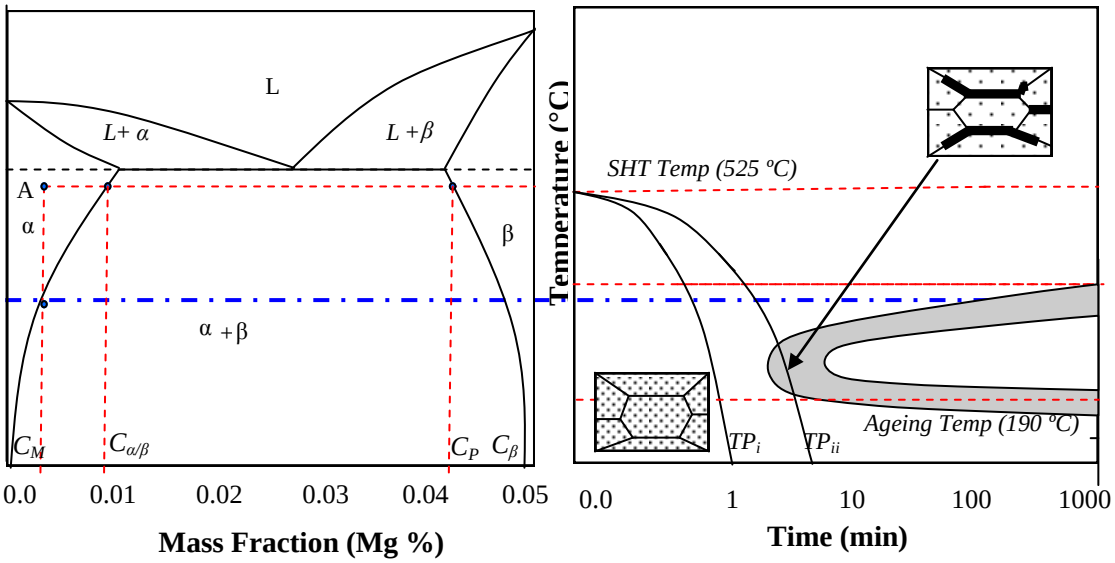

Figure 3-1 The phase diagram of AL-Mg-Si (b) TTT diagram for the precipitation of Mg2Si in al-matrix and schematic diagram of the microstructure from (TPi) fast and (TPii) slow quenching.

3.3.1 Sample preparation

The samples which are used for thermal-mechanical testing using Gleeble machine simulator are short 'dog-bone' samples. These dog-bone type samples were machined from the supplied large sheet in the rolling direction with T6 conditions. The geometry of the samples is shown in Figure 3.2.

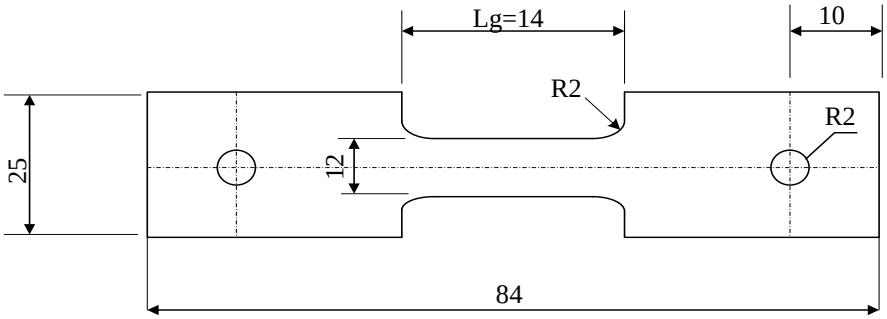

Figure 3-2 Short 'dog-bone' sample with thickness 1.5 mm and gauge length (Lg) 14 mm (dimension in mm).

3.3.2 Test facilities

3.3.2.1 Gleeble material simulator

The Gleeble (3800) is designed to carry out physical simulation of thermo-mechanical processes at a maximum heating rate of 10,000°C/sec, a maximum quenching rate of 10,000°C/sec and a maximum stroke rate of 2000 mm/sec. To control the temperature of specimen, thermocouples welded at the centre of the specimen provide signals for accurate feedback. Tests can be carried out in tension, compression, plane strain and plane stress conditions. Figure 3.3 shows the Gleeble machine simulator (3800 series).

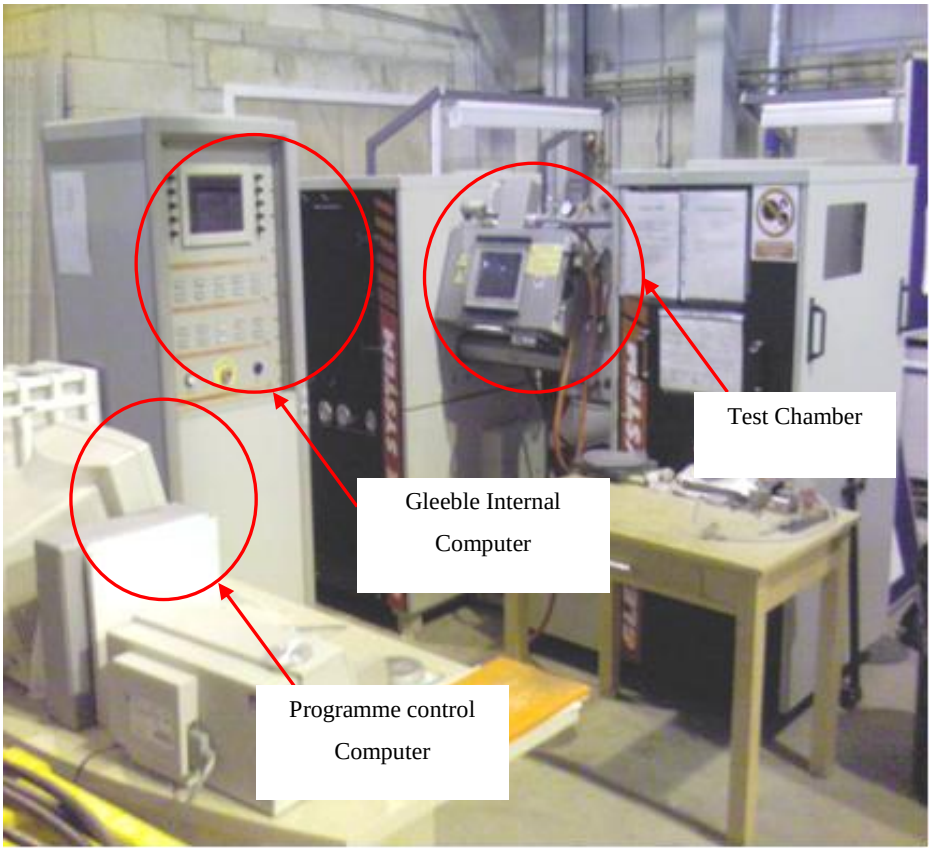

Figure 3-3 Gleeble material simulator (3800 series).

3.3.3 Test procedures

In this section, test procedures are described to investigate the effect of cooling rate on the mechanical properties of AA6082 during the HFQ process. The different cooling rates which were used in the test were 100, 50, and 10°C/sec. Where 10°C/sec is close to air cooling, 50°C/sec is similar to the heat removed when the sample is in contact with cold dies, and 100°C/sec is similar to water quenching. The aim of this test is to assess the precipitation hardening of the cold die quenching in comparison with air and water cooling. The samples in Figure 3.2 were used, and the tests were carried out using the Gleeble Material Simulator. The samples were heated to a SHT temperature of 525°C with a constant heating rate of 50°C/sec. The samples were then cooled with different cooling rates (100, 50, and 10°C/sec). After cooling to room temperature, the samples were then aged at 190°C for 9 hours. Hardness tests were carried out for the samples before and after ageing. Figure 3.4 shows the time-temperature profiles of different cooling rates tests.

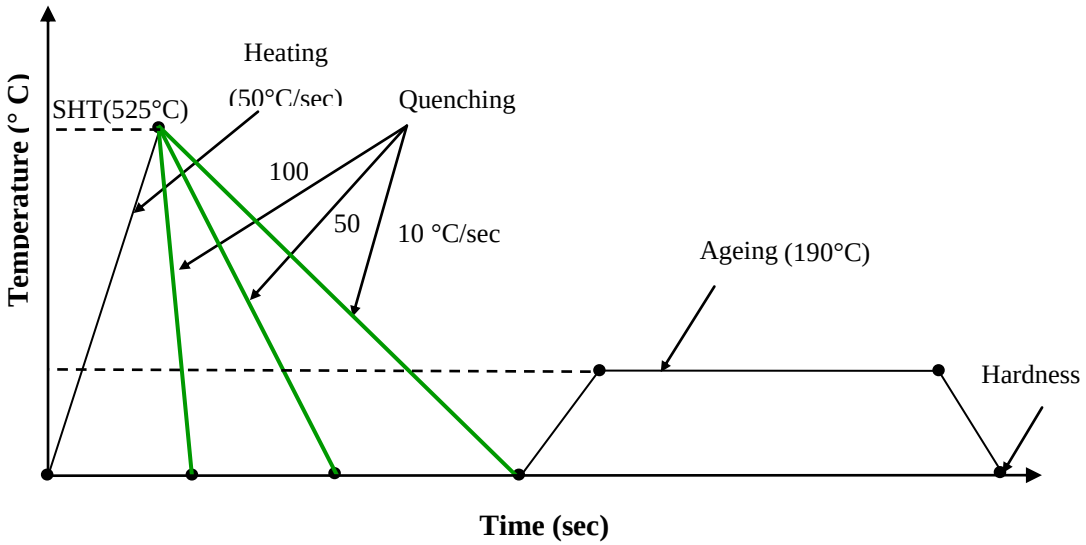

Figure 3-4 Time-temperature profile for the experimental tests of the effect of quench rate on mechanical properties of AA6082.

3.4 Experimental programme for ductility tests (hot tensile tests)

To investigate the viscoplastic behaviour and ductility of the AA6082, tests were designed to deform the material at different temperatures and strain rates using the Gleeble material simulator. In the manufacturing process, the sheet is heated to the SHT temperature, and then transferred to a press for deformation. The transfer may take a few seconds, during which the sheet temperature decreases. A further decrease in temperature occurs during the forming process as heat transfers to the cold dies (Foster et al., 2008). The forming process takes place over a temperature range of 525-450°C. The process is conducted quickly, with forming times typically being less than 1s (Foster et al., 2008).

3.4.1 Test procedures

The experimental tests were carried out using Gleeble material simulator 3800. The geometry of the testpiece which is recommended by Dynamic Systems Inc. (DSI) (the Gleeble manufacturer) is shown in Figure 3.2. The "dog-bone" sample with dimensions: thickness 2 mm, gauge length (Lg) 50 mm, and width 12mm, was machined from the supplied sheet in a T6 condition. Figure 3.5 shows the temperature profile for different deformation temperatures tensile tests. The testpieces were heated to SHT temperature of 525°C. The heating rate is divided into two steps; the first step is to heat the testpieces to 500°C using a heating rate of 50°C, the remaining heating is completed at a rate of 5°C as shown in Figure 3.5. The reason for that is to avoid the overheating of the sample. The temperature was then dropped to the deformation temperatures (525, 500, 450°C) with a cooling rate of 100°C/s. The temperature was controlled via a thermocouple welded at the centre of the testpiece. To evaluate the

viscoplastic flow of the material, three strain rates are selected according to the hot stamping process. They are 0.1, 1.0 and 10s^{-1}. Test parameters are listed in Table 3.2.

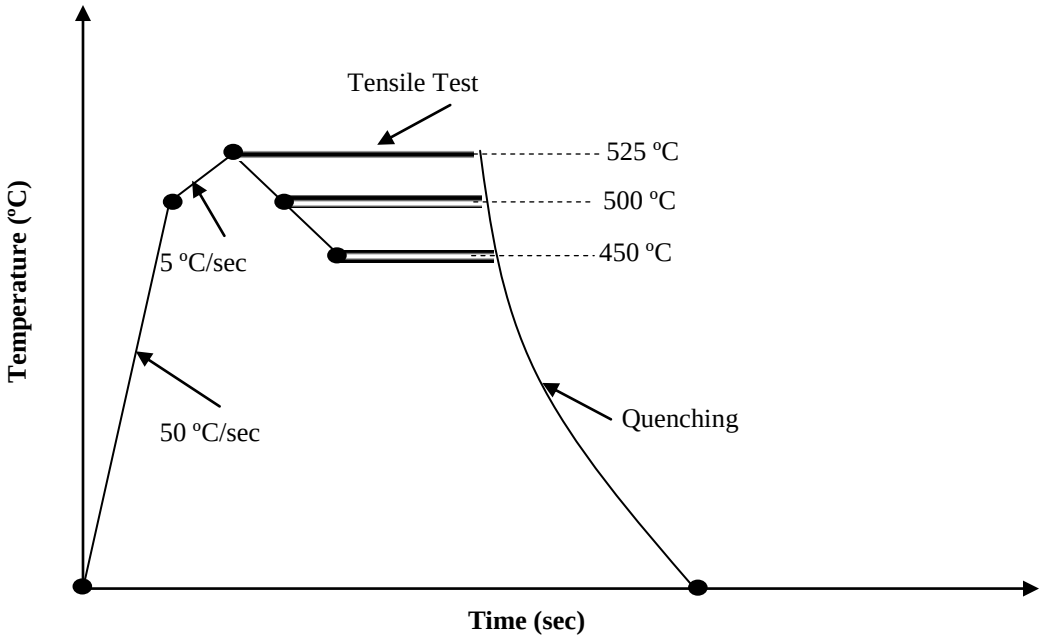

Figure 3-5 Schematic diagrams showing the experimental conditions for ductility tests.

Table 3-2 The experimental programme. '√' represents the selected tensile test conditions.

Strain rate (s^{-1}) / Temperature (°C)	0.1	1.0	10
525		√	
500	√	√	√
450		√	

3.5 Strain ageing test for AA6082

The effect of prestrain after solution heat treatment on the artificial ageing response has been examined for AA6082. Plastic deformation introduced after the solution heat treatment and prior to artificial ageing has been found to enhance the strength and ageing kinetics of the material. The plastic deformation introduces extra dislocations which act as preferential matrix nucleation sites for the primary strengthening phase. Increasing the amount of plastic deformation leads to a greater number of matrix dislocation (competitive heterogeneous nucleation sites) (Poole et al., 2000). An increase in the number density of nucleation sites creates overlapping diffusion fields as precipitates grow, causing the average size of precipitates to decrease. The refinement of the precipitate microstructure corresponds with the enhanced ageing kinetics due to the increased number density of strengthening precipitates (Poole et al., 2000; Deschamps et al., 1998; Birol et al., 2005; Esmaeili and Lloyd, 2005; Azushima et al., 2008). This section provides a detailed description of the experimental programme designed to investigate the effect of the plastic deformation on the post strength after artificial ageing of AA6082. Automotive manufacturers would like the process to take place during the paint bake cycle. Therefore, the test procedures will be held at baking temperature of 173°C (Golovashchenko and Al Krause, 2005).

3.5.1 Test procedures

Test procedures and temperature control for the effect of pre-deformation on the ageing kinetics of AA6082 are shown in Figure 3.6. Tensile samples were machined parallel to the rolling direction from a T6 supplied sheet. The solution heat treatment consisted of holding the samples at 525°C for 30 minutes followed by a quench into a water bath. Tensile tests of as-solution-treated materials were conducted as quickly as possible after

water quenching (typically within 20 minutes). The samples stretched on an Instron tensile machine (series 4466) at room temperature with different pre-strain levels (2.9%, 8.57%, and 18. 57%). After the pre-strain, the samples were then aged at a baking temperature of 173°C. Hardness tests were carried out for the samples at different ageing periods.

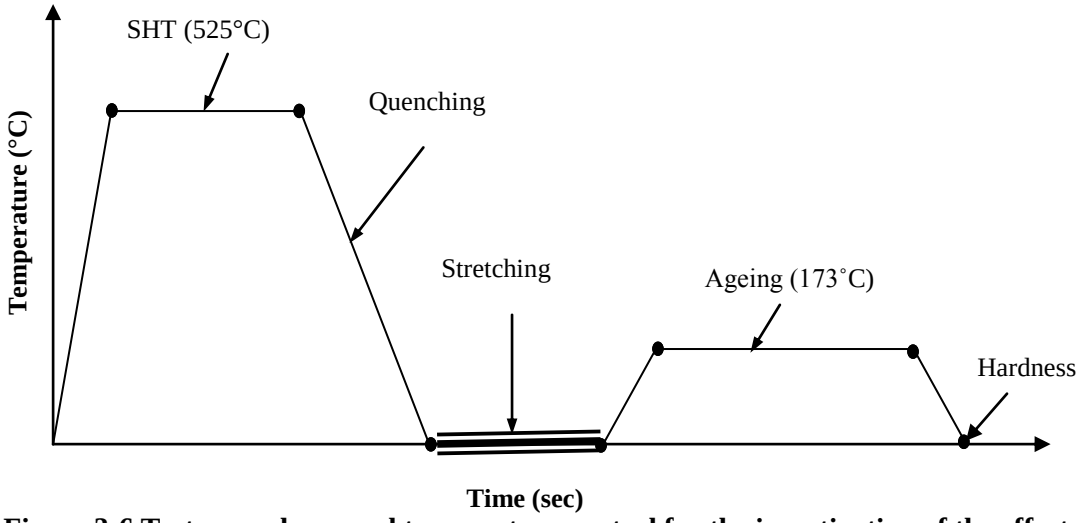

Figure 3-6 Test procedures and temperature control for the investigation of the effect of pre-deformation on ageing kinetics of AA6082.

3.6 Experimental programme for formability tests

For the manufacture of a component successfully using a hot stamping process, a correct choice of process parameters is essential. The optimal design of a hot stamping process requires a number of critical considerations including: (a) material flow behaviour at high temperature, (b) forming rate and drawing depth, (c) friction and lubrication, (d) tool design with temperature control.

This section contains a detailed experimental programme to perform the formability tests. The main hot stamping parameters are the forming rate and deformation temperature. A suitable lubricant was used between the punch and the sheet to reduce the friction and in turn give the material the opportunity to deform easily through the punch. The lubricant was selected according to the experimental work which was carried out by Foster (Foster et al., 2008). The experimental results are important for the validation of FE process simulation models.

3.6.1 Sample preparation

In formability tests, square samples with thickness of 2 mm were used as shown in Figure 3.7. A 16 mm diameter hole was drilled in the centre of the sample. The central hole would reduce the material constraint in the central region of the workpiece, while a cold-spherical punch was used in the forming process. The size of the hole was related to the ductility of the material and the size of the punch, which was optimised via a number of FE simulations. With this size of the hole, different failure modes and the formability at different forming conditions were expected to be observed in more details.

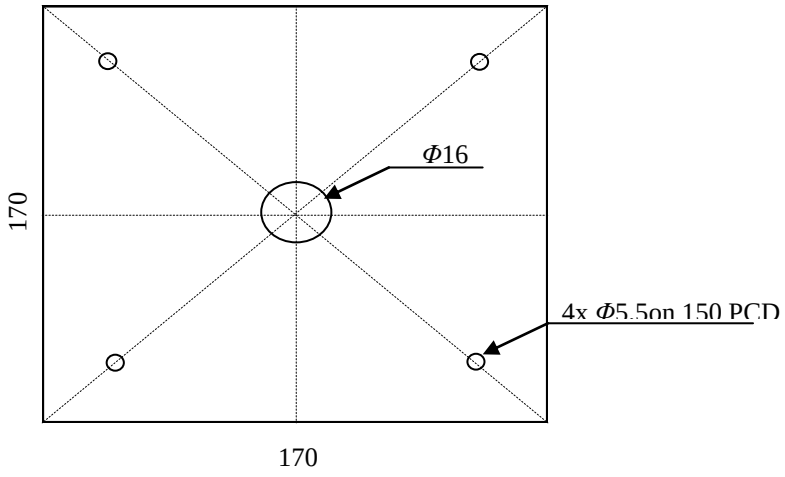

Figure 3-7 The geometry of the formability testpiece.

3.6.2 Test facilities

3.6.2.1 Hydraulic press and formability die sets

Tests were carried out using a 250 kN high speed hydraulic press with the designed formability die-set, as shown in Figures 3.8. The die set was designed to interrogate formability by stretching the sheet over a hemispherical punch (diameter 80mm), thereby imposing a difficult biaxial state of strain (i.e. radial and circumferential) on the sheet in contact with the die. The tool set, as shown Figures 3.8 has four main parts: hemispherical punch, top and bottom blank holders, and gas springs. Light springs maintain separation between the top plate and blank holder plate, where the sheet is located, until the press stroke equals the initial separation at which point the sheet is clamped between the blank holders (the much stiffer gas springs do not deflect appreciably until this occurs, but thereafter provide the clamping force on the sheet, which increases with increasing press stroke). The bottom blank holder was designed with a circumferential drawing bead, and corresponding recess in the top blank holder, to constrain the material from flowing into the die. The bottom blank holder was designed with four spring pins (diameter 5.5mm) to mitigate temperature loss from the sheet into the bottom blank holder after it is inserted and just prior to forming.

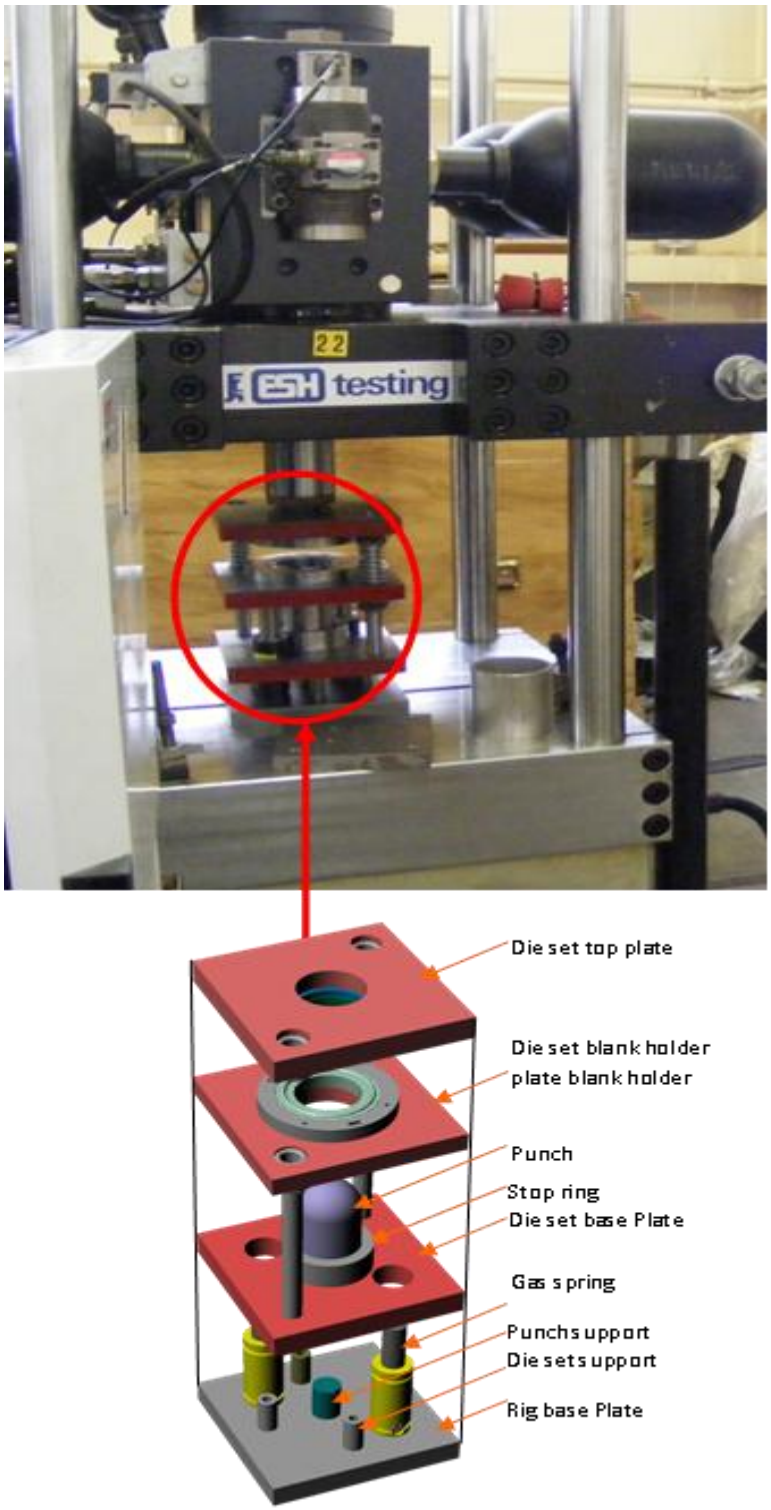

Figure 3-8 Formability test set-up and test rig design.

3.6.3 Test procedures

Firstly, the samples were heated to the SHT temperature of 525°C inside the furnace and were then transferred to the press between the cold die set for deformation. The transfer took about 3-5 seconds, which caused temperature reduction. A further decrease in temperature may occur during the forming process, as the cold dies are in contact with the hot workpiece locally. While the thermal conductivity of aluminium is high (typically 170W/m-K), the large surface area and thin section of the sheet material means that local cold spots would form where contact is made with the cold dies (Foster et al., 2008).

In practice, the forming process for AA6082 takes place over a temperature range of 525-450ºC. To control the heating rate and SHT and deformation temperatures, a thermocouple was welded to the testpieces. Once the blank was transferred to the press between the die set, the deformation started with applying the blank holder pressure of approximately 3-MPa to insure no material draw in during the pure stretching experiments. The punch was then actuated to stretch the blank. A suitable lubricant was used between the punch and the sheet to reduce the friction and in turn give the material the opportunity to deform through the punch.

Table 3.3 represents the formability test matrix. Two types of forming tests were carried out: (i) Investigation of the failure features under fast (0.64 ± 0.01 m/sec) and slow (0.166 ± 0.01 m/sec) forming rates. In this case, the samples were deformed until failure occurred. ii) Investigation of the formability limit for different forming rates and in turn to optimize the HFQ process parameters by developing a process window for

HFQ process of AA6082. This is can be done by carrying out some tests with different forming rates and different drawing depths as shown in Table 3.3.

Table 3-3 Formability test matrix. '√' represents that the tests are carried out at those conditions.

Forming rate (m /sec) / Stroke (mm)	0.166	0.32	0.48	0.64
24	√	√	√	√
32	√	√	√	√
42	√			√

Chapter 4

Experimental Results and discussions

4.1 Introduction

This chapter contains detailed results and discussion obtained from the experimental programme described in the previous chapter. These results are presented, discussed and analysed with a view to determining the specification of a commercial HFQ process. The chapter is structured to mirror the experimental work detailed in Chapter 3. First, results obtained from thermal and hardness tests are presented to examine the effect of quenching rate on the post ageing strength of the material. The second results, obtained from high temperature tensile tests (ductility results), are used to study how deformation parameters (strain rate and deformation temperature) affect ductility. The third results give the effect of pre-strain on the ageing kinetics (strain ageing results) of AA6082. Finally, results showing the effect of differing forming rates and differing drawing depths on the formability limit and failure features of the AA6082 are presented.

4.2 Effect of the quenching rate on the mechanical properties of AA6082 alloys

Figure 4.1 shows the achieved hardness for a range of quenching rates before and after the ageing of AA6082. For an un-aged material, a slow quench (10°C/sec.) provides a slightly stronger material in comparison to the fast quench (100°C/sec.). The slow

quench provides ample opportunity for coarse precipitates to nucleate and grow within the material matrix. The precipitates add strength and thus the material is slightly stronger in the quenched state. By contrast, for a fast quench, the heat is removed rapidly and there is insufficient time for precipitates to nucleate; thus the strength comes from only the soft single phase.

When the material is aged at 190°C for 9hrs, the result is reversed and the samples which were quenched rapidly produce the stronger material. The precipitating alloying elements are retained in the matrix during quenching, allowing precipitates to nucleate and grow during ageing, producing a fine precipitate phase. On the other hand, the slower quench decreases the retained supersaturation of solute available for the development of a fine precipitate phase during the subsequent ageing treatment.

Similar material properties exist between the water quenched (100°C/sec.) and the cold die quenched material (50°C/sec.). From this result, the quenching rate 50°C/sec, which is similar to that obtained during a cold die quench, is sufficient to suppress unwanted precipitation during quenching and to retain as a solute the elements available for the subsequent ageing treatment.

This material has not been affected by the SHT time. Tests were conducted to confirm the null effect of SHT time on the hardness of quenched, and quenched and aged samples. The results are illustrated in Figure 4.2. Each point on the graph was averaged from 5 data points. The lack of dependence of hardness on SHT time is consistent with fine precipitants quickly dissolving into the primary a-Al matrix during heating.

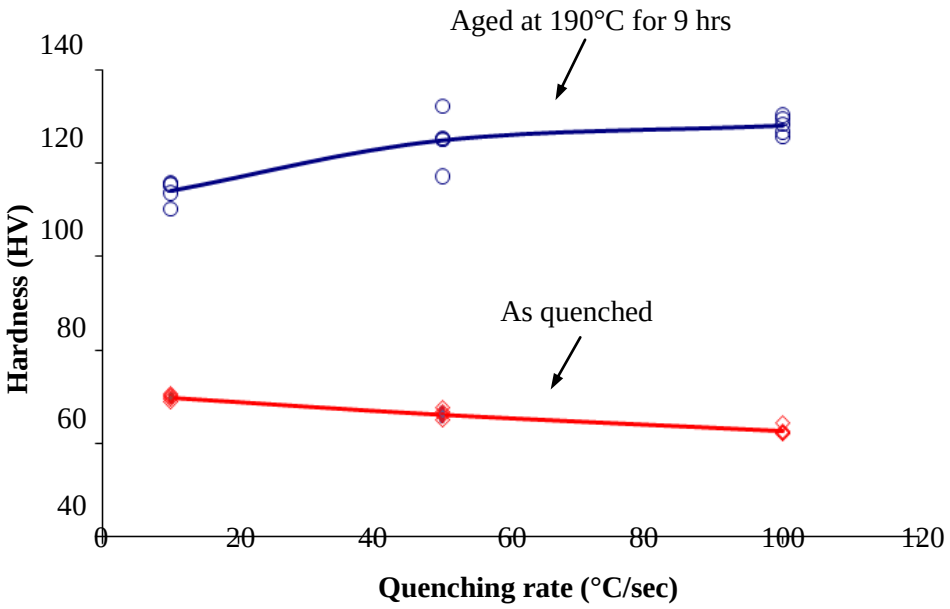

Figure 4-1 Effect of quenching on the hardness for SHT temperature of 525°C of AA6082.

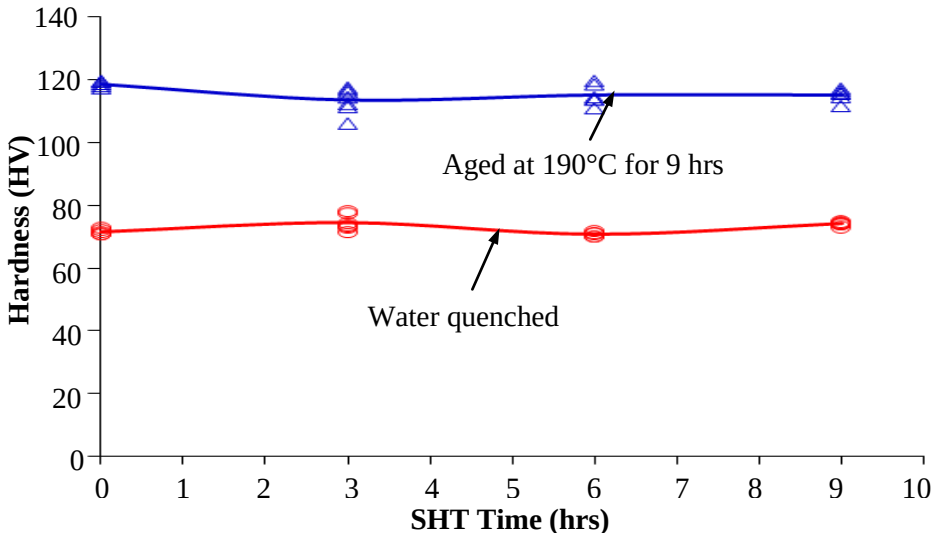

Figure 4-2 Effect of SHT time on the hardness for the samples solution heat treated at 525°C of AA6082.

4.3 Effect of the high temperature deformation regime on the mechanical properties for AA6082

4.3.1 The effect of strain rate on the mechanical properties of AA6082

Figure 4.3 shows the experimental results of the material tested for different strain rates (0.1, 1.0, 10 s^{-1}) at a deformation temperature of 500°C. The flow stress increases significantly with increasing strain rate, which demonstrates the highly viscoplastic nature of the material at 500°C. The ductility also increases with increasing strain rate, contrary to what is commonly observed of other materials. These results are in agreement with results published by Lassance (Lassance et al., 2006) and Danaf (El-Danaf et al., 2008; El-Danaf et al., 2009) for AA6082. It is theorised that this is due to the effect of grain growth within the aluminium matrix at lower strain rate, which would affect the ductility of the material. Grain boundary deformation effects (grain boundary sliding and rotation) are primarily diffusion controlled, hence rate (and temperature) limited, so the effect of increasing strain rate both encourages and inhibits ductility. However, the effect of a large grain size resulting from a lower strain rate likely offsets any gain in activation of grain boundary deformation effects associated with that lower strain rate. Towards the end of deformation the flow stress decreases due to damage softening which dominates until the final failure strain is achieved.

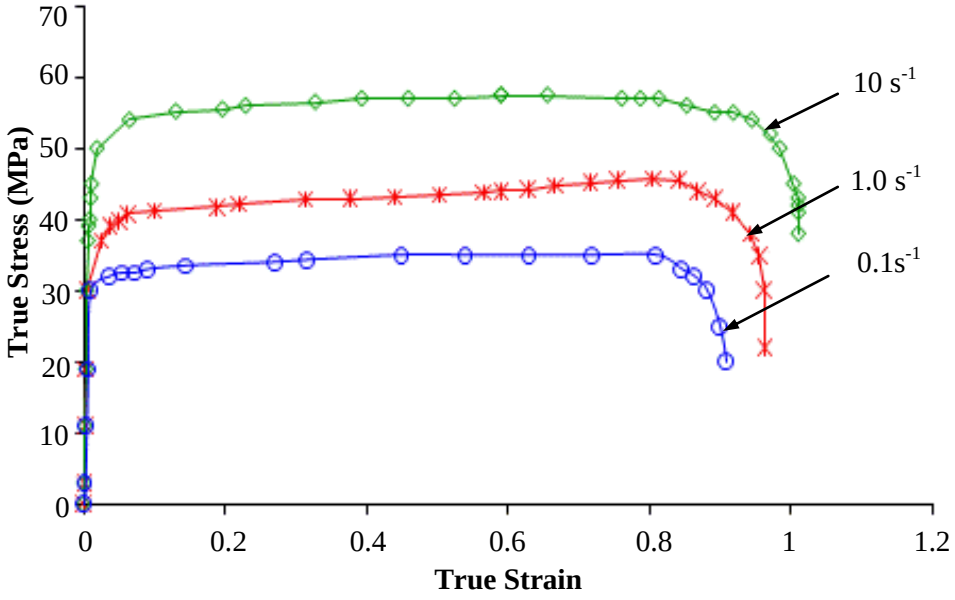

Figure 4-3 Experimental stress-strain relationships for different strain rates at deformation temperature 500°C.

4.3.2 The effect of deformation temperature on the mechanical properties of AA6082

Figure 4.4 shows the experimental results of the material tested for different deformation temperatures (525, 500, 450°C) at a strain rate of $1s^{-1}$. From the Figure, the measured flow stress decreases with increasing temperature. This is typical of most metals, and is commonly a result of higher dislocation mobility (by increased thermal vibration of the lattice and lower relative strength of obstacles to dislocation motion), activation of diffusion controlled processes such as grain boundary sliding and rotation and dislocation climb, as well as a generally more active recovery mechanism, all of which are thermally activated processes. In general, greater ductility can be expected with increased temperature, and this can indeed be observed by comparing the tensile test results carried out at 450°C to those at 500°C. The results at 525°C do not follow

the trend with temperature, although the ductilities of the 500ºC and 525°C tests are effectively indistinguishable given possible small error inherent in the stress and strain measurement; the lack of improvement in the ductility at 525ºC relative to 500°C is likely a result of the significant necking experienced near final failure, which biases the measured strain and makes calculating the stress difficult as an accurate measure of the neck diameter at that stage of the deformation is not available. Increased ductility implies that increased formability can indeed be achieved by forming at high temperature, hence more complicated components can be manufactured, with features such as large draw depths and sharp corners, and multi-part assemblies can be consolidated. Hence transferring the sheet from the furnace to the press is critical, in that it should be done quickly and with minimal opportunity for convective heat loss (e.g. the plane of the sheet should be parallel to the direction of transfer), and the forming process should also be carried out quickly to minimise the loss of heat to the dies.

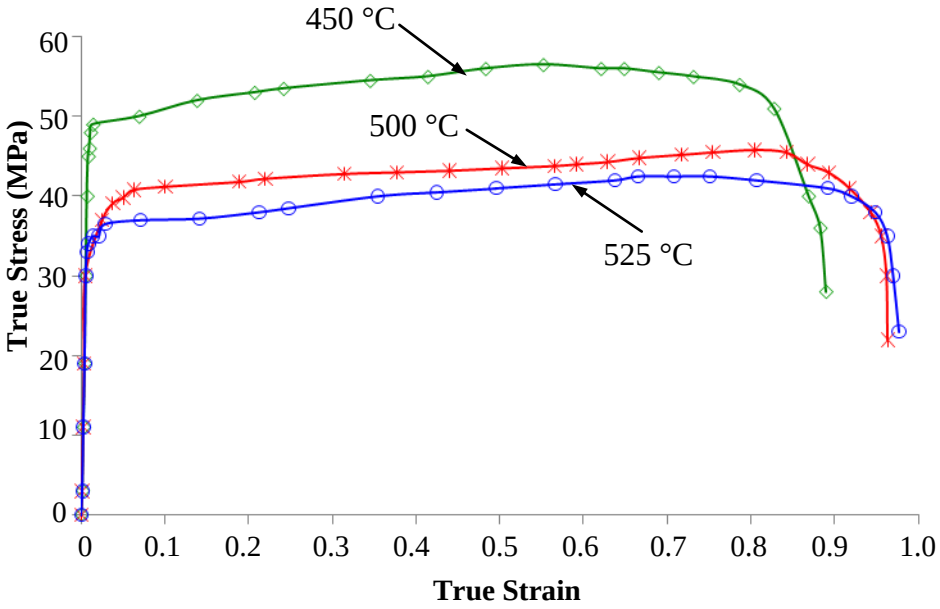

Figure 4-4 Experimental stress-strain relationships for different deformation temperatures at a strain rate of 1s-1 of AA6082

4.4 The effect of plastic deformation on the ageing kinetics prior to artificial ageing for AA6082 alloys

In this section, it is found that the plastic deformation after the solution heat treatment process can notably influence the ageing kinetics of AA6082. The effect of the pre-strain on peak hardening depends on the level of deformation. In addition the pre-strain accelerated the ageing process in terms of the precipitates nucleation and growth.

The variation in the hardness during isothermal ageing at 173ºC of AA6082 for different pre-strain levels is shown in Figure 4.5 Several important observations can be made from the data in Figure 4.5, the kinetics of ageing is accelerated and the magnitude of the peak hardness increases with presence of the pre-strain. This is through the introduction of dislocations which act as nucleation sites for the hardening phase. Increasing the amount of introduced plastic deformation leads to a greater number of matrix dislocations (Poole et al., 2000; Birol et al., 2005; Zhu and Starink, 2008). An increase in the number density of nucleation sites creates overlapping diffusion fields as precipitates grow, causing the average size of precipitates to decrease. The refinement of the precipitate microstructure corresponds with the enhanced ageing kinetics due to the increased number density of strengthening precipitates (Poole et al., 2000).

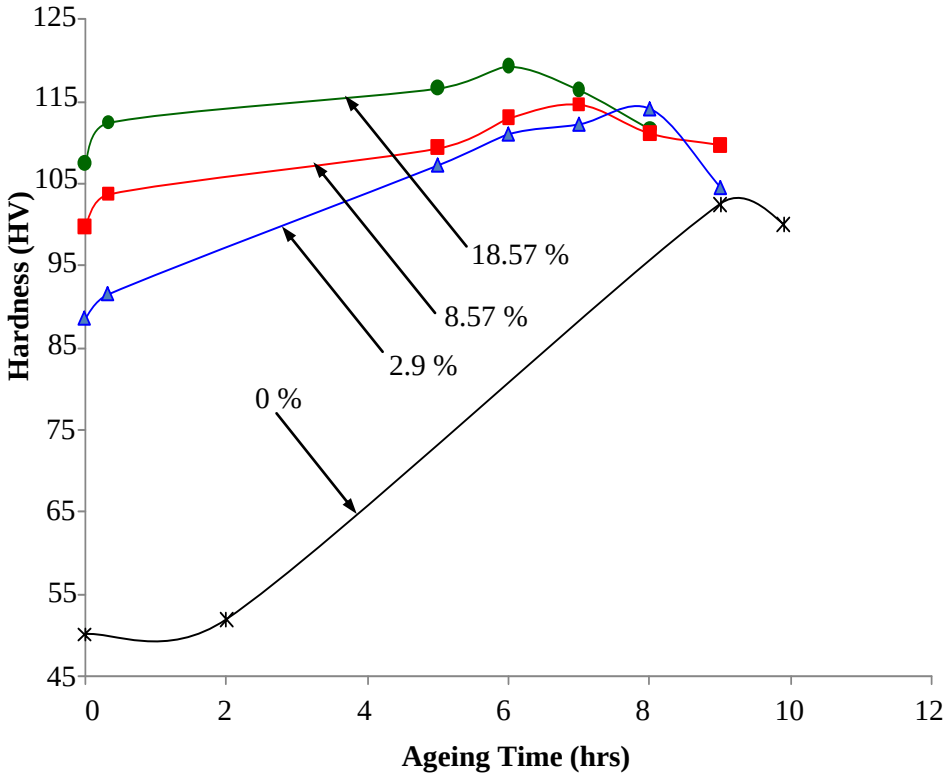

Figure 4-5 Experimental Ageing-hardening curves for AA6082 aged at 173±5°C for different levels of pre-deformation (0%, 2.9%, 8.57%, and 18.57%).

4.5 The effect of forming rate and drawing depth on the failure features and formability for AA6082 alloys

To find the proper forming conditions for the aluminium alloy sheets, the formability limit and the failure features of AA6082 during hot forming processes has to be correctly predicted. Therefore, the knowledge of failure features is essential. According to the formability results, two failure modes were observed in the hot stamping of AA6082 tests: (A) radial necking and subsequent tearing, emanating from the central hole, and (B) circumferential necking and subsequent tearing, occurring approximately halfway between the base and apex of the formed cup. Figure 4.6 (a) and (b) show hot

stamping experimental results for a deformation temperature of 470±10°C, punch stroke of 42 mm and forming rates of 0.64 ± 0.01 m/sec and 0.166 ± 0.01 m/sec, respectively. The following conclusions can be drawn from the experimental results:

- The failure feature of AA6082 under hot stamping depends on the forming rate.
- At a slow forming rate, failure occurred as a circumferential tear, preceded by necking at a middle height location on the formed cup. The time elapsed from when punch and sheet first come into contact until the end of forming is higher for a slower forming rate. This results in a higher temperature reduction in the region of contact, and, in turn, the part of the sheet in contact with the punch becomes harder than the area not in contact with the punch. Hence, most of the stretching occurred in the part of the sheet not in contact with the punch because it was hotter and so had a higher ductility and lower flow stress; the eventual failure was initiated by necking resulting from excessive strain in a preferred circumferential location.
- A high forming rate led to radial necking and tearing. Thinning of the sheet was maximal around the periphery of the central hole; radial thinning followed at a preferred location, and brought about the eventual ductile tearing of the sheet in that location. In contrast with the slow forming rate case, the central region of the sheet is in contact with the punch for a shorter time, causing a smaller temperature reduction. Therefore, provided the forming rate is sufficiently fast, the central region of the sheet in contact with the punch remains at a relatively high temperature, and so has a higher ductility and lower flow stress than the same region when the forming rate is slower. Hence, the central area of the sheet can be easily deformed, allowing ductile failure to occur at that location. It should be noted that if the sheet temperature were uniform and constant

throughout the forming, the strain in the central hole area would be higher, hence that is the preferred location of failure in the absence of sufficient cooling to cause failure to occur circumferentially, away from the central hole.

Slower forming rate can exacerbate uneven temperature of the sheet. While a non-uniform temperature profile can be useful in special cases, in general a uniform temperature is desirable to ensure homogeneous deformation (Foster et al., 2008), this is simplest to achieve by using a fast forming rate since heat transfer to the dies during the deformation process is kept to a minimum. AA6082 aluminium alloy shows little intrinsic strength at the SHT temperature and does not significantly strain harden when deformed. As a result, the low flow stress may not be sufficient to draw material into the die and across the die surface, leading to local thinning and low formability (Foster et al., 2008). By increasing the forming rate, the deformation can occur at a higher temperature, at which the microstructure is stable and the material is ductile, so the aluminium will have enough strength to pull material into the die.

Figures 4.7 (a, b), and 4.8 (a, b), 4.9 (a, b), and 4.10 (a, b) show the formability results for 0.166, 0.32, 0.48, and 0.64 m/sec respectively, where a, b corresponds to the drawing depths 24mm and 32mm. From these Figures, it could be seen that the samples deformed with the above forming rates and drawing depths are not failed. The overall results in this section are used to verify the numerically determined forming process window and this will be discussed in details in Chapter 6.

4.6 Conclusions from the experimental results

Based on the experimental results represented in the previous sections, major conclusions drawn from this study are as follows.

- Based on the thermal tests results, quenching between cold die set is more convenient and effective than water and air quenching during the HFQ process.
- A series of thermo-mechanical tests have been carried out on AA6082 and it has been found that at the same temperature, the ductility of the material is higher at high strain rate. This result are used to formulate the viscoplastic damage constitutive equations in Chapter 5
- The post strength of the AA6082 aluminium alloy after ageing is increased and the ageing kinetics is accelerated with the presence of the pre-strain prior to the ageing process. These results are used to formulate the precipitation hardening constitutive equations in Chapter 7.

The failure features of the AA6082 in the hot stamping of panel parts are forming rate dependent. For a high forming rate, the failure mode is radial tear from the centre. However, for a slow forming rate, the failure mode is a tear around circumference. Using this result, validation and optimization of the HFQ.

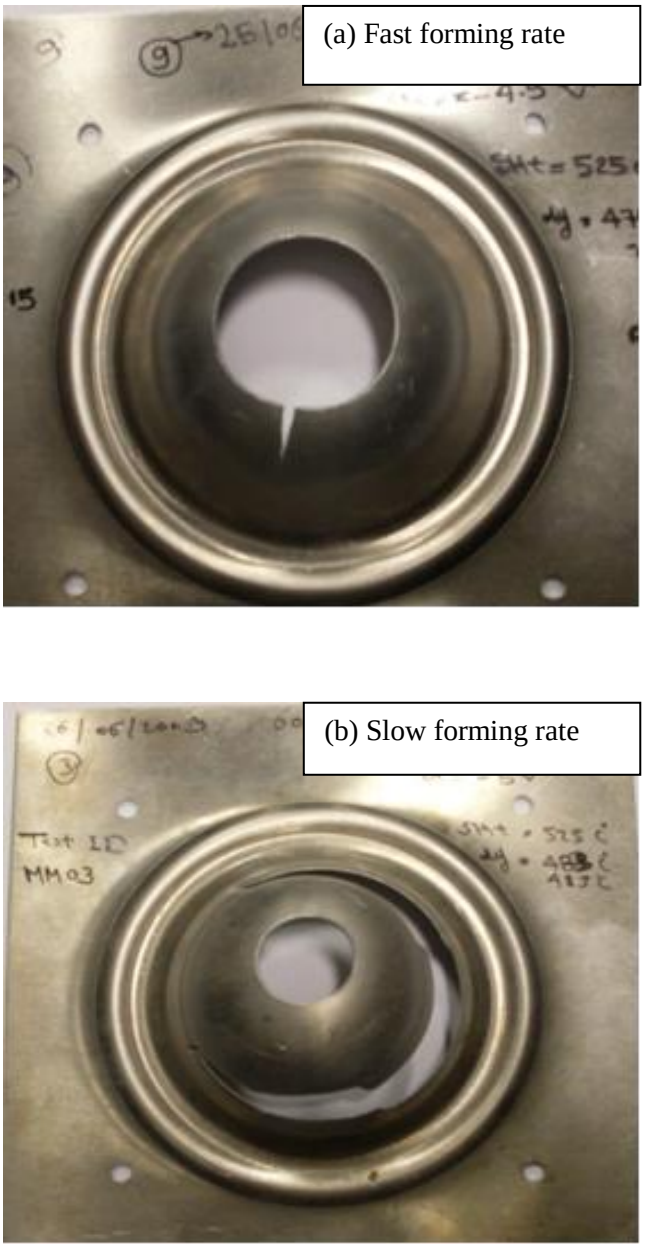

Figure 4-6 Experimental results for AA6082, deformed at 475±10 °C; a) Fast forming rate (0.64 ± 0.01 m/s) test fail due to radial rip from the central. b) Slow forming rate (0.166 ±0.01 m/s) test fail due to rip around the circumferential with punch stroke 42 mm.

(a)Stroke 24 mm (b) Stroke 32 mm

Figure 4-7 Experimental results for AA6082, deformed at 475±10 °C; with forming rate 0.166±0.01 m/sec. and different punch strokes; a) Stroke 24 mm, b) Stroke 32.

(a) Stroke 24 mm (b) Stroke 32 mm

Figure 4-8 Experimental results for AA6082, deformed at 475±10 °C; with forming rate 0.32 ±0.01 m/sec. and different punch strokes; a) Stroke 24 mm, b) Stroke 32.

(a) Stroke 24 mm (b) Stroke 32 mm

Figure 4-9 Experimental results for AA6082, deformed at 475±10 °C; with forming rate 0.48 ±0.01 m/sec. and different punch strokes; a) Stroke 24 mm, b) Stroke 32.

(a) Stroke 24 mm (b) Stroke 32 mm

Figure 4-10 Experimental results for AA6082, deformed at 475±10 °C; with forming rate 0.64±0.01 m/sec. and different punch strokes a) Stroke 24 mm, b) Stroke 32.

Chapter 5
Development of Viscoplastic Damage Constitutive Equations

5.1 Introduction

This chapter starts with a brief introduction to the deformation and damage mechanisms during deformation processes and then a specific deformation and damage mechanism for AA6xxx is identified. In this chapter, the viscoplastic-damage behaviour of fully solutionised AA6082 at, and below, the SHT temperature is discussed. Based on the experimentally observed results in Chapter 4, a set of unified viscoplastic damage constitutive equations is formulated and determined for AA6082 within the strain rate range of 0.1–10s^{-1} and deformation temperature range of 450-525°C. Damage, including the imaging of damage nucleation and growth features, has been investigated for tested samples using SEM. The computationally-derived stress strain relationships is presented and fitted with experimental results over the strain rate and temperature range considered.

5.2 Deformation and damage mechanisms

Hot deformation processes are generally carried out at high temperature ($T > 0.5T_m$) and typically involve a large plastic strain. It is related to thermal and physical

phenomena such as strain hardening, recovery, recrystallisation and dislocation mobility, all of these phenomena are highly strain rate and temperature dependent (Liu, 2004). Theses cause a significant change in the microstructure of the material. An understanding of these phenomena is therefore essential to be able to model hot deformation processes. During plastic deformation, damage due to the softening occurs and is directly is associated with hot deformation mechanisms.

5.2.1 Deformation mechanisms

Plastic deformation is a kinetic process that is affected by many factors including strain, strain-rate and deformation temperature. Hot deformation processes typically involve large plastic strains and high deformation rates. According to these factors, different deformation mechanisms occur simultaneously during these processes. Dislocation annihilation and dislocation accumulation dictate the macroscopic mechanical behaviour and microstructural evolution of the material.

Figure 5.1 shows the inter-relationship between the hot deformation variables for a material deformed under high temperature. Initially, the material is deformed elastically to the yield point (k) and a linear stress-strain relationship is observed as seen in Figure 5.1. During this initial elastic deformation stage, the material deformation resistance and the dislocation density remain unchanged from their initial values (i.e. ρ_o). At this stage, the stress potential available to create the viscoplastic effect can be expressed as $\langle \sigma - k \rangle$. Once the material begins to yield, elastic-viscoplastic deformation commences. As the plastic strain rate increases, rapid plastic deformation is observed and the dislocation density increases and then accumulates. Dislocation accumulation is requiring a higher stress to continue the plastic flow. Moreover, new dislocations are formed, causing a further rise in dislocation density to a ρ. As plastic deformation

continues, the volume of dislocations will continue to increase and the in mean time the material gain the strain hardening effect R. Strain hardening cause a rapid increase in the flow stress. Hence the stress able to create the viscoplastic effect can be expressed as $\langle \sigma - k - R \rangle$.

Recovery or recrystallisation processes are occurred during the hot deformation and reduce the volume of dislocations. For low strain rate deformation, the microstructure evolution and the volume of dislocations are significantly affected by the dynamic and static recoveries. The visco stress (σ_v) is directly related to the strain rate, and as such contribute to the viscoplastic effect. As the strain rate increases, the flow stress is increases as shown in Figure 5.

During the latter stages of deformation, the softening due to micro-damage dominates and causes the flow stress to decrease as seen in Figure 5.1 (Lin, et al., 2002). Meanwhile, annihilation of dislocation gradually increases due to dynamic and static recovery processes. Annihilation processes are partially inhibited by dislocations cross-slipping onto different gliding planes resulting in slow recovery. Plastic deformation continues and the dislocation density continues to rise to a certain value. This is the maximum value of dislocation number that can attained within a material, based on the assumption a fully saturated network will form, denoted as ρ_{max} (Liu, 2004).

The different types of deformation mechanisms for aluminium alloys during cold and hot deformation processes are discussed in the following section. Two major deformation mechanisms are considered to contribute to the total deformation behaviour of the aluminium alloys: (i) the dislocation glide mechanism; and (ii) the grain boundary sliding mechanism (Frost and Ashby, 1969; Ashby, 1970).

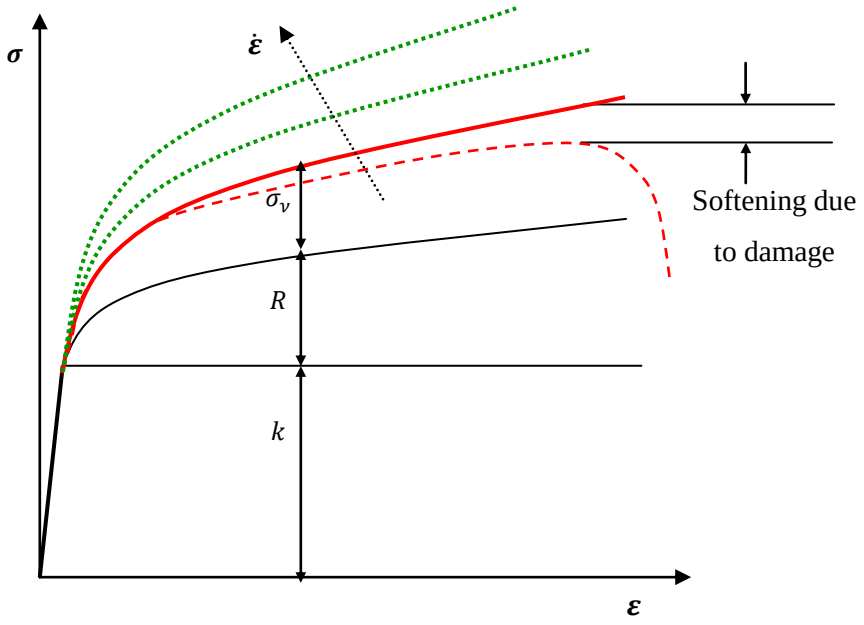

Figure 5-1 Schematic of superimposition of stress component in hot tension test

5.2.1.1 Dislocation glide and climb

Plastic flow of the material can occur due to dislocation glide. The mechanical behaviour of a material is dominated by the mobility and multiplication of dislocations. The mobility of dislocations is typically impeded by obstacles including other dislocations, grain boundaries and precipitates (Frost and Ashby, 1969). Dislocation can move through the material in several ways; edge dislocations can move by slip and climb, whilst screw dislocation can move by slip and cross-slip (Raj and Ashby, 1971). The way the dislocation moves which impacts on the observed plastic deformation behaviour (Raj and Ashby, 1971).

Strain fields can exist around the dislocations, and these control the mobility and multiplication of the dislocation. The strain fields serve to further impede to dislocation movement (Ashby, 1970; Ashby, 1983). For instance, if two edge dislocations have the same sign and lie on same slip plane, their strain fields interact and move them apart. However, if two dislocations have opposite signs and are on the same slip plane, they attract one another, and dislocation annihilation will occur when they meet (Ashby, 1983).

During cold deformation ($T < 0.3T_m$), the dislocation density increases due to the nucleation of new dislocations. Deformation is therefore limited by the rate of nucleation and gliding of dislocations. At low temperatures, the effect of the recovery mechanisms on the material microstructure is relatively low (Carrick, 2009). As such, increasing the plastic strain in the material serves to increase the number of dislocations in the crystal structure. This result in increase the flow stress needed to facilitate the movement of dislocation through and around one another, this is known as strain hardening. By employing a proper heat treatment, the effects of strain hardening can be removed (i.e. annealing) (Cocks, 1985).

At elevated temperatures ($T > 0.5T_m$), the thermal vibration of the lattice increases and therefore relative strength of obstacles to dislocation motion decreases. Activation of diffusion controlled processes such as grain boundary sliding and rotation and dislocation climb, results in a generally more active recovery mechanism (Carrick, 2009). The deformation becomes highly temperature and strain rate dependent. Due to the increase effect of the recovery mechanism, strain hardening is relatively low (Carrick, 2009). During hot deformation, the dislocations can glide, multiply and pile up into tangles resulting in increase in the amount of stress needed to maintain plastic

flow. Since the dislocations become entangled and their density rises, the annihilation of the generated dislocations increases. When the dislocation annihilation and dislocation generation rates are balanced, the flow stress ceases to increase and deformation proceeds at a steady- state. At lower strain rates, annihilation is relatively rapid and the steady-state balance is reached at a larger subgrain size and lower flow stress. However, at high strain rates, dislocation generation is relatively rapid and the steady- state balance is reached at a smaller subgrain size and higher flow stress (Frost and Ashby, 1969).

There is another mechanism by which dislocation can move. This mechanism allows an edge dislocation to move out and perpendicular to its slip plane and is known as dislocation climb. Dislocation climb at grain boundaries is a high temperature deformation mechanism (Frost and Ashby, 1969). Since grain boundary diffusion takes place at a higher rate than lattice diffusion, dislocation climb rates are likely to be higher in the proximity of a grain boundary. Therefore, dislocation climb at grain boundaries is likely to be the dominant dislocation movement mechanism. The effects of dislocation climb at grain boundaries are not fully understood, they may play a role in grain boundary sliding (Frost and Ashby, 1969).

5.2.1.2 Grain-boundary sliding

Grain boundary sliding is a kinematic process which contributes to the deformation mechanisms of metals and alloys. Grain boundary sliding can occur during the plastic flow of polycrystals provided. There is deformation incompatibility among grains and the necessary accommodation mechanisms for grain boundary sliding can operate (Raj and Ashby, 1971).

At the boundary (i.e. the grain boundary) between two neighbouring grains having different crystallographic orientations, some atoms are not bonded and cause an increase in the boundary energy. Impurity atoms often segregate along the grain boundaries due to the higher energy state. It is therefore possible for deformation to occur via grain boundary sliding. As such, the grain boundaries in metals and alloys are considered as a source of weakness at elevated temperatures (Zhou and Dunne, 1996).

For instance, superplastic forming for aluminium alloys is controlled by grain boundary sliding (Raj and Ashby, 1971; Lin et al., 2006). This has led to the widely held view that grain boundary sliding can be a controlling deformation process in fine-grained materials at elevated temperatures.

5.2.2 Damage mechanisms

The deterioration of a metallic structure during plastic and viscoplastic deformation is due to nucleation, growth and coalescence of the internal defects such as microvoids and microcracks. This process is generically termed as damage. Damage has a significant effect on the mechanical properties of a metal during deformation. The internal defects in the material act as nucleation sites and induce damage (Liu, 2004). The evolution of damage is essentially related to the dominant deformation mechanism. This mechanism depends on the deformation temperature, strain rate, material microstructure and chemical composition. Different deformation mechanisms are associated with different damage types. These various damage types are discussed below.

5.2.2.1 Creep type damage

Creep is the permanent plastic deformation of a metal under static load for a prolonged period of time. Creep phenomenon is usually observed at high temperatures ($0.3T_m < T < 0.5T_m$). The static creep load is generally below the yield stress of the material, and the rate of the deformation is relatively low (Hayhurst and Storakers, 1976; Dyson, 1988).

According to Cocks and Ashby (1982), any type of structural change resulting from adverse creep deformation can lead to damage. The creep damage can be of the forms: i) voiding or cracking at a microscopic level or ii) microstructure deterioration at a microscopic level (Ashby and Dyson, 1984). Ashby and Dyson (1984) suggest that voids grow by various controlled mechanisms such as power-law creep, grain-boundary diffusion or, a combination between both.

Based on Lin's work (Lin et al., 2005), during creep deformation the presence or absence of grain boundary damage nucleation and growth is strongly sensitive to the alloy composition and processing route. When present, it reduces the size of the load bearing section, hence accelerating creep. This, in turn, increases the rate at which damage grows. Under low stress, the damage is void-like; under high stress, the voids can link to form grain boundary cracks (Lin et al., 2005). Metals can fracture by this mechanism alone, though it is more usual for multiple damage mechanisms to interact, reducing ductility. Grain boundary damage formation is a kinetic phenomenon that, in metal forming, is strongly linked to the deformation rates. The influence of damage on deformation resistance and mode of the fracture for complex stress states depends on the rate of damage nucleation and growth, which in a macroscopic sense will be controlled by material temperature, stress state and strain rate (Lin et al., 2005).

There are many researchers have been done to model the creep type damage. Some of researches are based on developing the damage variable with relation with the stress state during of the deformation and other are based on the creep rate in terms of the creep time. Summary of different creep damage model is presented below.

Kachanove, (1958), describes the creep damage process using the damage state variable, *D*, in which the material is treated as a continuum as seen in Equation 5.1(Liu, 2004):

$$\dot{D} = \left(\sigma_e / A_d\right)^{m_d} .(1 - D)^{-n} \qquad 5.1$$

where A_d, m_d, n are material constants.

For a constant stress creep condition, the damage variation with time can be determined by simple integration of Equation 5.1.

According to Cocks and Ashby (1980), creep-type damage is affected by the stress state in terms of the stress traiaxiality. Cocks presented the traiaxiality relationship as the relative change in damage rate normalised to pure tension;

$$\frac{\dot{D}^*}{\dot{D}} = sinh\left(2\frac{(n-0.5)\sigma_H}{(n+0.5)\sigma_e}\right) \Big/ sinh\left(\frac{2}{3}\frac{(n-0.5)}{(n+0.5)}\right) \qquad 5.2$$

where n is a creep material constant. σ_H , σ_e are the hydrostatic and mean stress respectively.

When metal creep occurs at high temperature, the accumulation of mobile dislocations leads to damage. Hence, the creep in the materials is not controlled by dislocation recovery, but in terms of dislocation multiplication (Liu, 2004). In the presence of mobile dislocation damage, the secondary and tertiary creep can be modelled (Lin, et al., 1996). Lin, et al., represented a damage model as follow:

$$\dot{D} = C_d (1 - D)^2 . \dot{\varepsilon}_e \qquad 5.3$$

where, $D(= 1 - \rho_0/\rho)$is the mobile dislocation damage, ρ_0 is the initial dislocation density and ρ the current dislocation density. C_d is the material constant.

5.2.2.2 Ductile type damage

Ductile damage mechanisms in metals occur under sever plastic deformation and consist of three main stages: void nucleation, growth and coalescence (Rice and Tracey, 1969). In cold forming, grain boundary sliding does not occur and the dominant deformation mechanism is the multiplication of dislocations is (Rice and Tracey, 1969). This results in voids being nucleated around the second phase and typically inside the grain. Once the voids have been nucleated, by either decohesion or cracking of the second phase/ inclusions, a stress free surface on the voids is resulted. In addition, the weakened material displays areas of localised stress and strain concentrations (Tvergaard, V. & Needleman, A., 2001).

McClintock (1968) has developed a mathematical model describing the growth of cylindrical cavities within a material during cold deformation. Rice and Tracey (1969) subsequently developed a damage model based on the rate of volume change of spherical voids. In Rice and Tracey's model, the volume changing contribution to void

growth is found to overpower the shape changing part at high mean normal stress, resulting in essentially spherical growth. In addition, Rice and Tracey found that for any remote strain rate field, the void enlargement rate is amplified for that strain rate by factor rising exponentially with the ratio of the mean stress and yield stress. The Rice and Tracey (1969) damage model is based on the concept of a void in a cylinder undergoing dilatational growth due to stress traiaxiality. Coalescence occurs once the voids grow to the point that they meet.

$$\dot{D} = \frac{exp\left(\frac{\sqrt{3}}{6}\right)}{exp\left(\frac{\sqrt{3}\sigma_H}{2\sigma_e}\right)} \qquad 5.4$$

Brozzo et al (1972) developed a simple model involving the principal stress to predict the failure strain of a material described in the following equation 5.5:

$$D = \int_0^{\varepsilon_f} \left(\frac{2\sigma_1}{3(\sigma_1 - \sigma_e)}\right) . d\varepsilon_{eq} \qquad 5.5$$

At high temperature, many metals and alloys have been experimentally observed to be subjected to plasticity induced damage under high plastic deformation. Dunne and Katramados, (1998) investigated a micromechanical damage model for titanium alloys subjected to large plastic deformations over a temperature range of 925°C-975°C and strain rate range of 0.005-5.0s-1. Dunne and Katramados's model for nucleation and growth of voids has been developed by considering the decohesion between primary alpha particles and the beta matrix in titanium alloys. The model takes the forms (Equation 5.6 and 5.7):

$$\dot{D}_{pi}^{N} = a_1\left[1 - exp\left(-a_2 D_{VF}\right)\right]\left[1 + tanh\left(a_3 \frac{1}{\sigma_e}\right)\right]\dot{\varepsilon}_e^p \quad 5.6$$

$$\dot{D}_{pi}^{G} = \beta_g\left[1/\left(1 - D_{pi}\right)^n - \left(1 - D_{pi}\right)\right]\dot{\varepsilon}_e^p \quad 5.7$$

In which $\dot{D}_{pi}^{N}$ & $\dot{D}_{pi}^{G}$ are respectively the nucleation and growth damage parameters for plasticity induced damage. I is the stress invariant, a_1 is a material dependent parameter. a_2 and a_3 are material constants. D_{VF} in the Equation 5.8 is the volume fraction of the alpha phase. β_g and n are stress-controlled material coefficients.

Tvergaard and Needleman (2001) modified the Gurson model to investigate damage coalescence close to final failure. This modification significantly increases the model's ability to predict the damage fraction and damage related material softening at final failure. The equations take the form of a modified damage dependent flow potential function:

$$\Phi = \frac{\sigma_e^2}{\sigma_y^2} + 2q_1 f^* cosh\left(\frac{q_2\sigma_H}{2\sigma_y}\right) - 1 - (q_1 f^*)^2 = 0 \quad 5.8$$

$$f^* = \begin{cases} f \ldots\ldots\ldots\ldots\ldots\ldots\ldots\ldots f < f_c \\ f_c + \frac{\left(\frac{1}{q_1} - f_c\right)(f - f_c)}{f_f - f_c} \ldots\ldots f \geq f_c \end{cases} \quad 5.9$$

The damage growth parameter f represents the total damage, including new nucleating damage voids and the growth of pre-existing voids: $\dot{f} = \dot{f}_{nucleation} + \dot{f}_{growth}$ (Tvergaard and Needleman, 2001).

5.2.2.3 Superplastic type damage

high temperature causes grain boundary diffusion, which facilitates grain rotation and grain boundary sliding, both of which are more active when the grain size is small, temperature is high and deformation rate is low, as in superplastic forming (Lin et al., 2005). However, grain rotation and boundary sliding are not restricted to these conditions and may be present to a lesser extent at faster forming rates and in alloys not capable of superplasticity. The relative displacement of grains resulting from rotation and boundary sliding is accommodated by the redistribution of matter within the mantle adjacent to grain boundaries (Lin et al., 2005). When this accommodating process is insufficient to meet the requirements of the deformation rate, stresses at the grain boundaries are not relaxed sufficiently and, consequently, cavities nucleate primarily at the triple point of the grain as seen in Figure 5.2. When a cavity is present at a grain boundary (either nucleated during superplastic deformation or existing prior to the deformation), it grows by either superplastic diffusion processes or plastic deformation (Lin et al., 2005).

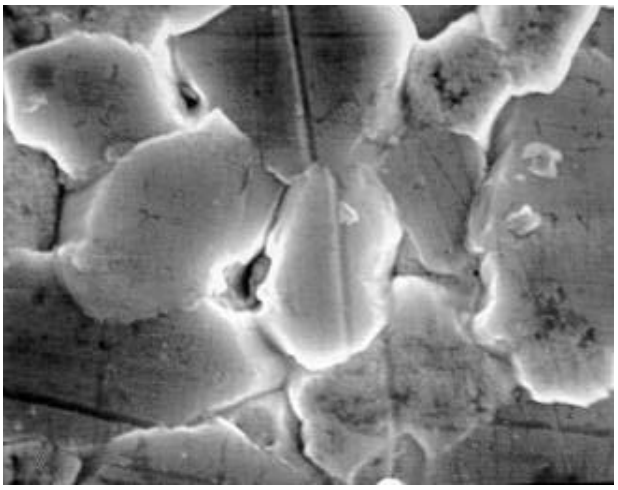

Figure 5-2 Voids at triple points of grains in superplastic forming (Lin et al., 2005)

In some alloys, the devolvement of cavitations limits the superplasticity. This is observed in aerospace aluminium alloys, where ductility in superplasticity is found to be strongly dependent on capitation processes (Dunne, et al., 1990). The ductility of the material during superplastic forming is not only controlled by the capitation process, but also by the inhomogeneous deformation and necking.

Nicolaou and Semiatin (2000) have developed a mathematical model for superplastic and general hot deformation processes. The damage growth in tension has been modelled through the classic plasticity mechanisms resulting in an equation describing the variation of damage radius r with strain,

$$r_d = r_{do} exp\left(\frac{\eta}{3}\varepsilon\right) \tag{5.10}$$

where η is an individual (volumetric) damage cavity parameter and r_{d0} is the initial cavity radius.

The stress state behaviour of superplastic type damage has been assessed by Pilling and Ridley (1986) for case of increasing compressive stress state. In Pilling and Ridley' model, tensile and biaxial deformation was conducted under increasing pressure as shown in the following equation;

$$\frac{\dot{D}^*}{\dot{D}} = 1 - 2\left(\frac{P}{\sigma_e}\right) \tag{5.11}$$

Pilling and Ridley's equation has been modified in terms of stress traiaxiality by (Nicolaous and Semian (2003) as shown in Equation 5.12.

$$\frac{\dot{D}^*}{\dot{D}} = \left(\frac{1}{3} + 2\frac{\sigma_H}{\sigma_e} \right) \quad 5.12$$

5.2.3 Damage mechanisms for aluminium alloys

5.2.3.1 Effect of second phase on damage mechanisms

The deformation process of aluminium alloys is significantly dependent on the series type. Since different second phase particles are contained in different aluminium series, the deformation and damage mechanisms will change according to the second phase properties, shape and conditions of matrix interface of the particles. As mentioned previously, during cold deformation the dominate deformation mechanism is dislocation movement which is obstacle-limited (Hansen, 1990). These obstacles increase the strength of the material and reduce the plastic flow. Obstacles include: the solute atoms as found in solution hardening series (AA5xxx) and second phase particles as in precipitation hardening series (AA2xxx, AA6xxx and AA7xxx). In addition, second phase particles can also affect the damage mechanism for aluminium alloys.

Aluminium alloys AA2xxx (i.e., AA2024) are age hardening alloys and are used in the aerospace industry due to their ability to combine good strength with fatigue resistance. AA2024 has low ductility, enabling complex-shaped parts to be formed using conventional cold forming. In general, greater ductility is observed at high temperatures, although this is not the case for all aluminium alloys. AA2024 exhibits reduced ductility at temperatures greater than about 450˚C, which is still below the SHT temperature for that alloy. At low temperature conditions ($350℃ \leq T \leq 450℃$), the dominant damage mechanism is either the debonding or fracture of second phase particles (Wang, 2010). At a temperature range of $450℃ \leq T \leq 480℃$, solute

enrichment of grain boundaries reduces the cohesion of the grain boundary. This is coupled with softening of the matrix which results in voids located around finer inclusions and leads to a mixed ductile intergranular fracture. However, at the highest forming temperatures range ($480℃ \leq T \leq 493℃$), the grain boundaries display a very low strength and the dominant damage mechanism is intergranular fracture (Wang, 2010).

In solution hardening aluminium alloys such as AA5xxx, ductility is increased at high temperatures and reduced at high strain rates. The increasing in ductility at hot temperatures is due to the increasing in strain rate sensitivity. This type of aluminium series owes its strength mainly to the second phase found in the solid solution as well as the grain size. Solid solution hardening results due to the interaction between mobile dislocations and the solute atoms. The ideal deformation temperature range for this material is 500-540ºC, in which the second phase (hardened phase) are completely dissolved inside the aluminium matrix resulting in an increase in the ductility of the material (Abedrabbo, 2006).

Smerd, et al., (2005) have investigated the effect of strain rates on the ductility and damage mechanism for AA5xxx notably AA5754 and AA5182. Smerd et al., found that as the strain rate was increased, both alloys demonstrated a significant increase in ductility. Reasons for this are not currently completely understood uncertain at this time; however, this phenomenon may be due to inertia stabilization delaying the onset of final fracture (Smerd, et al., 2005).

5.2.3.2 Specific damage mechanism for AA6xxx (AA6082) at hot forming conditions

From the damage review outlined in the previous sections, it is ascertained that damage phenomena are linked to deformation conditions (strain rate and temperature) and microstructure of the material (grain size, texture, and the second phase). For deformation at low temperatures (cold forming processes), damage accumulates at the second phase interfaces due to decohesion. At low strain rates and high deformation temperatures, damage can occur at grain boundaries or at triple points as observed in creep and superplastic deformation respectively. Constitutive damage modelling has been developed to model each type of above damage mechanisms individually as discussed previously.

It is well known that AA6xxx contains a large volume fraction of different intermetallic particles having different sizes. These particles have an important effect on the formability of the material. The most common are the plate-like β-Al5FeSi particles and the rounded α-Al12(Fe,Mn)$_3$Si particles. The brittle, β-Al5FeSi phase, which is insoluble during solution heat treatment, is associated with poor formability as acts as obstacle to the dislocation movement. These particles can either debond or fracture from the aluminium matrix. For this reason, these particles can be considered as nucleation sites for voids. Damage in AA6xxx is initiated by either decohesion or fracture of these inclusions (Lassance et al., 2007).

Several studies have assessed the behaviour of AA6xxx during hot deformation. For AA6xxx, the deformation rate is relatively high and the deformation mechanism comprises the grain boundary sliding and dislocation movement. When inclusions
Lie on the grain boundary damage features are observed at the inclusion interface.

Lassance, (2006) has studied the deformation and damage mechanisms for AA6xxx at both room and high temperatures. Lassance found that the ductility and stress levels increase with increasing strain rate. This inline with current results shown in Figure 5.5. Damage initiation occurs in these alloys by either decohesion or fracture of intermetallic inclusions. At room temperature, the damage initiation occurs due to fracture of the inclusions. However, at high temperature, the damage initiation occurs due to decohesion of inclusions. A physical schematic diagram illustrated in Figure 5.3, shows the nature of the damage evolution of AA6xxx at high temperature (Lassance, 2006).

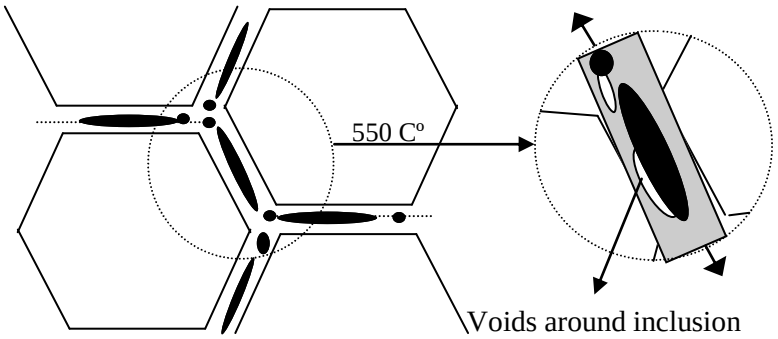

Figure 5-3 Damage initiation mechanisms in aluminium alloys AA 6xxx at high temperature (Lassance, 2006).

At high temperatures ($T > o.5T_m$), the intermetallic particles experienced a reduced stress and the damage is mostly nucleated by the inclusions/matrix decohesion. This decohesion is driven by an accumulation of plastic strain along the interface. Small intermetallic particles do not play a significant role in this mechanism. At high temperature, only the large particles play the role in the damage process (Lassance, 2006).

Lassance carried out uniaxial tensile tests for AA6060 at 550ºC with various amounts of straining. Figure 5.4 presents typical micrographs showing the damage evolution at 550ºC in AA 6060 (Lassance, 2006). It is observed form this figure that nucleation always occurs via debonding along the particle/matrix interface.

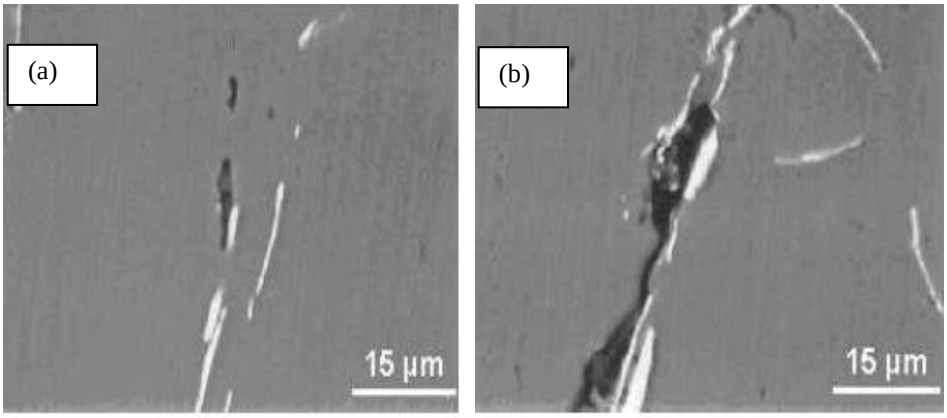

Figure 5-4 SEM micrographs showing some features of the process of (a) void nucleation and growth and (b) void growth and coalescence, the alloy AA 6060, deformed at 550ºC (Lassance, 2006).

Mrówka-Nowotnik, (2008) has obtained the same findings as Lassance, (2003) and studied the fracture mechanism in AA6082 and found that the nucleation of the voids always occurs by either fracture or debonding of the second phase along the particle/matrix interface.

In addition of Lassance's and Mrówka-Nowotnik's work, El. Danaf et al., (2008) has studied the effect of hot deformation regime (deformation temperature and strain rates) on the ductility of AA6082. EL. Danaf's found that hot deformation of aluminium alloys is controlled by dynamic recovery; the flow curves generally exhibit strain hardening until a steady state, though in some instances a moderate peak is observed.

The formations of solute atoms with the matrix hinder dislocation glide and in turn raising the flow stress. However, fine precipitates particles is a more effective source of strengthening of the alloy. Furthermore, the ductility is increased with increasing strain rate and temperature. This finding agrees with the current results presented in Figure 4.3.

5.3 Development of unified viscoplastic damage constitutive model

The experimental study of hot deformation of AA6082 in section 4.2 shows that, the flow stress response of the material may be separated into two regions. The first is concerned with the viscoplastic response, in which the overall material hardening is the results of an increase of dislocation density. The second region, which occurs at the latter stages of deformation, is related to softening due to damage, which leads to a decrease in flow stress as shown in Figures 4.3 and 4.4. A set of mechanism based unified constitutive viscoplastic equations is developed to model the evolution of the plastic flow, dislocation density, and damage evolution due to softening during hot deformation processes.

5.3.1 Viscoplastic constitutive equations

In this section a dislocation density driven incremental-plasticity model is formulated in terms of the viscoplastic flow rule, work hardening and dislocation density. At this stage, damage phenomenon is not considered.

5.3.1.1 Flow rule

The flow rule describes the relationship between the flow stress and the plastic flow rate, incorporating factors such as the initial yield, material hardening due to the interaction of dislocations, and the viscoplastic effect. The dependency of the flow stress on the temperature and strain rate is a critical concern needed to model the hot deformation process.

For ductile metals and alloys at temperatures less than $0.4T_m$, at which plastic deformation occurs by dislocation motion, the hardening stress-strain relationship is conventionally described by a power law:

$$\sigma = K\varepsilon_P^N \tag{5.13}$$

where K is material constant and N is the strain-hardening exponent.

When the temperature rises above $0.5T_m$ and thermally activated processes become significant, the flow stress becomes a function of strain rate.

$$\sigma = K\varepsilon_P^N \dot{\varepsilon}_P^m \tag{5.14}$$

where $\dot{\varepsilon}_P$ is the strain rate and m is the strain rate-hardening exponent (Lin and Dean, 2005; Lin and Dean, 2003). The terms ε_P^N, and $\dot{\varepsilon}_P^m$ model the strain hardening of the material due to the plastic deformation and plastic strain rate respectively. When rearranged, this forms a viscoplastic flow rule:

$$\dot{\varepsilon}_P = \left(\frac{\sigma}{K\varepsilon_p^N}\right)^{1/m} \quad 5.15$$

To physically model the hardening mechanism, the occurrence of the plastic flow of the material can be expressed by unified viscoplastic constitutive equations. Based on the inter-relationship of the internal state variables which are shown in Figure 5.1, the initial material has a dynamic yield point *k*. The stress potential that leads to viscoplastic material flow can be expressed as $\langle \sigma - k \rangle_+$, where the brackets indicate that only positive values are valid (Foster et al., 2007b). After sufficient plastic straining occurs, dislocation entanglement, pile-ups, etc., harden the material by an amount, R, the stress that leads to viscoplastic flow is reduced to $\langle \sigma - R - k \rangle_+$. Thus the flow rule can be modified to depend directly on the isotropic hardening and initial yield stress as shown in Figure 5.1. Equation 5.15 is replaced by:

$$\dot{\varepsilon}_P = \left(\frac{\sigma - R - k}{K}\right)^{n_1} \quad 5.16$$

where, $\dot{\varepsilon}_P$ in the Equation 5.16 is the traditional power law viscoplastic flow formulation. The material hardening R due to the plastic deformation is calculated according to the accumulation of dislocation density $\bar{\rho}$ (Lin and Dean, 2005; Lin and Dean, 2003;). n_1 is material constant. K, k , are temperature dependent parameters and can be represented by temperature dependent function (Liu and Lin, 2003):

$$K = K_0 \exp\left(\frac{Q_K}{R_g T}\right) \quad 5.17$$

$$k = k_o \exp\left(\frac{Q_k}{R_g T}\right) \quad 5.18$$

In which, R_g is the universal gas constant and Q is the activation energy.

5.3.1.2 Isotropic work hardening law

As discussed earlier, plastic straining occurs by the formation and movement of dislocations. Work hardening occurs because some fraction of the mobile dislocations remains locked in the material lattice and react with other dislocations, forming new obstacles to dislocation slip (Garrett et al., 2005).

The strain required to cause dislocation slip is heavily influenced by the length over which a dislocation can run and the dislocation slip length. As the density of dislocation increases the slip length reduces and a higher stress level is required to induce the plastic deformation (Garrett et al., 2005). Relating this to hardness, the hardening factor R, is directly related to the reciprocal of the average slip length L through which a dislocation can run. In turn, the mean slip length is governed by the inverse square of the dislocation density, $\rho^{-1/2}$. From this, the isotropic hardening, R, can be expressed in terms of the average dislocation density (Garrett et al., 2005).

$$\dot{R} = 0.5B\bar{\rho}^{-1/2}\dot{\bar{\rho}} \tag{5.19}$$

where B is temperature dependent constant and can be defined by:

$$B = B_o \exp\left(\frac{Q_B}{R_g T}\right) \tag{5.20}$$

5.3.1.3 Dislocation density evolution law

Dislocation density is presented in an averaged, normalized form $\bar{\rho}$, as used by Lin and Dean (Lin and Dean, 2005). In consideration of high temperature deformations mechanisms, static and dynamic recovery, a constitutive equation for normalized dislocation density evolution can be of the form:

$$\dot{\bar{\rho}} = A(1-\bar{\rho})|\dot{\varepsilon}_P| - C\bar{\rho}^{n_2} \qquad 5.21$$

where, A is a material constant, $\bar{\rho} = (\rho - \rho_0)/(\rho_{max} - \rho_0)$, ρ_0 the initial dislocation density and ρ the dislocation density in deformed material, where C is temperature dependent constant and can be represented by:

$$c = c_o \exp\left(\frac{-Q_C}{R_g T}\right) \qquad 5.22$$

The normalized dislocation density varies from 0 (the initial state) to 1 (the material experiences increasing plastic deformation, the saturated state of a dislocation networks). The first term in Equation 5.21 represents the development of dislocation density due to plastic strain and the dynamic recovery. The second term gives the effect of static recovery on the evolution of dislocation density. Recovery of dislocations is not a well defined phenomenon, due to the complex interaction of static and dynamic recovery mechanisms, especially at high temperatures where static recovery plays a significant role. Static recovery is a time dependent process in which annealing effectively removes dislocations from the material matrix (Liu, 2004; Foster et al., 2007b).

5.3.1.4 Unified viscoplastic constitutive equations

The dislocation based unified viscoplastic constitutive equations have been derived in terms of dislocation density evolution. The resulting unified viscoplastic equation set may take the form:

$$\dot{\varepsilon}_P = \left(\frac{\sigma - R - k}{K} \right)^{n_1}$$

$$\dot{R} = 0.5B\bar{\rho}^{-1/2}\dot{\bar{\rho}}$$

$$\dot{\bar{\rho}} = A(1-\bar{\rho})|\dot{\varepsilon}_P| - C\bar{\rho}^{n_2}$$

$$\sigma = E(\varepsilon_T - \varepsilon_P) \qquad 5.23$$

E is the Young's modulus of the material and is shown in Equation 5.24.

$$E = E_o \exp(\frac{-Q_E}{R_g T}) \qquad 5.24$$

5.3.2 Viscoplastic-damage constitutive model

According to the specific damage mechanism for AA6xxx which presented previously in section 5.2.3.2, the deformation rate is high and the deformation mechanism is combined between the grain boundary sliding and dislocation motion resulting in damage features appearing at the interface of the inclusion particularly at the grain boundaries. The damage mechanism for aluminium alloys in the current study is highly liked with that occurs at superplastic forming which is void nucleation and growth at the interface of the second phase and the matrix particularly at the grain boundary.

As a general rule, ductile fracture results from the nucleation, growth and coalescence of damage, as shown in Figures 5.3 and 5.4. This failure mode occurs in metals provided the material is deformed to a sufficient degree for a given temperature and strain rate. In observing the failure surface in aluminium alloys, it is evident that damage initiation sites are usually associated with second phase particles or non-metallic inclusions. The growth of damage in metals takes place by a combination of classical dislocation plasticity mechanisms, and superplastic mechanisms, depending on the conditions of the deformation.

Due to the lack of appropriate evidence to demonstrate the ductile fracture features under hot metal forming conditions, a series of hot tensile tests have been carried out on the AA6082 aluminium alloys for different deformation temperatures and strain rates which were presented in the previous chapter. In order to study and characterise the damage mechanism in AA6082 alloys at high temperature, metallographically prepared sections of fractured specimens, previously strained under uniaxial tension at various temperatures and strain rates, were analysed using a Scanning Electron Microscope (SEM). Small samples were cut from the tensile specimens out the necking region and ground parallel to the loading direction. These samples were then polished and etched using standard metallographic techniques.

Figure 5.3 shows SEM micrographs in which typical features of the processes of (a) void nucleation due to inclusion/matrix decohesion at grain boundaries and (b) subsequent void growth can be seen for AA6082. In this instance the test piece was deformed at 450°C and a constant strain rate of 1 s^{-1}. Figure 5.4 shows (a) voids starting to coalesce and (b) a large void opening, with the material close to final failure. In Figure 5.4, the test piece was deformed at 500°C and a constant strain rate of 10 s^{-1}.

The first occurrences of damage are at large strains (relative to the total failure strain). Nucleation always occurs by debonding along particle/matrix interfaces at grain boundaries, as shown in Figure 5.3(a) (the inclusions themselves have been ejected from the metal matrix when polishing and etching the samples). Total debonding requires additional strain, at which point the microcavities or microvoids grow quickly with increasing tensile strain, as shown in Figure 5.4, then form macroscopic cavities or cracks leading to macroscopic fracture.

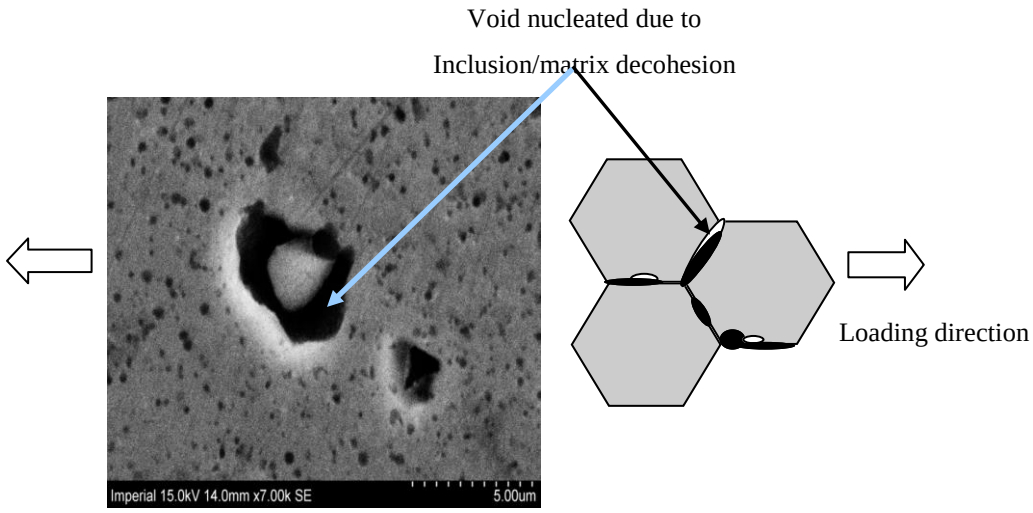

(a)

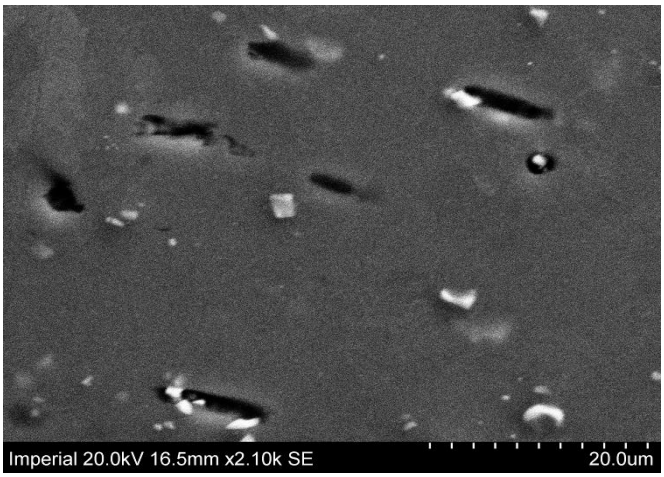

(b)

Figure 5-5 SEM micrographs showing early features of the damage mechanism (a) Void nucleation resulting from inclusion/matrix decohesion and (b) void growth in AA6082 deformed at 450 °C and a strain rate of 1 s-1.

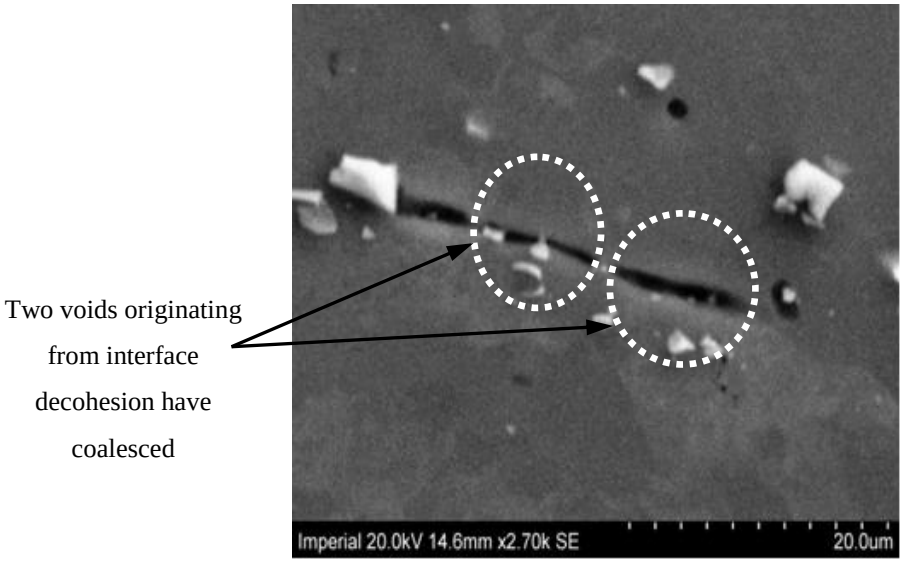

(a)

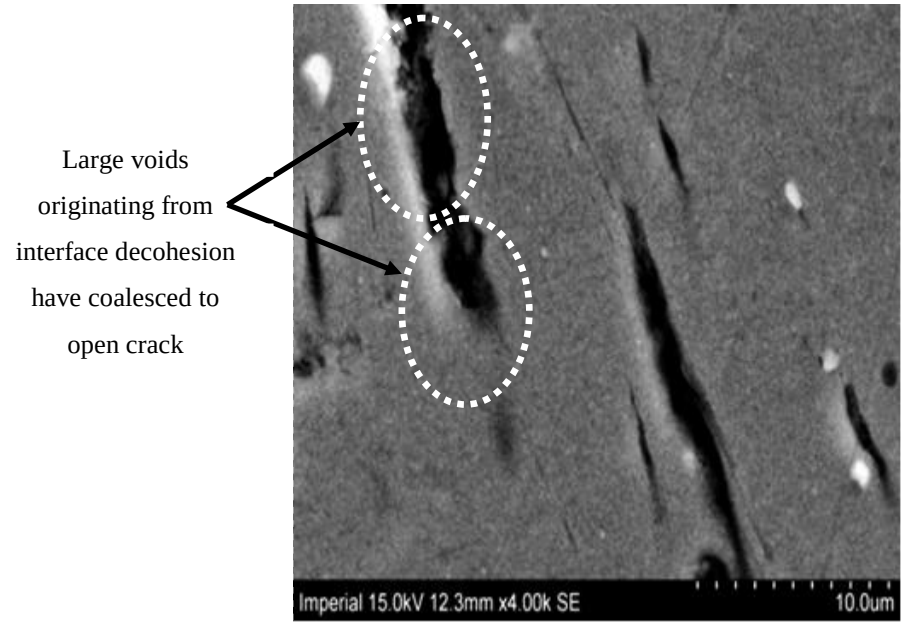

(b)

Figure 5-6 SEM micrographs showing final features of the damage mechanism: (a) Voids beginning to coalesce and (b) a large void opening and the material close to final failure for AA6082 deformed at 500 °C and a strain rate of 10 s-1.

In the late stage of deformation, softening due to damage dominates the material behaviour, and, as a result, the flow stress decreases, as shown in Figures 4.5 and 4.6). This is a result of a microstructural process of void nucleation, growth and coalescence at grain boundaries (see Figures 5.3 and 5.4). As discussed before in section 5.2.2, the dominant damage mechanisms of AA6082 is the void nucleation and growth due to the debonding of the inclusion interface particularly at the grain boundaries. A model proposed by Lin, et al. (2002) of damage in superplastically deforming materials (which occurs at grain boundaries in a manner similar to that shown in Figures 5.3 and 5.4 for hot deformation of AA6082) is adopted, where both diffusion and plasticity (power-law) induced cavity expansion are modelled. The area fraction of damaged material is defined as $f_d = r_d^2/l^2$, where r_d is an effective cavity size that includes the radial extent of the diffusion zone, and l is the cavity spacing. It is a feature of the model that if $r_d = l$, cavity growth occurs purely by diffusion, and if r_d is equal to the actual radial cavity size, then cavity growth occurs purely by power-law plasticity. Henceforth, the parameters r_d and l are not explicitly required. The damage law proposed by Lin, et al. (2002) for the evolution of f_d is expressed as:

$$\dot{f}_d = D_1 f_d^{\,d_1} \dot{\varepsilon}_P^{\,d_2} + D_2 \dot{\varepsilon}_P^{\,d_3} \cosh(D_3 \varepsilon_p) \qquad 5.25$$

where D_1 and D_2 are temperature-dependent parameters, and D_3, d_1, d_2, and d_3 are material constants. The temperature dependent parameters D_1 and D_2 are given by the following equations:

$$D_1 = D_{1o} \exp\left(\frac{Q_{D_1}}{RgT}\right) \qquad 5.26$$

$$D_2 = D_{2o} \exp\left(\frac{Q_{D2}}{RgT}\right) \qquad 5.27$$

5.3.3 Modification of the flow rule

The flow rule was modified to account for the internal reduction in cross section area caused by damage. The damage area due to growth and coalescing damage f_d reduces the area of load bearing material over which a macro stress is distributed. At a micro scale, the material is subjected to an augmented stress over the undamaged area $1-f_d$ creating an effective stress for plastic deformation of $\sigma/(1-f_d)$. The flow rule is modified thus:

$$\dot{\varepsilon}_P = \left\langle \frac{\sigma/(1-f_d) - R - k}{K} \right\rangle^{n_1} \qquad 5.28$$

The flow stress in Equation 5.23 may be modified due to the effect of softening and damage parameter, this shown in Equation 5.29:

$$\sigma = E(1-f_d).(\varepsilon_T - \varepsilon_P) \qquad 5.29$$

5.3.4 Viscoplastic damage constitutive equation set

The viscoplastic constitutive relationship may now be expanded to include damage. The equations enable a wide range of time dependent phenomena to be modelled, such as dislocation density evolution, strain hardening and damage evolution.

$$\dot{\varepsilon}_P = \left\langle \frac{\sigma/(1-f_d) - R - k}{K} \right\rangle^{n_1}$$

$$\dot{R} = 0.5B\bar{\rho}^{-1/2}\dot{\bar{\rho}}$$

$$\dot{\bar{\rho}} = A(1-\bar{\rho})|\dot{\varepsilon}_P| - C\bar{\rho}^{n_2}$$

$$\dot{f}_d = D_1 f_d^{\,d_1} \dot{\varepsilon}_P^{\,d_2} + D_2 \dot{\varepsilon}_P^{\,d_3} \cosh(D_3 \varepsilon_P)$$

$$\sigma = E(1-f_d).(\varepsilon_T - \varepsilon_P)$$

5.4 Calibration of the constitutive equations

One of the most difficult tasks encountered in developing viscoplastic constitutive equations is accurately determining the material constants from experimental data, valid over a range of temperatures and strain rates. The proposed viscoplastic damage constitutive equations consist of a set of non-linear ordinary differential equations. They can be solved using numerical integration techniques, such as Euler. The equation set has a total of 21 material constants: K_0, k_0, B_0, C_0, E_0, D_{1_0}, D_{2_0}, Q_K, Q_k, Q_B, Q_C, Q_E, Q_{D_1}, Q_{D_2}, n_1, n_2, A, d_1, d_2, d_3 and D_3. For a set of unified general viscoplastic constitutive equations, numerical integration is needed to solve the equations. The experimental data set was used to determine the material constants arising in the unified constitutive equations. The fitting technique starts with determining the boundaries of the material constants using advanced EP based optimization algorithm (Li et al., 2002). Throughout trials and errors and with a detailed understanding of the physical base of each constant, an approximate range for each constant was determined. Using a simple spread sheet, and the boundaries of the material constants, the fitting of the data is achieved by trial and error comparison between the numerical and experimental data.

The procedures to determine the material constants consist of four steps:

1. Fit the equations (i.e. determine a set of values for the material constants) to the data obtained for different strain rates and a deformation temperature of 500°C.

2. Fit the equations to the data obtained for a strain rate of $1s^{-1}$ and deformation temperature of 450°C), by changing only the values of the temperature dependent parameters (i.e., for a fixed temperature, the activation energies and coefficients of temperature dependency are not required); values of the parameters that do not depend on temperature are retained from Step 1. This leads to a second set of independent temperature-dependent parameter values.

3. Using the Arrhenius equation for temperature dependent parameters as shown in Equations 5.17, 5.18, 5.20, 5.22, 5.24, 5.26, and 5.27, the values of the coefficients and activation energies in the temperature dependencies are determined from the two independent values of each temperature-dependent parameter obtained in Steps 1 and 2.

4. The last step is validating the values of the material constants obtained from the optimization. This was done in this study by using the parameter values determined by Steps 1-3 to predict the remaining data set (strain rate of 1 s^{-1} and deformation temperature of 525°C); a good agreement indicates the parameter values are valid. More robust checking can be carried out by using the parameter values to predict further data sets not used in the optimization procedure.

By using the above-mentioned optimization procedures, the material constants in the constitutive equations were determined for AA6082 aluminum alloys and are listed in Table 5.1.

Table 5-1 Material constants for AA6082 for viscoplastic damage constitutive equations.

E_o (MPa)	C_o (S^{-1})	B_o (MPa)	k_o (MPa)	K_o (MPa)	D_{1o}	D_{2o}
322.8191	0.26	4.91	0.89	0.219	10.32	5.49E-19
Q_k (J/mol)	n_2	n_1	A	d_1	Q_E (J/mol)	d_2
6883.5	1.8	5	13	1.2	12986.72	1.01
Q_{D2} (J/mol)	Q_K (J/mol)	Q_C (J/mol)	Q_B (J/mol)	d_3	D_3	Q_{D1} (J/mol)
119804.6	27687.07	3393.46	11625.8	0.5	26.8	6408.4

The constants in Table 5.1 were used to make the model predictions (curves) for stress versus strain shown in Figures 5.5 and 5.6 demonstrate a good agreement between the model predictions and experimental results (symbols) for three different strain rates at a deformation temperature of 500°C, and different deformation temperatures for a strain rate of 1 s^{-1}, respectively.

Figure 5.7 represents the relationship between the damage parameter and the true strain for different strain rates. The damage parameter is zero (undamaged) at the beginning of the deformation, and remains zero until damage initiates, at which point the damage

parameter begins to rapidly increase as failure of the material is approached. In this way, the viscoplastic damage equations can be used to predict the viscoplastic deformation and ductile fracture of AA6082 in a hot stamping process, i.e. failure of the material (hence the failure strain) can be identified by the damage parameter attaining a critical value, taken to be 0.7 for AA6082 in this study.

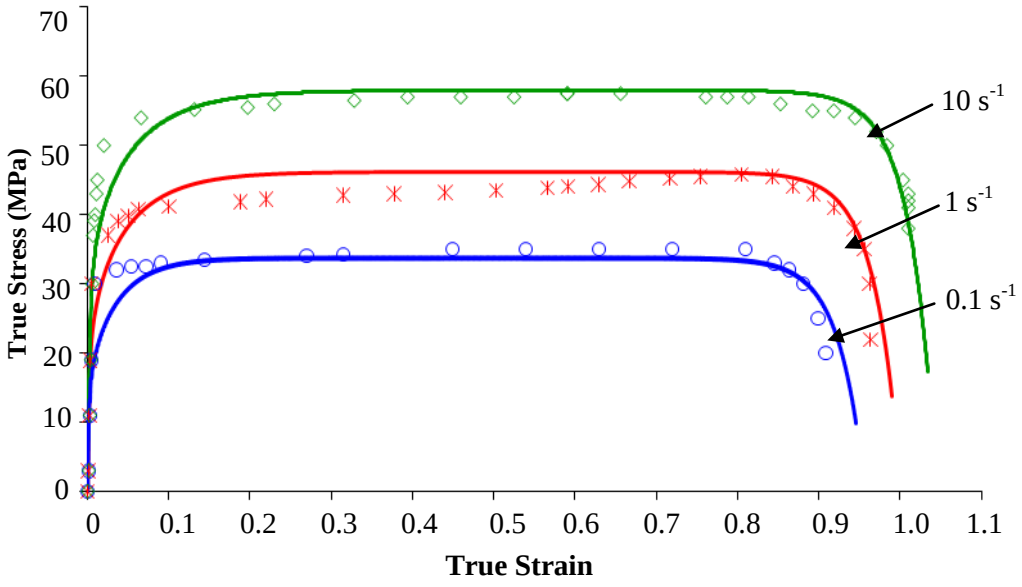

Figure 5-7 Comparison of computed (solid curves) and experimental (symbols) stress–strain relationships, for AA6082 alloy deformed at temperature of 500 °C for three different strain rates.

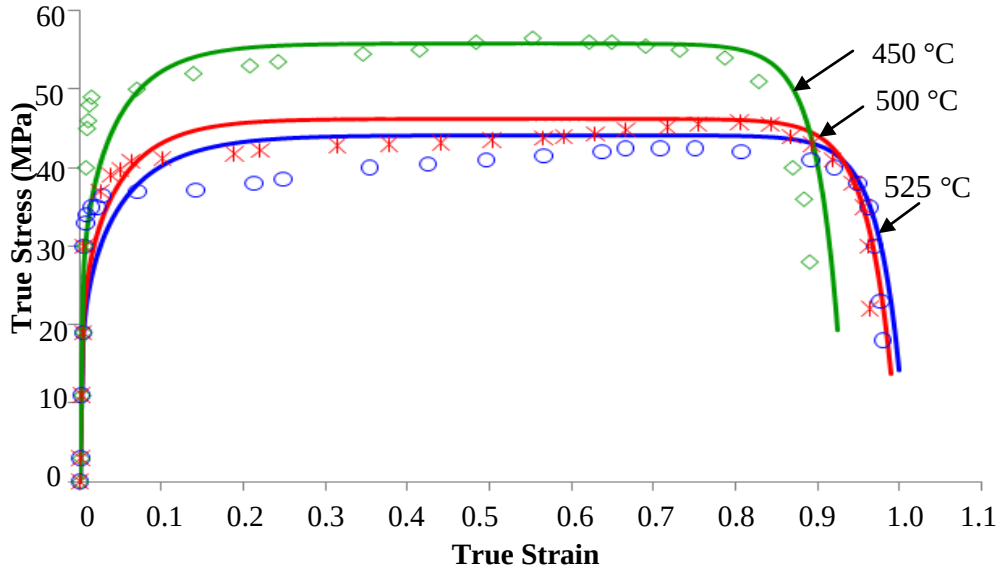

Figure 5-8 Comparison of computed (solid curves) and experimental (symbols) stress–strain relationships, for AA6082 alloy deformed at strain rate of 1s-1 for three different deformation temperatures.

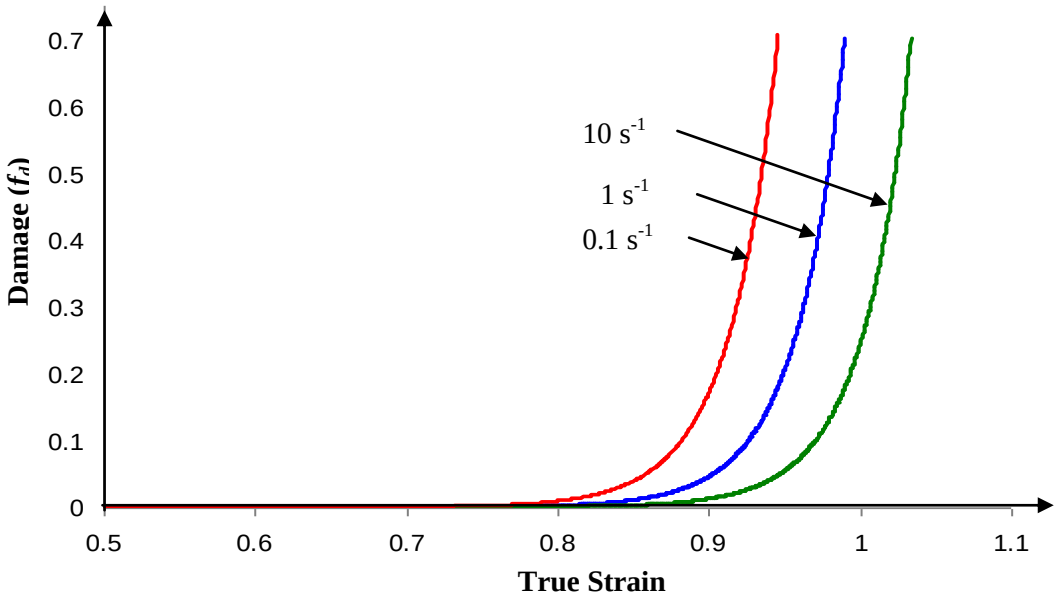

Figure 5-9 Prediction of the damage parameter for AA 6082 alloy deformed at temperature of 500°C for different strain rates.

5.5 Conclusion from viscoplastic damage model

The hot tensile deformation results presented in the previous chapter on AA6082 for the temperatures range of 525-450°C and strain rates range of 0.1–10s^{-1} have been accurately modelled using the viscoplastic-damage model. A set of viscoplastic damage constitutive equations have been developed and determined for the AA6082 at and below the SHT temperature. SEM tests have also been carried out to investigate the damage nucleation and failure features of the material. Damage normally nucleated at the interface of precipitates and the matrix material. By fitting the model described, a good prediction of experimental data has been obtained for a range of temperatures and strain rates. This confirms that the determined equations can be used to model the viscoplastic damage behaviour of AA6082. In the next chapter, this set of equations was implemented into the commercial software ABAQUS via the user defined subroutine VUMAT and used to predict failure features and formability limits in hot stamping of AA6082 panel part with a central hole.

Chapter 6

Modelling of Failure Behaviour of AA6082 in HFQ Process

6.1 Introduction

The unified viscoplastic-damage constitutive equations developed in the previous chapter was implemented in the commercial software ABAQUS via the user-defined subroutine VUMAT for carrying out forming process simulations. An FE process simulation model and numerical procedures are established for the modeling of hot stamping and cold die quenching processes for a spherical part with a central hole. The FE prediction results have been validated by the experimental observations which were developed in Chapter 4.

6.2 FE Process modelling procedures

6.2.1 Explicit FE formulation

Abaqus/Explicit is a finite element analysis package that is particularly well-suited to simulating transient dynamic events. The ability of Abaqus/Explicit to deal with the nonlinear behaviour makes it very suitable for the simulation of many quasi-static events, such as hot forming processes (Prior, 1994). In explicit solutions, the computational cost per increment depends on the size of the model, without increasing

memory or processing time as the problem size increases, such as that associated with implicit solutions. The time increment size depends only on element dimensions and the material properties, not on the analysis complexity. Therefore, an explicit method often gives results even after the analysis becomes complicated (Prior, 1994, Jung, 1998).

Dynamic simulations also model pressure waves flowing through the material. The velocity of pressure waves is governed by material mass density and the elastic modulus, requiring time increments that are usually small in comparison to the forming process time (Prior, 1994). For forming processes, where inertial effects have a insignificant impact on the result, mass scaling can be used to increase the time increment. Here material density is artificially increased. This reduces the velocity of pressure waves and thus the time increment between FE calculations can be increased.

There are certain static or quasi-static problems that can be solved properly with Abaqus/Explicit or Implicit. However, using Abaqus/Implicit to solve those problems may lead to difficulty converging because of material complexities, resulting in a very large number of iterations (Belytschko et al., 2000). While Abaqus/Implicit must iterate to solve a nonlinear problem, Abaqus/Explicit solves the problem without iterating by explicitly determining the next increment based on the previous state (Prior, 1994). In addition, the predicting of computational cost which is increased with mesh refinement in explicit is rather simple, however, in implicit is more difficult to predict.

In the dynamic code, the equation of equilibrium governing nonlinear dynamic response of a system is (Belytschko et al., 2000):

$$M\ddot{a} + C\dot{a} + Ka + f = 0 \qquad 6.1$$

In which, M, C and K are the mass, damping and spring matrices respectively, a and f are the nodal displacement and the external force vectors respectively. Abaqus/Explicit can solve the nonlinear equilibrium equations using central-difference operator (Belytschko et al., 2000). In an explicit dynamic analysis, displacements and velocities at time $t + \Delta t$ is based on the conditions of the previous step of equilibrium at time t. Therefore, the global mass and stiffness (Jacobean) matrices need not be formulated and inverted (Duni and Toniato, 2008).

To reduce the computational cost for the explicit analysis, the stable time increment should be increased and this can be achieved by increasing the density of the material. This is generally known as ‘’mass scaling’’ (Jung, 1998). Mass scaling is the most common way to control the time increment without changing the mesh size. Increasing the mass scaling level causes an increase in the kinetic energy of the moving material. However, there is a limit to the level by which the mass can be increased before inertia dominates the solution. Mass scaling should be used for problems where high frequency effects are not important. For example, in sheet-metal forming, which is essentially a static process, it causes no difficulties. On the other hand, if high frequency response is important, mass scaling is not recommended (Belytschko et al., 2000).

6.2.2 Implementation of the viscoplastic – damage model

To verify the implementation of the viscoplastic damage model in ABAQUS via the user defined subroutine VUMAT, an axisymmetric FE model was established. In the FE model, a single element was used to test the implementation of the viscoplastic

damage model in ABAQUS via the user defined subroutine VUMAT. The element type was selected as a 4-node thermally coupled axisymmetric quadrilateral, bilinear displacement and temperature (CAX4RT). The mass scaling used in this simulation is semi-automatic mass to target time increment of 1E-7.

The simulation results were comparing with the numerical integration stress strain data which were presented in Figures 5.5 and 5.6 in the previous chapter. Figure 6.1 represents an example of the comparison of the stress-strain relationships derived from numerical integration (solid curves) and FE simulation (symbols) for strain rates $1s^{-1}$ and $10s^{-1}$ at a deformation temperature of 500°C for AA6082. From the Figure, it could be seen that, the FE results is in a good agreement with the integration results. The minor differences are due to that different numerical methods are used in the numerical integration and FE simulation. This confirms that VUMAT subroutine is correct and the unified viscoplastic damage equations have been successfully implemented into ABAQUS.

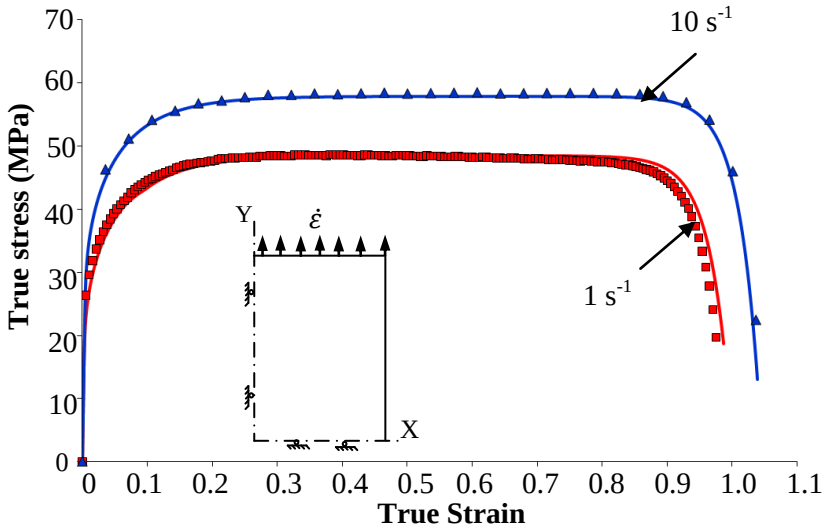

Figure 6-1 Comparison of numerical integration (solid curves) and FE simulation (symbols) stress–strain relationships for AA6082 alloy deformed at temperature of 500°C and different strain rates.

6.2.3 Formability FE model

FE simulations of round cup forming at elevated temperatures were conducted for AA6082 aluminium alloy using explicit FE code ABAQUS. In these simulations, the geometry was modelled as coupled temperature-displacement axisymmetric model. The sheet was meshed with axisymmetric elements. The VUMAT subroutine was linked with the library file to define the material properties in ABAQUS. Several issues, such as material properties, friction conditions, geometry representation, meshing method, must be considered in determining the computational cost and application of numerical process simulation:

a. Geometry

Formability FE model geometry contains four main parts: blank, hemispherical punch, top and bottom blank holders. The hot stamping process is simulated using coupled thermo-mechanical axisymmetric model. A schematic diagram of a coupled thermo-mechanical model is given in Figure 6.2. Assignment of the boundary conditions to build the CAE input file for the analysis is also shown in Figure 6.2. The blank, punch, die, and blank holder were constructed using deformable part definitions to investigate the temperature gradient and stress analysis of the specimen and the tools together.

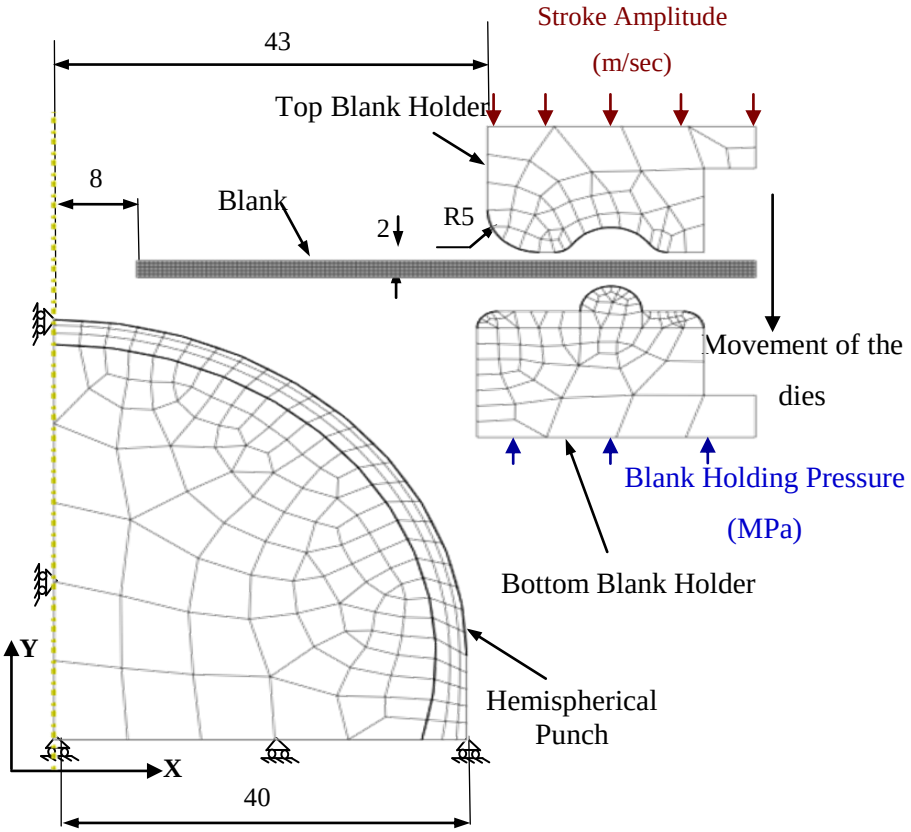

Figure 6-2 FE formability model using hemispherical punch.

b. Meshing

In a hot stamping process, the blank undergoes large plastic deformation, and the relative motion between the deforming material and the die surface is significant. Hence, the number of the elements in the blank should be big enough to obtain accurate results. To ensure that results of an analysis are not affected by changing the size of the mesh, adequate mesh density is required in the model. The formal way to establish that the mesh ensures a convergent solution is to investigate the convergence curve of a

chosen state variable in a specific region of the model where deformation is significant plotted versus mesh density.

In the FE model, a mesh was used in the blank with 4 elements through the thickness to accurately model bending of the sheet. The element type was selected as a 4-node quadrilateral, bilinear displacement and temperature (CAX4RT). The element details for blank and tools are given in Table 6.1.

Table 6-1 FE element details used in formability model.

Part / Element details	Blank	Punch	Top blank holder	Bottom blank holder
Element type	CAX4RT	CAX4RT	CAX4RT	CAX4RT
Number of elements	2230	120	46	86

c. Blank and tool material properties

In order to accurately predict the metal flow and the forming loads, it is necessary to use reliable input data. The material properties for the blank and tools used for the FE analysis are given in Table 6.2 (Foster et al., 2008).

Table 6-2 Physical and thermal properties used for the FE analysis (Foster et al., 2008).

Property	Value	Units
Density, die	7.85e-9	Tonne/mm^3
Density, blank	2.7e-9	Tonne/mm^3
Specific heat, die	5.1e8	mJ/Tonne·K
Specific heat, blank	8.9e8	mJ/Tonne·K
Thermal conductivity, die	50	mW/mm·K
Thermal conductivity, blank	170	mW/mm·K

d. Interface conditions, (friction and heat transfer)

The heat transfer conditions in the hot stamping process between the aluminium blank and the die set have a critical effect in the metal flow. Foster et al., (2008) carried out heat transfer tests for 1.5 mm thickness AA6082 and flat steel tooling. In this test, different gap distances between the sheet and the die using some ceramics spacers in order to generate accurate gap width, and different pressures were used. The calculated heat transfer coefficients which used in the current FE model are given in Table 6.3 (Foster et al., 2008).

Table 6-3 Heat transfer between the aluminium blank and steel tooling (Foster et al., 2008).

Gap width (mm)	Pressure	Heat transfer
1.05		0.04
0.6		0.07
0.0	0.0	0.8 (3.0 with lube)
	170	40.0

6.3 Formability process modelling procedures

The FE process modelling procedures and analysis was simulated in three steps:

1. In the first step, the upper die moves down in the vertical direction and deforms the sheet metal sample into drawbeads with the bottom blank holder. The hemispherical punch stayed fixed.

2. The punch remain fixed, however blank holder pressure applied based on the calculation has been done from the gas spring force and the area of the blank holder surface and It is found 3-MPa.

3. In the third step, the top, bottom blank holder, and blank sheet moves together toward the punch until given displacements are achieved.

Based on the process modeling procedures, the boundary conditions are applied on the model as shown in Figure 6.2. Apply the forming strokes according to the experimental

forming real time and speed. The applied stroke, process time and mass scaling used in the FE model for fast and slow forming rates are given in Table 6.4.

Table 6-4 The FE model details for fast and slow forming rates

Forming rate	Slow	Fast
Applied stroke (mm)	50	50
Process time (sec)	0.3	0.08
Mass scaling	5E-6	1E-6

The first objective of the process simulation was an investigation into the failure features of AA6082 during hot stamping. This was done by running the simulation under fast and slow forming rates until failure took place. The second objective of the process simulation was an examination of the spatial thickness gradient (based on normalized thickness t/t_o) of the deformed cup under different forming rates at the point in forming just before failure took place; the latter is used to develop a so-called process window, a recommended region of processing parameters for successful forming, for the hot stamping process of AA6082 aluminium alloys under different forming rates. The process window was identified by running simulations with different forming rates and different punch strokes to identify the bounds on possible combinations that lead to successful part forming (i.e. without failure or unacceptable thinning).

6.4 Validation of FE process modelling results

6.4.1 Comparison of failure features

Figures 6.3 and 6.4 show contours of the damage parameter for the fast and slow forming rates, respectively. It can be observed that ductile failure is initiated at the location of localized necking, and that location of localized necking is dependent on the forming rate. Figure 6.3 shows that, for the fast forming rate, necking occurs at the top of the cup around the central hole, and maximum damage is predicted in this area, consistent with the experimental observations. On the other hand, Figure 6.4 shows that in simulations with a slow forming rate, necking occurs in the middle region of the workpiece, circumferentially, also consistent with the experiments. Qualitatively, the simulations are in very good agreement with the experiments indicating that the damage equation is correctly formulated.

Figures 6.5(a) and 6.5(b) show the temperature profiles of blank and punch during fast and slow forming rates respectively. As mentioned before, for fast forming rate, the central region of the sheet is in contact with the punch for a shorter time, causing a smaller temperature reduction as shown in Figure 6.5(a). Therefore, the central region has a higher ductility and lower flow stress than the same region when the forming rate is slower. On the other hand, at a slow forming rate, the time elapsed when punch and sheet first come into contact until the end of forming is higher for a slower forming rate. This results in a higher temperature reduction in the region of contact as shown in Figure 6.5 (b), and, in turn, the part of the sheet in contact with the punch becomes harder than the area not in contact with the punch.

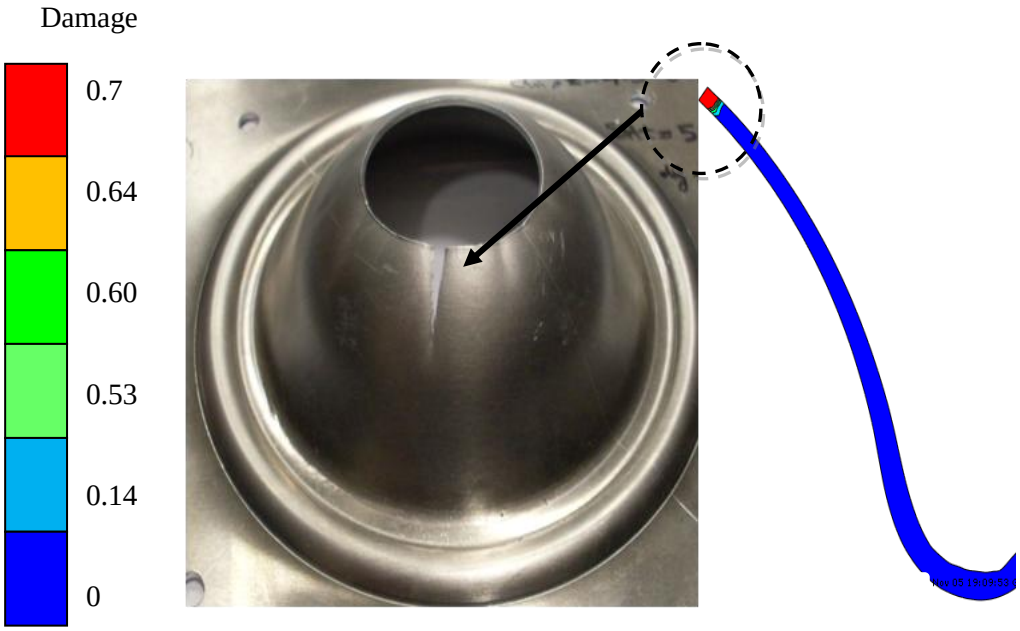

Figure 6-3 FE formability simulation results for the fast forming rate (0.64±0.01 m/sec), showing contours of the damage parameter.

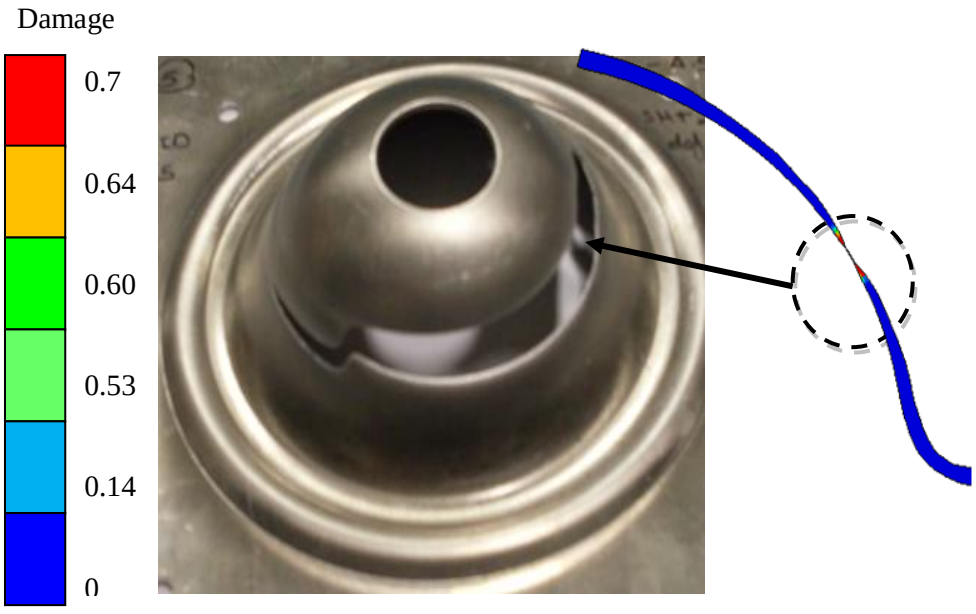

Figure 6-4 FE formability simulation results for the slow forming rate (0.166±0.01m/sec), showing contours of the damage parameter.

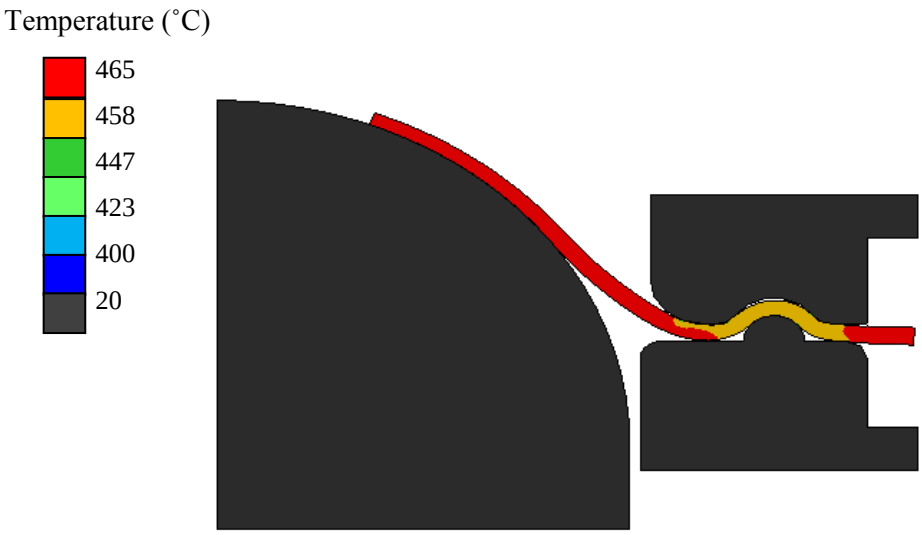

(a)

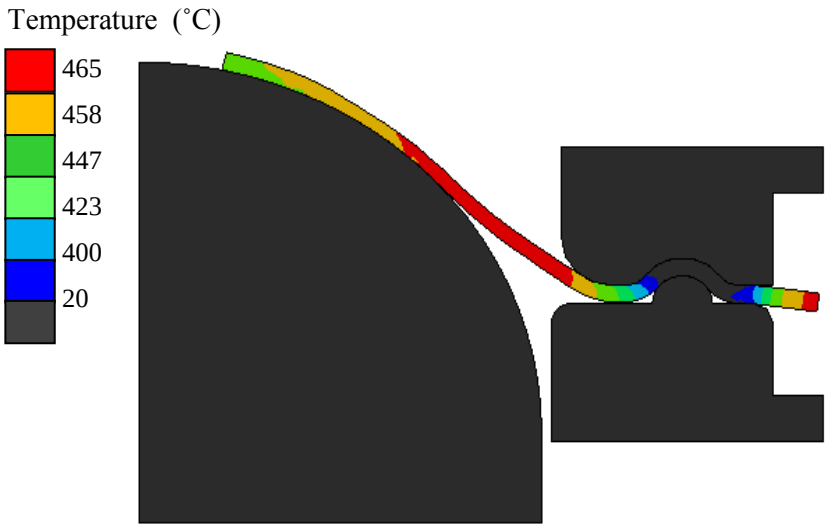

(b)

Figure 6-5 Temperature profiles of blank and punch during deformation during (a) fast, and (b) slow forming rates.

6.4.2 Comparison of thinning features

Figures 6.6(a) and 6.6(b) are direct comparisons of the experimental and simulated cup profiles, showing that the location of necking is the same for both the fast and slow forming rates, respectively. The sheet was deformed at 470 ± 10°C (in the experiments) to a state prior to failure but after the start of necking, requiring a punch stroke of 32 mm. Contours of plastic strain are also shown for the simulation results in Figures 6.6(a) and 6.6(b), where the largest plastic strain indicates the location of maximum thinning. Notably, the plastic strain is low in the mid-height circumferential region when the forming rate is high, and in the vicinity of the hole when the forming rate is low; in both cases, the plastic strain is low at the location of the drawing bead, indicating that very little drawing of material through the clamping location occurs in the simulations.

The normalized thickness (t/t_0), where t_0 is the initial sheet thickness, for physically and numerically formed parts can be measured and compared, as shown in Figure 6.7. Symbols in the figure are the experimental results, with circles representing fast forming (0.64 m/sec) and triangles slow forming (0.166 m/sec), while the solid curves are the simulation results for the two forming rates. A third, intermediate forming rate (0.21 m/sec) was simulated, given by the dashed line in the figure. Measurements were carried out for a number of tested specimens and cross sections, giving the error bars in the figure for the scatter in the measured data. There is a fairly good agreement between the experiments and simulations for both forming rates. The results in Figure 6.7 show quantitatively that the minimum value of t/t_o is at the central hole for the fast forming rate. On the other hand, for the slow forming rate, the thinnest location is shown to be at a middle height on the cup. Figures 6.3, 6.4, and 6.7 confirm that the constitutive

equations and FE model implementation are suitable for predicting deformation and failure features for hot stamping of AA6082 panel parts.

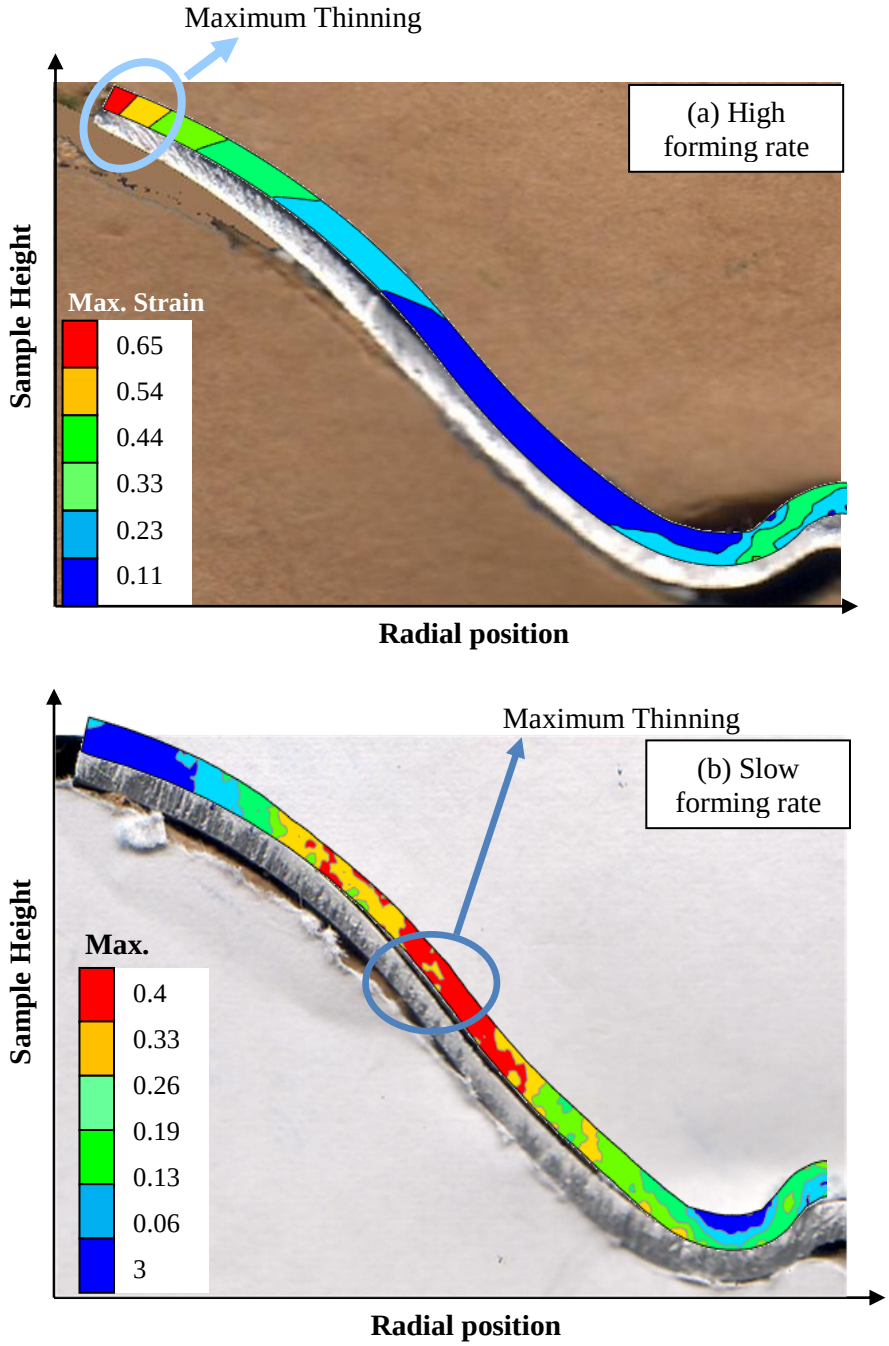

Figure 6-6 Comparison of the computational FE (coloured-plastic strain) and experimental deformed part with punch stroke 32mm and different forming rates: (a) 0.64±0.01 m /sec and (b) 0.166±0.01 m/sec.

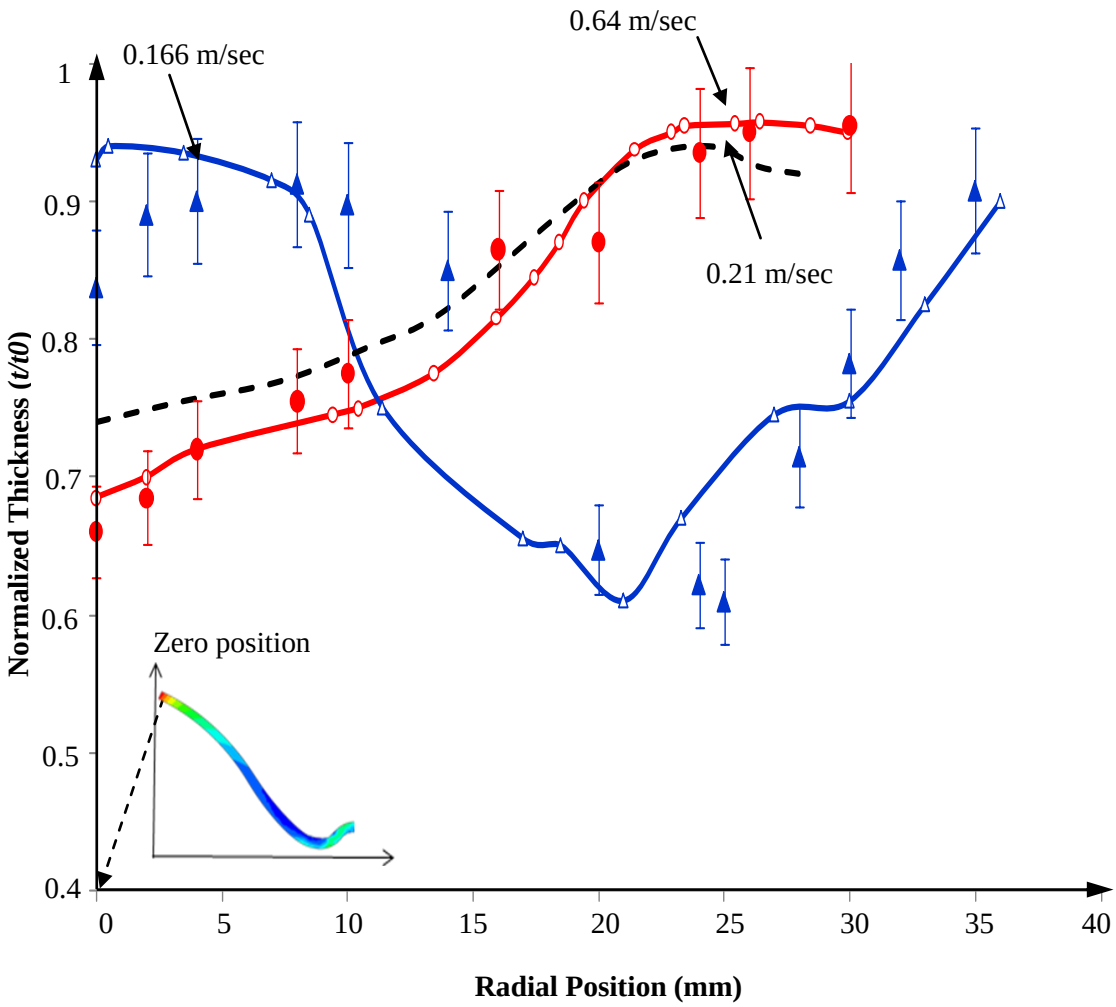

Figure 6-7 Comparison of the computational (curves) and experimental (symbols) for the normalized thickness variation of the punch stroke to 32 mm with different forming rates; 0.64±0.01 m /sec and 0.166±0.01m/sec.

Figure 6.8 shows the strain rate history ($^{\Delta\varepsilon}/_{\Delta t}$) at different regions of the deformed cup for fast and slow forming rates. From the figure, it could be seen that the first three set of curves are strain rate variation for fast forming rate (0.64 m/sec). This speed is such the extreme speed for the hot stamping process. These three curves are corresponding to different regions of the deformed cup; A, B and C. In which A is the region close to the central hole, B and C are the middle and bottom regions of the deformed cup as shown in the deformed profile in Figure 6.8. As mentioned previously, at fast forming

rate the failure takes place at the central hole, hence, the strain rate for the region A is the maximum and slightly increased the strain rate range ($0.1\text{-}10s^{-1}$) which is selected in the ductility test programme in section 3.3. This exceeding is due the localized necking occurs at this region and typically cause increasing the strain rate during deformation. Below this region, all strain rate histories are laying within the strain range as seen in curves B and C in Figure 6.8 due to the amount of deformation occurs at these regions are lower than that occur at region A.

On other side, the second three curves are the strain rate histories for slow forming rate (0.166 m/sec). The exceeding of strain rate is occurred only at middle region of the deformed sample as seen in curve B in Figure 6.8. This is due to the maximum necking occurring at this region for slow forming rate. However, the strain rate histories for regions A and C are lying within the selected strain rates range.

The viscoplastic constitutive equations set cover the strain rate range 0.1 to 10s-1 and slightly above and below this range. Hence, from Figure 6.8, it could be concluded that the hot stamping process of spherical AA6082 cups with central hole at different forming rates is accomplished nearly within the strain rates range which selected in the ductility test programme.

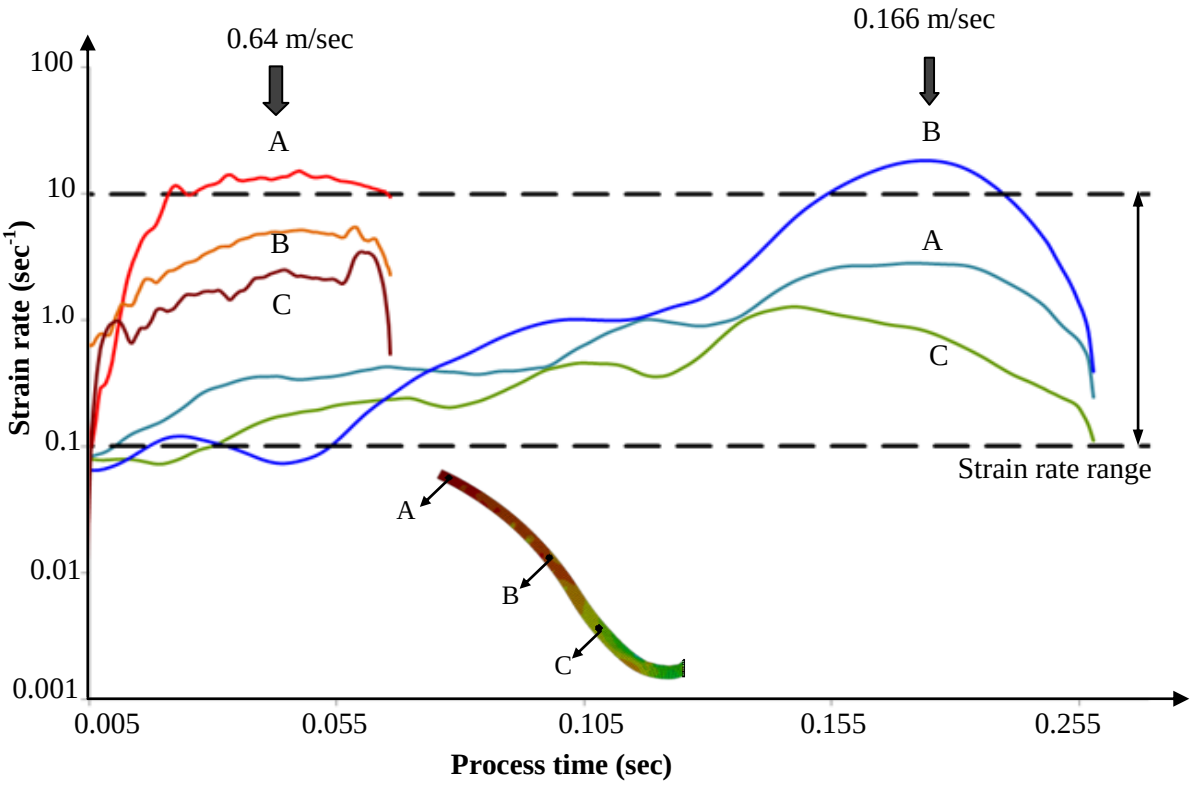

Figure 6-8 The strain rate histories at the different regions of the deformed cup for fast and slow forming rates.

6.5 Computational results

Figure 6.7 shows that significant necking and damage are observed in the central hole and middle-height cup regions for the fast and slow forming rates, respectively, in the hot stamping of the cup component. Hence, it is expected that there exists a transition region in forming rate between the failure locations, which gives a more homogenous and uniform thickness in the formed part. At the transition forming rate, thinning may occur in the central hole and mid-height cup regions to a similar degree. The transition forming rate is the optimum forming rate for the hot stamping process. To determine the optimum forming rate, a series of FE simulations were carried out with forming

rates ranging from 0.13 to 0.64 m/sec. The simulation shown in Figure 6.7 by the dashed line for a rate of 0.21 m/sec indicates the beginning of the transition to a circumferential failure mode. The thickness in the neck is greater for the 0.21 m/sec case compared to the 0.166 m/sec case. Further reduction of the forming rate towards 0.166 m/sec gives a rapidly increasing thickness in the central hole region, and as 0.166 m/sec is approached, the thinnest region moves to the middle height of the cup. It is difficult to identify precisely the optimum forming rate, but 0.21 m/sec was the most optimal forming rate tested, which enabled the part to be formed with the most uniform thickness distribution and a higher drawing depth. At the optimal forming rate, the quality of the formed part can be higher and localised necking occurs only at the much latter stage of the drawing process.

To explore this further, Figure 6.9 shows cross sections of the formed cups for simulations of the different forming rates. Again, it can be observed that the failure mode is a circumferential tear when the forming rate is low (0.13 m/sec to 0.2 m/sec). The transition to the central hole failure mode occurs between the forming rates of 0.2 m/sec and 0.23 m/sec; the thickness distribution of the 0.21 m/sec forming rate is fairly uniform (as shown in Figure 6.9).

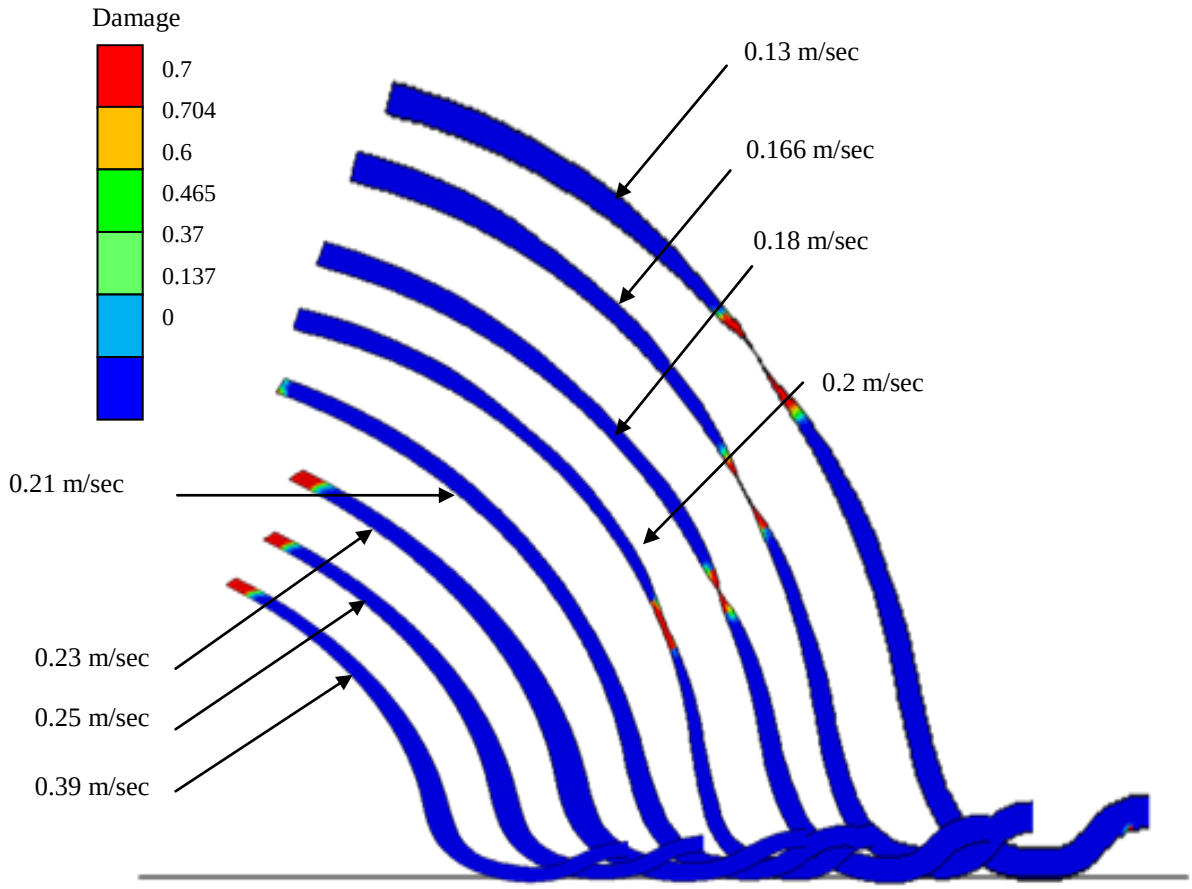

Figure 6-9 Prediction of the failure features and maximum thinning of deformed cup with the different forming rates for AA6082 aluminium alloys.

6.6 Process window to achieve high formability

For successful manufacture of a component using hot stamping, correctly choosing the process parameters is essential. The forming rate and drawing depth are the two most important parameters, which are studied in depth to define the process window for the forming process. To determine the process window numerically, a series of FE forming process simulations with different forming rates and drawing depths were carried out.

To define a boundary point of the process window for a given forming rate, a simple bisection method was used. Simulations were carried out with a forming rate of 0.166 m/sec as an example to describe the procedure. An initial guess for the drawing depth limit of 35 mm was used; the part was formed without failure (Step 1 in Figure 6.10). The next simulation was carried out with an increased drawing depth of 41.5 mm, selected according to previous experience to ensure failure would take place (Step 2 in Figure 6.10). From the first two simulation results, it can be concluded that the critical drawing depth for forming the part at a forming rate of 0.166 m/sec is between 35 mm and 41.5 mm. The next simulation was carried out with a drawing depth of 38.25mm, midway between 35 mm and 41.5 mm (Step 3 in Figure 6.10); as failure did not occur, it can be concluded that the critical drawing depth must be between 38.25 mm and 41.5 mm. The process is repeated until the critical drawing depth is identified to the required accuracy. In this case, it was found to be 38.65 mm; any drawing depth less than this can be formed at 0.166 m/sec without failure taking place. This procedure produces a single point on Figure 6.11, corresponding to a forming rate 0.166 m/sec.

Figure 6.11 shows the forming process window (determined by FE simulations) in terms of forming rate (ranging from 0.13 to 0.3 m/sec) and drawing depth. The open and solid circles are simulation results where no failure and failure occurred, respectively. Hence, the boundary between the open and solid circles in Figure 6.11 is the formability limit curve; below the curve, quality parts can be formed.

Figure 6.11 can be regarded as an overall forming process working diagram for hot stamping of AA6082 panel parts. (Pictures of tests corresponding to four different combinations of forming rate and drawing depth are shown, further indicating that good qualitative agreement was achieved between experiment and simulation). This provides

an extra confidence that the numerically determined forming process window can be used to for the production of the quality AA6082 part.

The failure region (above the forming limit curve) is divided into three parts: The transition region where the forming rate is optimal and the maximum drawing depth can be obtained with a nearly uniform part thickness, which is bounded on the left by a region where failure occurs circumferentially at a mid-height location on the formed cup, and on the right by a region where failure occurs at the central hole. Further, according to the known viscoplastic response of AA6082, a higher strain rate leads to higher ductility, which is different from the trend observed for most other materials. Therefore, the trend of the forming limit curve, shown in Figure 6.11, differs from what would be expected for a material that exhibits lower ductility at a higher strain rate, particularly at high forming rates; the expectation for such a material, in the fast forming region, is given by the dashed line in Figure 6.11.

The process window diagram in Figure 6.11 is specific to the hemispherical cup with central hole for the hot stamping process of AA6082 rounder cup with central hole. In other words, the strain rate of the hot stamping process is significantly dependant on the part geometry and in turn affects the formability limits.

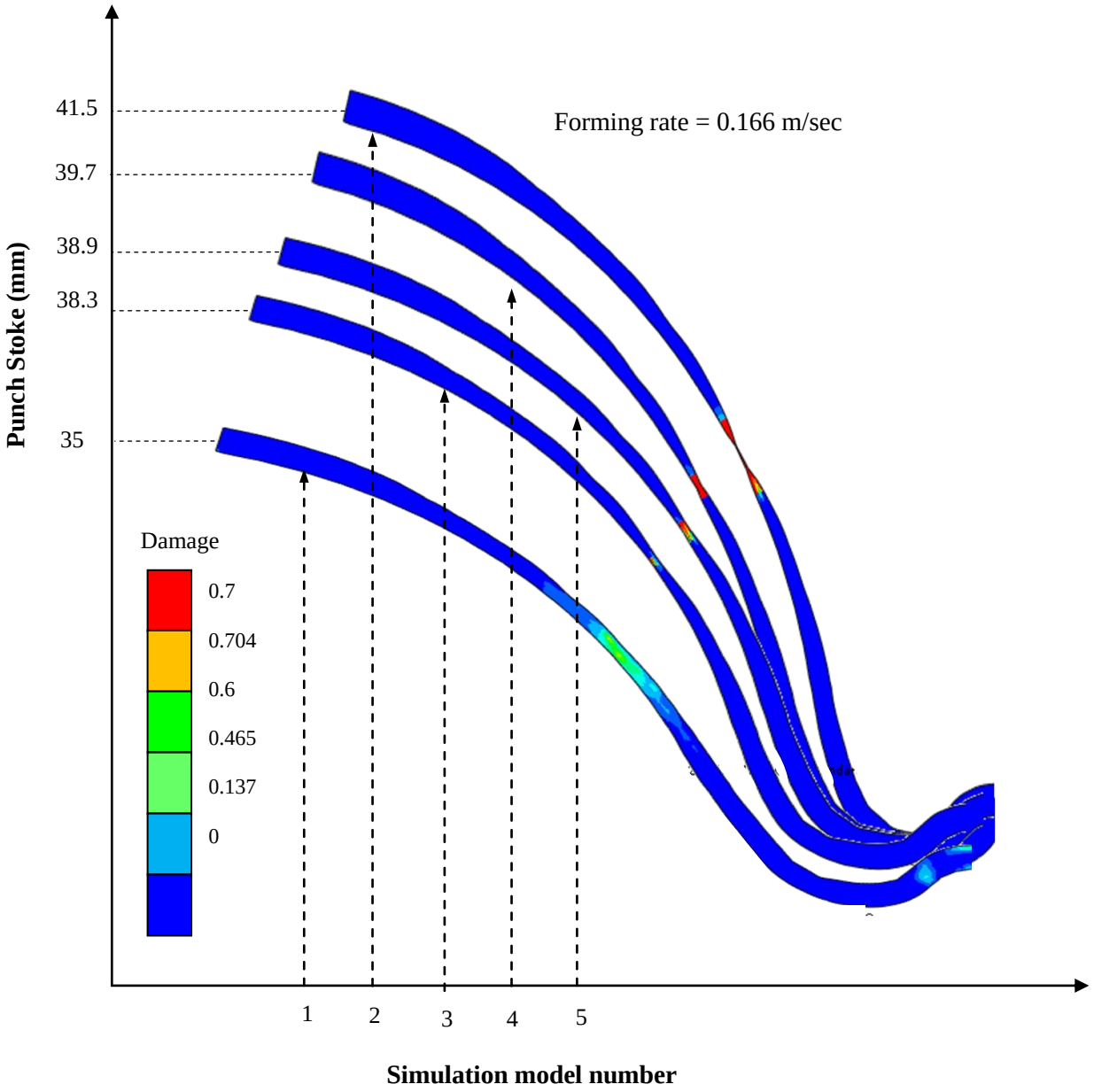

Figure 6-10 Prediction of the formability limit for forming rate 0.166 m/sec with different deformation strokes for AA6082 aluminium alloys.

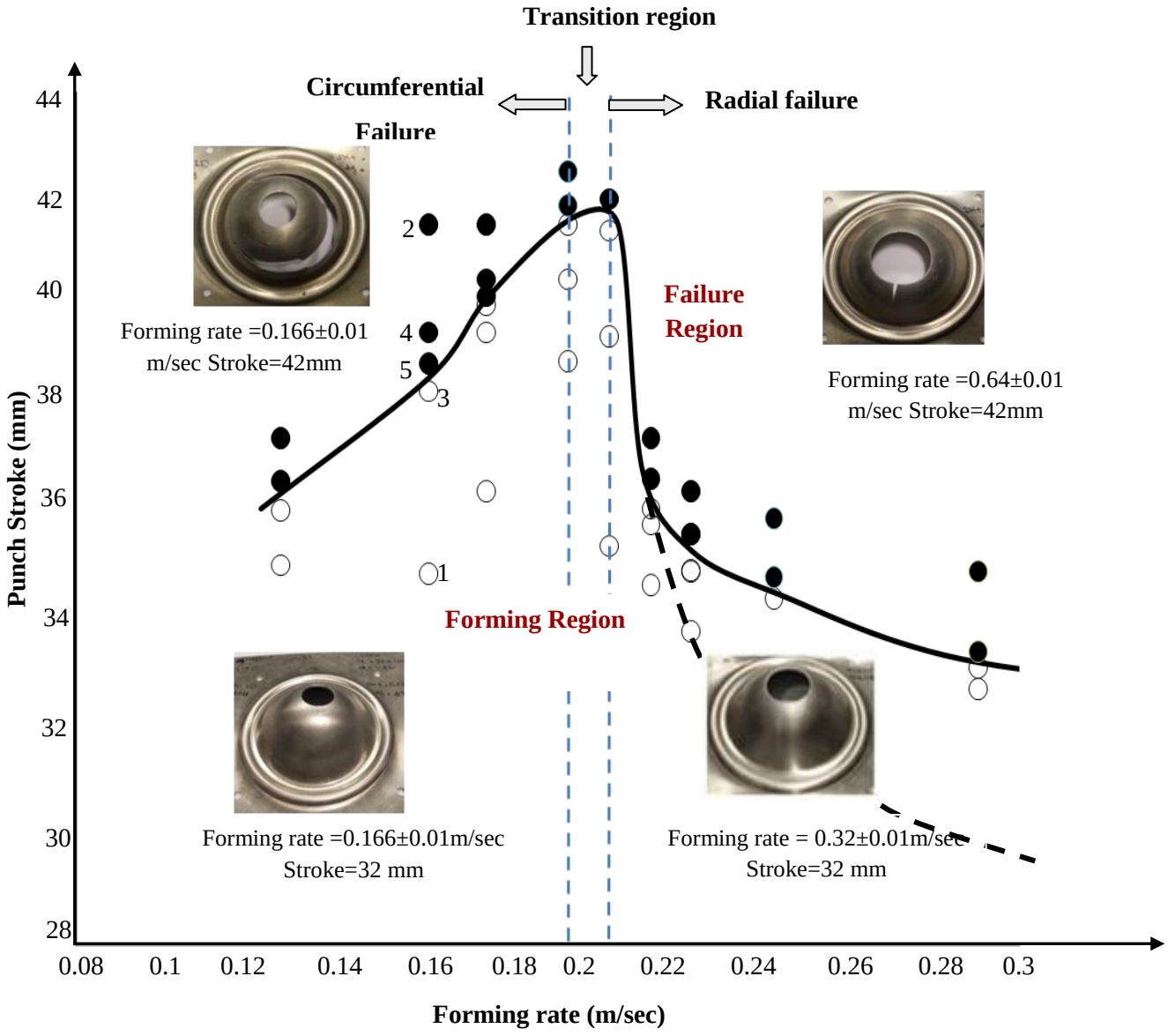

Figure 6-11 Process window diagram for prediction the process forming window and failure features for hot stamping process with different forming rates and different punch strokes for AA6082

6.7 Conclusions

In this chapter, an FE model employing a material model for viscoplastic flow and plasticity induced damage in AA6082, calibrated from experimental data, was created. The model was used to define the process window diagram for hot stamping of an AA6082 panel part with a central hole. Major conclusions drawn from this study are:

- The failure features of the AA6082 in hot stamping of panel parts are forming rate dependent. For high forming rate, the failure mode is radial tear from the centre. However, for slow forming rate, the failure mode is a tear around circumferential. The failure features have been predicted numerically and experimentally observed.

- The viscoplastic constitutive equations set which cover the strain rate range 0.1 to $10s^{-1}$ and slightly above and below this range. The hot stamping process of spherical AA6082 cups with central hole at different forming rates is accomplished within the strain rates range which selected in the ductility test programme except the tinning regions which is slightly increased the strain rate range.

- The forming process window for AA6082 hot stamping was determined by FE simulations, and was experimentally validated. The largest drawing depth and most uniform part thickness can be achieved with a forming rate of approximately 0.21 m/sec.

Chapter 7
Development of Precipitation Hardening Model

7.1 Introduction

In This chapter, the modelling of the ageing kinetics of AA6082 has been developed. The model provided the analysis and discussion of the correlation between the mechanical properties and pre-strain during artificial ageing of AA6082. The input parameters of the model consist of pre-strain levels and heat treatment parameters. The outputs of this model include property parameters namely; precipitates microstructure evolution, dislocation density evolution and yield strength. The unified precipitation hardening constitutive equation set has been formulated based on the experimental results obtained in Section 4.4 in Chapter 4. This set of equations was implemented into the commercial software ABAQUS via the user defined subroutine VUMAT to predict the post strength of a hot stamping and cold die quenching processes for a spherical part with a central hole. The FE prediction results have been validated from experimental observations.

7.2 Model methodology

The methodology of an age hardening model described in (Shercliff and Ashby, 1990) is a combination of sub-models to predict the yield strength (σ_y) or hardness values after various ageing treatments. Included in the model are expressions for:

- The decrease in solute concentration and growth in volume fraction of precipitates during ageing,
- The effect of ageing time and temperature on the ageing kinetics process (Shercliff and Ashby, 1990; Poole et al., 2000),
- The strengthening contribution from solute atoms, and
- The strengthening contribution from precipitates.

Equations describing these components are formulated as simple as possible by combining the constants into empirically significant parameters, using normalized and dimensionless variables, and using only the most essential variables to describe the microstructure and strengthening (Shercliff and Ashby, 1990; Poole et al., 2000). The methodology is consistent across the sub-models and is calibrated using experimental ageing curves.

The attempts which have been made to model the precipitation hardening are basically dependent on the determination of the yield strength of the material during ageing. The ageing kinetics parameters, which effect the strength of the material, are precipitate morphology (concentration, volume fraction, shape and size of the precipitate), and process parameters such as ageing time, ageing temperature, and dislocation density. All these parameters are investigated in most of the ageing models.

Shercliff and Ashby (Shercliff and Ashby, 1990) developed the first attempt to model the precipitation hardening for aluminium alloys. Ashby's model is based on the simple established principles of phase equilibrium, precipitate growth and coarsening, and dislocation precipitate interactions. These components are assembled into an overall process model. Ashby's model describes the ageing curves of binary AA6xxx alloys with fair success, but the complexities of the AA7xxx series are accommodated by the model.

In addition to Shercliff and Ashby model, Poole (Poole et al., 2000) and Deschamps (A. Deschamps et al., 1998) investigated the effect of the pre-strain after solution heat treatment on the artificial ageing response for AA7xxx experimentally and numerically. Based on the Poole and Deschamps results, it was observed that the kinetics of ageing was accelerated and the magnitude of the peak strength decrease in the presence of the pre-deformation. However, Baharmi et al., (2008), Dadbakhsh, et al. (2010) and Quainoo, G. K., et al., (2002) have found that the strength of the materials AA6061, AA6082, and AA6111 increases in the presence of the pre-strain respectively.

Based on all previous models, the key point of the precipitation hardening model is to identify the yield strength including the contribution of solid solution strength, precipitation strength, and dislocation strength.

7.3 Precipitation model

The precipitation model is developed based on the internal state variable approach, relating the material response of interest to microstructural variables (Shercliff and Ashby, 1990; Poole et al., 2000). The complete stages of ageing including under-aged, peak-aged and over-aged conditions are considered. The precipitation model is divided

into two main parts; precipitation microstructure evolution, and precipitation strengthening. Each part will be investigated in detail in the subsequent sections.

7.3.1 Precipitation microstructure evolution

The Johnson–Mehl–Avrami (JMA) formula can be used to describe the relationship between the volume fraction of precipitates and time at a certain temperature (Guo and Sha, 2002) as shown in the following equation:

$$f_r = 1 - exp\,(-kt^m) \qquad 7.1$$

Where, k and m are so-called JMAK parameters. This equation does not consider the effect of pre-strain on the ageing kinetics of the material. In the presence of the pre-strain, Berbenni (Berbenni, et al., 2004) found that the formation of the fine precipitates occurs mainly along the dislocations and the growth of the precipitates is dependent on the number of atoms around dislocations during the ageing. Li (Li, et al. 2010) have established a unified ageing–creep constitutive equation to describe the precipitates growth and distribution in term of precipitate kinetics, as well as precipitates hardening on the yield strength during the ageing process. In his model, the relationship between the creep forming during ageing and precipitation kinetics of AA7xxx is investigated. In the current study, the acceleration of the precipitation process was developed based on the relationship between the volume fraction and dislocation density. From Berbenni's model and Li's model, Equation 7.2 described the strain ageing kinetics mechanism in terms of the influence of the dislocation density on the relative volume fraction of the precipitates.

$$\dot{f}_r = Ar^2.(1-f_r)^{\gamma_1}.(1+\bar{\rho})^{\gamma_2} \quad 7.2$$

In which $\bar{\rho}$ is the normalized dislocation density, r is the average precipitate radius, γ_1 and γ_2 are material constants, and *A* is a temperature dependent parameter. In order to evaluate the precipitates radius, a growth law can be used to extrapolate the r data as follow;

$$\dot{r} = \frac{1}{r^2}k_1 \quad 7.3$$

In which k_1 is a temperature dependent growth rate parameter and it is related to the interfacial energy of the precipitate/matrix interface and the solubility of the precipitate elements in the matrix. Equation 7.3 can be integrated directly to give:

$$r^3 = r_0^3 + k_1 t \quad 7.4$$

In which r_o is the average radius of precipitate nuclei. To simplify the model, Equation 7.4 can be adapted in normalized form. This can be done by using a dimensionless variable ($\tau = t/t_{p_o}$), where τ is normalized time and t_{p_o} is the peak time for an undeformed sample. According to the nature of the dislocation-precipitates interaction, it is a fair approximation that when the precipitate's radius reaches to the critical radius r_c the material approaches to the peak hardness and all precipitates in the populations are non-shearable precipitates. The average critical radius is a function of the pre-strain level using the following equation:

$$\dot{r}_{c\,=} A_2(-k_2).\dot{\varepsilon}.exp\,(-k_2\varepsilon) \quad 7.5$$

where, A and k_2 are material constants. Assuming that the initial size of the precipitates is small and using Equations 7.4 and 7.5, Equation 7.3 can be then replaced by:

$$r = r_{co}.(\tau)^{1/3} \quad 7.6$$

where, r_{co} is the average critical radius in the absence of cold forming.

7.3.2 Precipitation strengthening model

In order to model the yield strength of the strain-aged alloys, the following contributions have to be considered in the precipitation model:

- Solid-solution strengthening,
- Dislocation strengthening, this is due to pre-strain prior to ageing.
- Precipitation hardening, shearable and non-shearable precipitates.

7.3.2.1 Solid solution strengthening

Solute atoms obstruct dislocation motion, contributing to the strength of the alloy. The contribution from solid solution strengthening is the maximum in as-quenched condition and then declines as the solute is removed from the matrix to form the precipitates. So, the solid solution strengthening, σ_{ss}, is related to relative volume fraction of precipitates, f_r , in the matrix (Shercliff and Ashby, 1990; Esmaeili et al., 2003; Esmaeili and Lloyd, 2005). Using the relationship given by Esmaeili et al., 2003 and considering that a fraction "α" of the initial solute concentration is depleted from the matrix when f_r approaches unity (i.e. peak-aged condition), it can be shown that:

$$\dot{\sigma}_{ss} = n_3 \alpha \sigma_{ss0}(-f_r)(1 - \alpha f_r)^{n_3 - 1}.\dot{f}_r \quad 7.7$$

In which, σ_{ss0}, is the as-quenched solid-solution flow-stress contribution, and n_3 is a constant.

7.3.2.2 Precipitation strengthening

One of the fundamental factors which determine the mechanical behaviour of the precipitates hardening is the interaction model between a dislocation and particle strength. The strength of a certain type of particle alloy is related to its size. Therefore, strengthening or softening only relates to the particles size, by growth or through coarsening.

By the definition of the critical precipitates radius r_c in Equation 7.5, then:

(1) When $r < r_c$, the particle is sheared by a dislocation - resulting in hardening;

(2) When $r > r_c$, dislocation loop across the particle - leading to softening.

In the current study, it is adequate to accept that the contribution of shearable and non-shearable precipitates to the yield strength σ_{ppt}as a function of the volume fraction of shearable particles and precipitation radius as shown in Equations 7.8 and 7.9 respectively.

$$\dot{\sigma}_{(ppt)sh} = n_3 C_1 f_r^{n_3-1}.\dot{f}_r \qquad 7.8$$

$$\dot{\sigma}_{(ppt)nsh} = C_2(1-m).r^{-m}\dot{r} \qquad 7.9$$

In which C_1, C_2 are temperature dependent parameter and ,n_4, m are material constants.

7.3.2.3 Dislocation strengthening

The normalized dislocation density of strain-aged alloys involves dislocation generation due to plastic pre-strain and dislocation recovery during ageing. The influence of pre-strain can affect the precipitation process in two ways: (1) heterogeneous nucleation can occur on dislocations, and (2) the growth and/or coarsening rate of precipitates on dislocations can be accelerated due to an enhanced diffusion rate as a result of dislocation core diffusion.

Cheng (Cheng, et al., 2003) estimated a modifying factor due to the effect of the dislocation/precipitates interaction on the recovery during ageing. Based on Cheng's model, the strength of the material is highly influenced by the rate of the dislocation recovery. During the ageing process, the dislocation density has not been completely recovered and there is some dislocation density still remaining inside the matrix. Therefore, the total dislocation density recovery can be split into locked dislocations and free or unlocked dislocations as also explained in the Berisha model (Berisha, et al., 2008). Locked dislocations are those dislocations which have interacted with the second phase inside the matrix and free or unlocked dislocations are those which did not interact.

In order to investigate the effect of pre-strain on the ageing kinetics of AA6082, dislocation density evolution (Equation 5.21) is represented in a normalised way defined with the difference of a parameter C_{ageing} introduced in Equation 7.10. This parameter represents the effect of the precipitate volume fraction on the dislocation recovery during the ageing process and it is a function of C (recovery rate) for hot deformation. The factor H in Equation 7.11 is a modification factor due to the dislocation/precipitate interactions. The amount of H at the hot deformation is equal

zero due to the precipitates being completely dissolved inside the matrix at hot deformation. Hence, Equation 5.23 can be adapted to involve the effect of precipitate volume fraction on the rate of the dislocation recovery as follows:

$$\dot{\bar{\rho}} = A(1-\bar{\rho})|\dot{\varepsilon_P}| - C_{ageing}\bar{\rho}^{n_2} \quad 7.10$$

$$C_{ageing} = C.(\frac{1}{1+H.f_r}) \quad 7.11$$

The relationship between the flow stress contribution from dislocation hardening and the dislocation density is given by.

$$\dot{\sigma}_{dis} = C_3 n_4 \bar{\rho}^{n_4-1}\dot{\bar{\rho}} \quad 7.12$$

In which C_5 and n_5 are material constants.

7.3.2.4 Combined yield strength model

The overall yield stress of the alloys is obtained by assembling the various stress contributions. The superposition of the various contributions provides the following equation for the yield strength and the corresponding hardness (Poole et al., 2000; Myhr et al., 2001; Myhr et al., 2004).

$$\sigma_Y = \sigma_{ss} + ({\sigma_{dis}}^2 + {\sigma_{ppt}}^2)^{1/2} \quad 7.13$$

$$HV = 0.33\sigma_Y + 16 \quad 7.14$$

7.3.3 Unified precipitation hardening constitutive equations

The correlation between the dislocation density, precipitate volume fraction, particularly at certain temperatures, and the pre-strain effect on the strengthening mechanism of AA6082 aluminium alloys are mathematically expressed as below:

$$\dot{f}_r = A_1 r^2 . (1 - f_r)^{\gamma_1} . (1 + \rho)^{\gamma_2}$$

$$\dot{r} = \frac{1}{r^2} k_1$$

$$r = r_{co} . (\tau)^{1/3}$$

$$\dot{r}_{c\,=} A_2(-k_2) . \dot{\varepsilon} . exp\ (-k_2 \varepsilon)$$

$$\dot{\sigma}_{ss} = n_3 \alpha \sigma_{ss0} (-f_r)(1 - \alpha f_r)^{n_3 - 1} \dot{f}_r$$

$$\dot{\sigma}_{(ppt)sh} = n_3 C_1 f_r^{n_3 - 1} . \dot{f}_r$$

$$\dot{\sigma}_{(ppt)nsh} = C_2(1 - m) . r^{-m} \dot{r}$$

$$\dot{\bar{\rho}} = A(1 - \bar{\rho})|\dot{\varepsilon_P}| - C_{ageing} \bar{\rho}^{\,n_2}$$

$$C_{aging} = C . (\frac{1}{1 + H . f_r})$$

$$\dot{\sigma}_{dis} = C_3 n_4 \bar{\rho}^{n_4 - 1} \dot{\bar{\rho}}$$

$$\sigma_Y = \sigma_{ss} + ({\sigma_{dis}}^2 + {\sigma_{ppt}}^2)^{1/2}$$

$$HV = 0.33 \sigma_Y + 16$$

7.4 Determination of material constants

The model described in the previous sections has been implemented in a simple program file using Matlab. The model is designed to handle the artificial heat treatments and different levels of pre-strain for AA6082 aluminum alloys. The equation set has a total of 18 material constants. For a set of unified general precipitation hardening constitutive equations, numerical integration is needed for solving the equations. The experimental data were used to determine the material constants arising in the unified constitutive equations. By using the above-mentioned method, the material constants in the constitutive equations were determined for AA6082 aluminum alloys and are listed in Table 7.1.

Table 7-1 Material constants for precipitation hardening model for AA6082 aluminium alloys.

A_1	γ_1	γ_2	A_2	k_2	n_3	α	σ_{sso}	n_3	H
0.55	*1.03*	*1.3*	*8*	*0.338*	*3*	*0.03*	*130*	*0.4*	*3E+9*
C_1	C_2	m	C_3	n_4	k_1	r_{co}	t_{po} *(hrs)*		
140	*630*	*2.5*	*155*	*0.5*	*3*	*3*	*9*		

7.5 Discussion and computational results

Having determined all material constants, the proposed set of constitutive equations is tested for its capability to predict the ageing hardening for AA6082 aluminium alloys at 173ºC for a number of different pre-strain levels. The results from the model for

hardness strength as function of ageing time are compared with the experimental data for pre-strain levels of 0%, 2.9%, 8.57%, and 18.57 as shown in Figure 7.1 for the AA6082 alloys. Overall, the agreement between the model and the experiments is very good. The key parameters of interest, the magnitude of the peak strength and the time to reach the peak strength are well predicted. The transition between the shearable and non-shearable precipitates was accelerated with presence of the plastic pre-strain. The model explains all changes in hardness for under-aged, peak aged, and over-aged periods.

The evolution of the precipitate volume fraction is plotted in Figure 7.2 for different pre-strain levels. It could be seen that the precipitate volume fraction grows monotonically and reaches unity at the peak age hardening. The precipitate volume fraction approaches unity faster after the material is pre-strained. From the Figures 7.1 and 7.2, the model is able to predict the ageing kinetics with different pre-strain levels.

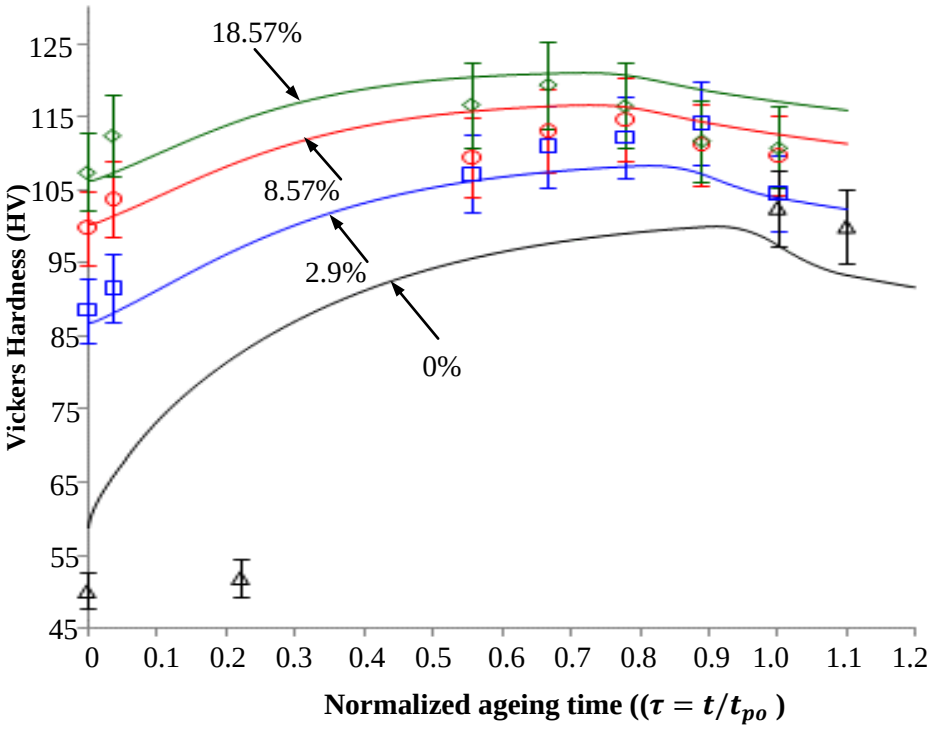

Figure 7-1 Supplemental ageing data illustrating comparison of model predictions and experimental results for AA6082 for ageing at 173ºC with prestrain amounts;

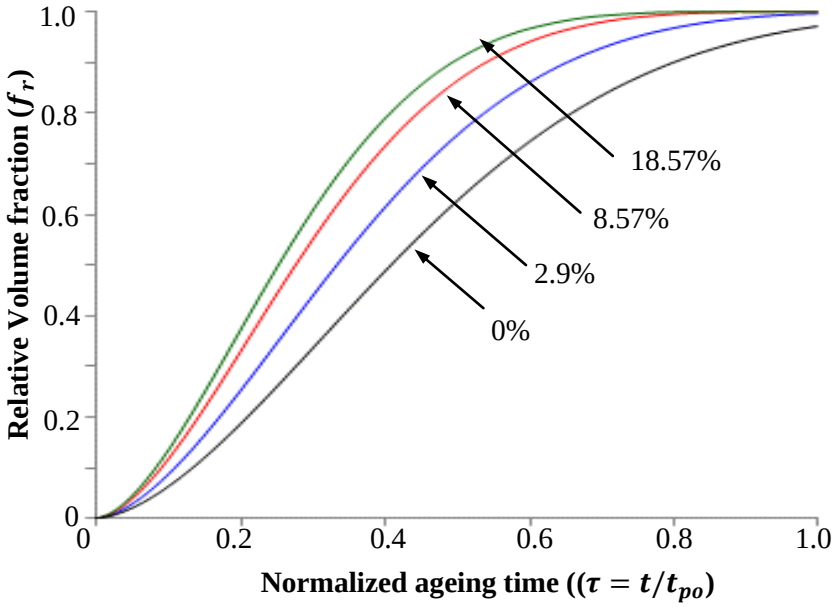

Figure 7-2 Model predictions for evolution of relative volume fraction of the precipitates with different prestrain levels of AA6082 aged at 173°C.

7.6 Process simulation and experimental validation

7.6.1 Hot stamping and ageing tests

The deformed samples for formability tests, which are shown in the Figures 4.7(b) and 4.10(b) in the Chapter 4 for slow (0.166±0.01 m/sec) and fast (0.64±0.01 m/sec) forming rates respectively, are aged at temperature of 173˚C. According to strain ageing results shown in Figure 7.1, the ageing time to reach the peak hardness of these samples is expected to be four hours. The deformed samples were sectioned. Hardness tests were carried out for particular locations (1 is a region at the central hole, 2 is a region between the centre hole and the middle region of the deformed part, 3 is the middle region of the deformed part, and finally 4 at the outer part of the sheet (undeformed region)) as shown in the coloured profile in Figures 7.3 (a) and (b).

The symbols in Figures 7.3 (a) and (b) show the variation of hardness of AA6082 for different locations of the deformed samples. Several important observations can be made from the data in such Figures, the peak hardness increases at the region with high plastic strain. In fast forming rate, the maximum thinning occurred at the top region around the central hole (region 1) of the deformed sample and in turn, the corresponding hardness is the maximum as shown Figure 7.3 (a). On the other hand, for slow forming rate, the maximum thinning occurred at the middle region (region 3) of the deformed sample and in turn the maximum hardness occurred at the same region as shown in Figure 7.3 (b). The results were used to validate of modelling results.

The determined unified precipitation hardening constitutive equations are input into the commercial FE code, ABAQUS, via the user defined subroutine, VUMAT which including the viscoplastic damage constitutive equations. An axisymmetric FE model

for the formability process simulation is shown in Figure 6.2. This is a coupled thermo-mechanical FE process simulation and the physical and thermal properties used for the FE analysis are given in (Foster et al., 2008).

7.6.2 Validation of FE Process modelling results

The predicted values (solid curves) in Figures 7.3(a) and (b) show the hardness values across the sections for the fast and slow forming rates respectively. The predicted values are higher than those of experimental data for both cases. This is because the precipitation equations are calibrated using cold initial stretching, where the final dislocation density is much higher than that of hot deformation, since static recover of dislocation at hot deformation is much higher. A technique needs to be developed to calibrate the difference of dislocations deforming at high and low temperatures with different deformation rates. However, the trends of the hardness variation across the sections are well predicted for both cases.

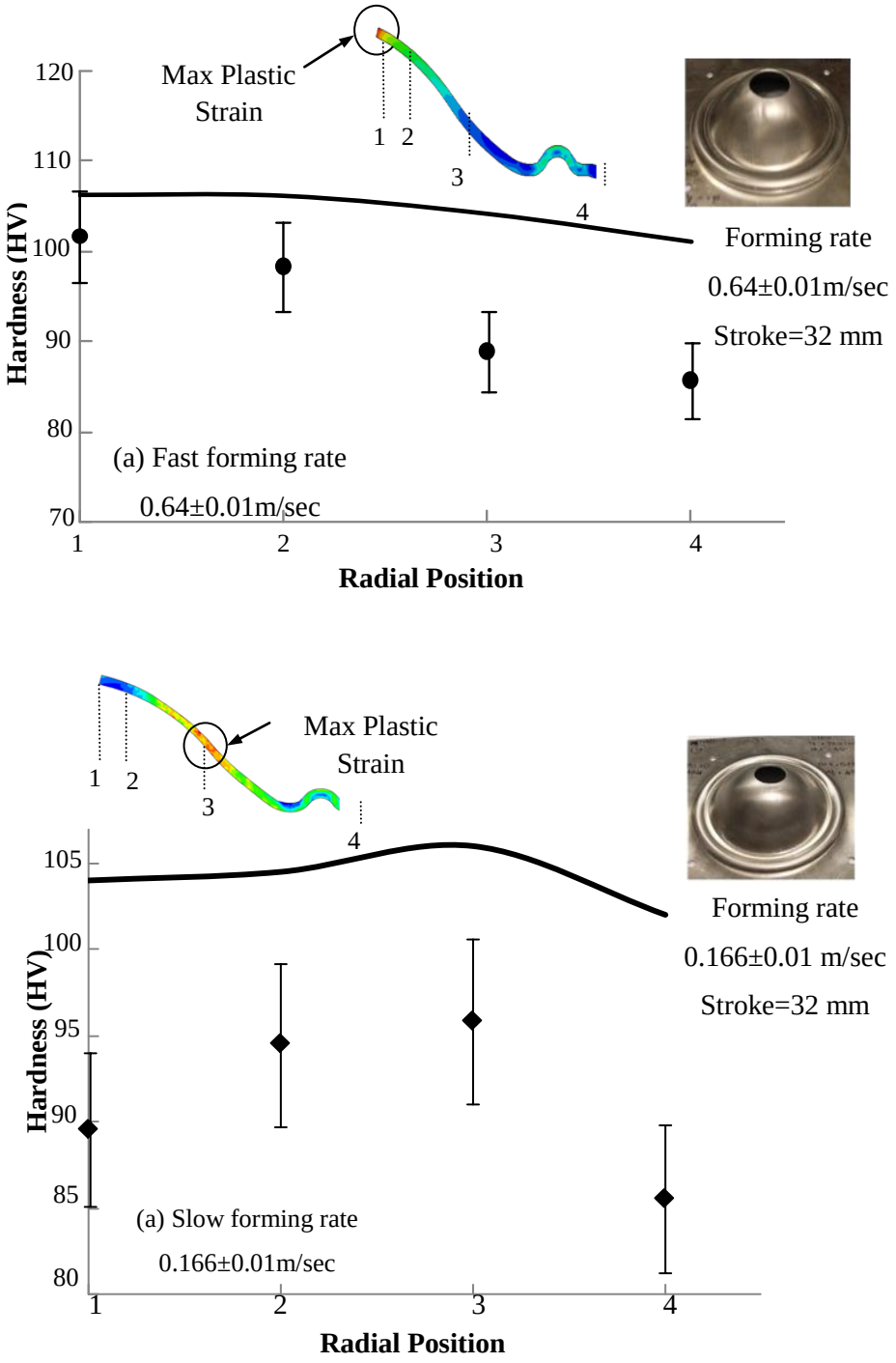

Figure 7-3 Compression of experimental (symbols) and FE (solid lines) hardness data of the formability samples for fast and slow forming rates aged at 173°C and 4 hours.

7.7 Conclusion from precipitation model

The ageing kinetics of the strain-aged AA6082 has been investigated. The work shows the following.

- A physically based model for yield strength has been developed. This model includes the effect of pre-strain on the ageing kinetics and precipitation-hardening.
- The model has been tested using the experimental results which have been represented in Chapter 4 for AA6082. The model fits and explains all changes in hardness well.
- The dislocation density evolution equation is adopted to cope with hot deformation and ageing kinetics processes.
- For all three reductions, the AA6082 alloy shows a distinct precipitation-hardening effect. The ageing kinetics accelerated with presence of the cold-stretching and the hardness increased in terms of effect of the dislocation density which plays a main role as nucleation sites for the precipitates.
- The equations, coupled with the FE model, can be used to predict the material hardness at hot stamping conditions. Regarding the precipitation hardening, the equations can be used to predict the trends very well, although the values are with certain level of differences.

Chapter 8
Conclusions, Discussion and Suggestions for Future Work

8.1 Conclusions

8.1.1 Viscoplastic damage model of AA6082

The material behaviour can be described by modelling the evolution of plastic flow potential, isotropic hardening, dislocating density and damage criteria. A series thermo-mechanical tests have been carried out on AA6082 and it has shown that at high strain rate, the ductility is higher, which is different from the commonly observed features of other materials. SEM tests have also been carried out to investigate the damage nucleation and failure features of the material. Damage normally nucleated at the interface of precipitates and the matrix material. A set of viscoplastic damage constitutive equations have been developed and determined for the AA6082 at and below the SHT temperature. By fitting the model described, a good prediction of experimental data has been obtained for a range of temperatures and strain rates. This confirms that the determined equations can be used to model the viscoplastic damage behaviour of AA6082.

8.1.2 Failure behaviour and process window of HFQ process of AA6082

The set of viscoplastic damage constitutive equations was implemented into the commercial software ABAQUS via the user defined subroutine VUMAT and used to predict failure features in hot stamping of AA6082 panel part with a central hole.

Firstly, the implementation of the set of viscoplastic damage constitutive equations into Abaqus/Explicit is tested by developing an axisymmetric uniaxial FE model with a single element and comparing with the stress-strain data obtained by numerical integration which is presented in Chapter 5. The FE results are in good agreement with the integration results.

Secondly, an FE formability model has been created and a test programme has been developed to validate the numerical process. It has been successfully used to numerically define the process window for hot stamping of an AA6082 panel part with a central hole. Major conclusions drawn from this study are as follows.

- The failure features of the AA6082 in hot stamping of panel parts are forming rate dependent. For high forming rate, the failure mode is radial rip from the centre. However, for slow forming rate, the failure mode is a rip around circumference. The failure features have been predicted and experimentally observed.

- The forming process window for AA6082 hot stamping was determined by FE simulations, and was experimentally validated. The largest drawing depth and most uniform part thickness can be achieved with a forming rate of approximately 0.21 m/sec.

Physically based, alloy-specific material models, calibrated by experimental data, can be used with commercial FE software to successfully determine forming limit curves where otherwise many time consuming and costly tests would be needed. This approach constitutes a virtual metal forming process design procedure, which may be readily extended to other alloys if material models and data are available. The forming limit diagram obtained in Chapter 6 is specific to the hemispherical cup with central hole. In other words, the strain rate of the hot stamping process is significantly dependant on the part geometry and in turn affects the formability limits.

The viscoplastic constitutive equations set cover the strain rate range 0.1 to 10 s-1. Hence, from Figure 6.8, it could be concluded that the hot stamping process of spherical AA6082 cups with central hole at different forming rates is accomplished within the strain rate range that was selected in the ductility test programme.

8.1.3 Precipitation hardening model

The precipitation hardening model has been developed to predict the yield stress in AA6982 alloys with different levels of pre-strain after solution treatment. The model uses the radius and volume fraction of the precipitates as variables. The role of the precipitate size distribution is empirically accounted by defining the average radius at which all precipitates are non-shearable. The change in precipitate size is described using a normal coarsening theory, and volume fraction of precipitates is a function of the dislocation density generated from different levels of pre-strain after solution treatment.

The precipitation-hardening response is calculated based on the interaction between the precipitates radius and the dislocation in terms of shearable and non-shearable

precipitates. The work-hardening behaviour of the alloy is described well by a power-law hardening law.

The model has been trained and subsequently tested using the experimental results which have been mentioned in Chapter 4 for AA6082. The model fits and explains all changes in strength and hardness well. All parameters in the model are within ranges that can be expected on the basis of microstructural investigations and literature data. The dislocation density evolution equation is adopted to cope the hot deformation process and ageing kinetics process.

For all three reductions, the AA6082 alloy shows a distinct precipitation-hardening effect. The ageing kinetics accelerated with cold- stretching and the hardness increased in terms of the effect of the dislocation density which plays a main role on the precipitation process nucleation sites for precipitates.

8.2 Recommendations for future work

This thesis has advanced the understanding of material mmodelling and experimental investigation for AA6xxx during hot forming process including the viscoplastic damage model and advanced precipitation hardening model which characterises the effect of the pre-hot deformation on the ageing kinetics of the aluminium alloys. The constitutive modelling of hot forming processes has many challenges and shows good promise for future work. A technique needs to be developed to calibrate the difference of dislocations deforming at high and low temperatures with different deformation rates.

Much of this work can be transferable to other metals. In additions, the constitutive material models will continue to be an important method of describing complex material behaviour for the foreseeable future.

References

Abedrabbo, N., Pourboghrat, F., & Carsley, J., (2006), Forming of aluminum alloys at elevated temperatures – Part 1: Material characterization. *International Journal of Plasticity*, 22, 314–341.

ArcelorMittal, (2008), Steels for hot stamping, E. edition.

Ashby, M.F., (1983), Mechanisms of deformation and fracture, Advances in applied mechanics, (23), 117-172.

Ashby, M.F., (1970), The deformation of plastically non-homogeneous materials. *Philosophical Magazine*, 21(170), 399 – 424.

Ashby, M. F., & Dyson, B. F., (1984), Creep damage mechanics and micromechanisms. IN VALLURI (Ed.) *Advances in Fracture Research*. Oxford, Pergamon.

Azushima, A., Kopp, R., et al. (2008), Severe plastic deformation (SPD) processes for metals. CIRP Annals - Manufacturing Technology, 57(2), 716-735.

Bahrami, A., Miroux, A., Kestens, L., (2008), An age hardening model for interrupted ageing of the alloy AA6061. *Steel Research International*, 79 (11), VII, 224-231.

Berhenni, S., Faviera, V., Lemoineb, X., Berveillera, M., (2004), A micromechanical approach to model the bake hardening effect for low carbon steels. *Scripta Materialia*, 51(4), 303-308.

Belytschko, T., Liu, W.K., Moran, B., 2000, Nonlinear finite elements for comtinue and structure. *Northwestern university, Evanston, Illinois.*

Berisha, B., Hora, P., Wahlen, A., (2008), A dislocation based material model for warm forming simulation. *International Journal of Mater Form*, 1,135–141.

Birol, Y., (2005), Pre-ageing to improve bake hardening in a twin-roll cast Al-Mg-Si alloy. *Materials Science and Engineering*, A391 (1-2), 175-180.

Brozzo, P., Deluca, B., & Redina, R., (1972), A new method for the prediction of formability limits in metal sheets. *7th Biennial Conference of the International Deep Drawing Research Group.*

Burger, G., Gupta, A. K., et al. (1995), Microstructural control of aluminum sheet used in automotive applications. *Materials Characterization Microstructural Characterization of Lightweight Structural Materials Transportation*, 35(1), 23-39.

Carrick, R. N., (2009), High Temperature Deformation Behaviour of an Al-Mg-Si-Cu Alloy and Its Relation to the Microstructural Characteristics, MSc. thesis, University of Waterloo, Applied Science in Mechanical Engineering Waterloo, Ontario, Canada.

Cantor, B., Grant, P., Johnston, C., (2008), Automotive Engineering Lightweight, Functional, and Novel Materials. *M. a. S. a. Engineering.*

Cheng, L.M., Poole, W. J., Embury, J. D., and Lloyd, D. J., (2003), The Influence of Precipitation on the Work-Hardening Behavior of the Aluminum Alloys AA6111 and AA7030. *Metallurgical and materials transactions*, A 34A, 2473-2481.

Cocks, A. C. F., & Ashby, M. F., (1980), Intergranular fracture during power-law creep under multiaxial stresses. *Journal of Metal Science*, 14, 395-402.

Cocks, A. C. F., & Ashby, M. F., (1982), On creep fracture by void growth. *Progress in Materials Science*, 27, 189-244.

Cocks, A. C. F., (1985), The nucleation and growth of voids in a material containing a distribution of grain-boundary particles, Acta Metallurgica, 33(1), 129-137

Cole, G., Sherman, A. M., (1995), Light weight materials for automotive applications. Materials Characterization Microstructural Characterization of Lightweight Structural Materials Transportation, 35(1), 3-9.

Dadbakhsh, S., Taheri, A. K., et al. (2010), Strengthening study on 6082 Al alloy after combination of ageing treatment and ECAP process. *Materials Science and Engineering*, In Press, Accepted Manuscript.

Deschamps, A., and Brechet, Y., (1998), Influence of predeformation and ageing of an Al-Zn-Mg alloy—II, Modeling of precipitation kinetics and yield stress. *Acta Materialia*, 47(1), 293-305.

Dunne, F. P. E., Othman, A. M., Hall, F. R., & HAYHURST, D. R., (1990), Representation of uniaxial creep curves using continuum damage mechanics. *International Journal of Mechanical Sciences*, 32, 945-957.

Dunne, F. P. E., HAYHURST, D. R., & LIN, J., (1996), Physically-based temperature dependence of elastic-viscoplastic constitutive equations for copper between 20 and 500°C. *Philosophical Magazine A*, 74, 359-382.

Dunne, F.P.E. and Katramados, I., 1998, Micro-mechanical modelling of strain induced porosity under generally compressive stress states. *International Journal of Plasticity*, 14(7), 577–595.

Duni, E., Toniato, G., (2008), Vehicle Fatigue Load Prediction based on Finite Element TIRE/ROAD Interaction implemented in an Integrated Implicit-Explicit Approach *Abaqus Users' Conference 1.*

Dyson, B. F., (1988), Creep and fracture of metals: mechanisms and mechanics. Revue. *De Physique Appliquee*, 23, 605-613.

El-Danaf, E.A., AlMajid, A. A., Soliman, M. S., (2008), Hot deformation of AA6082-T4 aluminum alloy. Journal of Materials Science, 43, 6324-6330.

El-Danaf, E.A., AlMajid, A. A., Soliman, M. S., (2009), Effect of Solution Heat Treatment on the Hot Workability of Al-Mg-Si Alloy. J *Journal of Materials Science*, 24, 637 - 643.

Esmaeili, S., and Lloyd, D. J., (2005), Modeling of precipitation hardening in pre-aged AlMgSi (Cu) alloys. *Acta Materialia*, 53(20), 5257-5271.

Esmaeili, S., Lloyd, D. J., Poole, W. J., (2003), Modeling of precipitation hardening for the naturally aged Al-Mg-Si-Cu alloy AA6111. *Acta Materialia*, 51(12), 3467-3481.

Foster, A., Lin, J., Dean, T., (2007a), Hot stamping and cold die quenching for producing ultra high strength automotive safety parts. *Mechanical and Manufacturing Engineering, Birmingham*.

Foster, A., (2007b), Modeling damage evolution during the hot deformation of free machining steels. *Degree Doctor of Philosophy,* 1-178.

Foster, A., (2008), Giving Aluminum the hot cold treatment. Confederation of British Metalforming, Metal Matters, 11, www. Britishmetalforming. com.

Foster, A., Mohamed, M., Lin, J., Dean, T., (2008), An investigation of lubrication and heat transfer for a sheet aluminum Heat, Form-Quench (HFQ) process. *Steel Research International*, 79 (11), VII, 133-140.

Frost, H. J., Ashby, M. F., (1969), Deformation-Mechanism Maps, The Plasticity and Creep of Metals and Ceramics, by Harold J Frost, Dartmouth College, USA, and, Cambridge University, UK.

Garrett, R. P., Lin, J., and Dean, T. A., (2005), An investigation of the effects of solution heat treatment on mechanical properties for AA 6xxx alloys: experimentation and modelling. *International Journal of Plasticity*, 21(8), 1640-1657.

Golovashchenko, S., and Krause, Al., (2005), Improvement of formability of 6xxx aluminum alloys using incremental forming technology. *Journal of Materials Engineering and Performance*, (14), 503-507.

Quainoo, G.K.", Yannacopoulos, S., (2004), The effect of cold work on the precipitation kinetics of AA6111 aluminum. *Journal of Materials Science*, 39, 6495-6502.

Guo Z. and Sha, W., (2002), Quantification of precipitation hardening and evolution of the precipitates. *Materials Transactions*, 43(6), 1273-1282.

Hansen, N., (1990), Cold deformation microstructures, *Materials Science and Technology*. 6, 1039-1047.

Hayhurst, D. R., Lin, J., Hayhurst, R. J., (2008), Failure in notched tension bars due to high-temperature creep: Interaction between nucleation controlled cavity growth and continuum cavity growth. *International Journal of Materials Processing Technology*, 45, 2233-2250.

Hodkinson, R., and Fenton, J., (2000), Lightweight construction materials and techniques Lightweight Electric/Hybrid Vehicle Design. Oxford, Butterworth-Heinemann, 173-198.

Jeswiet, J., Geiger, M., Engel, U., Kleiner, M., Schikorra, M., Duflou, J., Neugebauer, R., Bariani, P., Bruschi, S., (2008), Metal forming progress since 2000. *CIRP Journal of Manufacturing Science and Technology*, 1(1), 2-17.

Jung, D. W., (1998), Study of Dynamic Explicit Analysis in Sheet Metal Forming Processes Using Faster Punch Velocity and Mass Scaling Scheme. J*ournal of Materials Engineering and Performance*, 7(4) 1998-479.

Kachanov, L. M., (1958), Rupture time under creep conditions. *Izvestia Akademii Nauk, SSSR, Otdelenie tekhnicheskich nauk*, 8, 26-31.

Kim, T-W., and F. P. E. Dunne, F. P. E., (1999), Modeling heterogeneous microstructures in superplasticity. *Proc. R. Soc. Lond*, A 455, 701.

Kim, H. S., Koç, Muammer, Ni, Jun, (2007), A hybrid multi-fidelity approach to the optimal design of warm forming processes using a knowledge-based artificial neural network. *International Journal of Machine Tools and Manufacturing*, 47(2), 211-222.

Khraisheh, F., Farha, A., Khraisheh, M., (2008), An integrated approach to the Superplastic Forming of lightweight alloys: towards sustainable manufacturing. *International Journal Sustainable Manufacturing*, 1, 18-40.

Kleiner, M., Chatti, S., Klaus, A. (2006), Metal forming techniques for lightweight construction. *International Journal* of *Materials Processing Technology, Proceedings* of the 11th International Conference on Metal Forming 2006, 177(1-3), 2-7.

Kleiner, M., Geiger, M., Klaus, A., (2003), Manufacturing of Lightweight Components by Metal Forming. *CIRP Annals - Manufacturing Technology*, 52(2), 521-542.

Lassance, D., Fabrègue, D., Delannay, F., Pardoen, T., (2006) Modeling of damage mechanisms in AlMgSi alloys, Understanding the role of homogenization on the extrudability. Journal of Material Science, Belgium, 52, 22-32.

Lassance, D., (2006), Modeling of damage mechanisms in AlMgSi alloys Understanding the role of homogenization on the extrudability, *PHD Thesis*, F*ACULTE DES SCIENCES APPLIQUEES*.

Li, B., Lin, J., & Yao, X., (2002), A novel evolutionary algorithm for determining unified creep damage constitutive equations. *International Journal of Mechanical Sciences*, 44, 987-1002.

Li, C., Wan, M., Wu, X-D., Huang, L., (2010), Constitutive equations in creep of 7B04 aluminum alloys. *Materials Science and Engineering*, A 527(16-17), 3623-3629.

Lin, J., Cheong, B. H., Yao, X., (2002), Universal multi-objective function for optimizing superplastic- damage constitutive equations. *Journal of Materials Processing Technology*, 125-126, 199-205.

Lin, J., Liu, Y., Dean, T.A., (2005), A review on Damage Mechanisms, Models and Calibration Methods under Various Deformation Conditions. *International Journal of Damage Mechanics*, 14.

Lin, J., and Dean, T. A., (2003), Modeling of microstructure evolution in hot forming using unified constitutive equations. *Journal of Materials Processing Technology*, 143-144, 281-285.

Lin, J., and Dean, T. A., (2005), A set of unified constitutive equations for modeling microstructure evolution in hot deformation. *Journal of Materials Processing Technology*, 167(2-3), 354-362.

Liu, Y., and Lin, J., (2003), Modeling of microstructural evolution in multipass hot rolling. *Journal of Materials Processing Technology*, 143-144, 723-728.

Liu, Y., (2004), Characterisation of microstructure and damage evolution in hot deformation. *PHD thesis, Manufacturing and mechanical engineering. Birmingham, UK, The University of Birmingham*.

Miller, W. S., Zhuang, L., Bottema, J., Wittebrood, A. J., De Smet, P., Haszler, A., Vieregge, A., (2000), Recent development in aluminum alloys for the automotive industry. Journal of Materials Science and Engineering, 280(1), 37-49.

Mohamed, M., Foster, A. D., Lin, J., (2008), Solution heat treatment in HFQ process. *Steel Research International*, 79 (11), VII, 160-167.

Mohamed, S. M., (2003), An investigation of tube hydroforming process, Production Engineering Department. Cairo-Egypt, Helwan University,1-135.

Mrówka-Nowotnik, G., Sieniawski, J., Nowotnik, A., (2005), Influence of heat treatment on the microstructure and mechanical properties of 6005 and 6082 aluminum alloys. *Achievements in Materials and Manufacturing Engineering*, 20 (1-2), 447-450.

Mrówka-Nowotnik, G., (2008), Damage mechanism in AlSi1MgMn alloy. *Archives of Materials Science and Engineering*, 29 (2), 93-96.

Myhr, O. R., Grong, Ø., Andersen, S. J., (2001), Modeling of the age hardening behavior of Al-Mg-Si alloys. *Acta Materialia*, 49(1), 65-75.

Myhr, O. R., Grong, Ø., Andersen, S. J., Fjær, H. G., Marioara, C. D., (2004), Modeling of the microstructure and strength evolution in Al-Mg-Si alloys during multistage thermal processing. *Acta Materialia*, 52(17), 4997-5008.

Nicolaou, P. D., & Semiatin, S. L., (2000), An analysis of the effect of continuous nucleation and coalescence on cavitation during hot tension testing. *Acta Materialia*, 48, 3441-3450.

Nicolaou, P. D., & Semiatin, S. L., (2003), An experimental and theoretical investigation of the influence of stress state on cavitation during hot working. *Acta Materialia*, 51, 613-623.

NHTSA, (1990), Corporate Average Fuel Economy (C A F E). *www.nhtsa.dot.gov/cars/rules/cafe/index.htm*.

Pilling, J., & Ridley, N., (1986), Effect of hydrostatic pressure on cavitation in superplastic aluminium alloys. *Acta Metallurgica*, 34, 669-679.

Polmear, I.J., (1995), Light Alloys – Metallurgy of the Light Metals. Third ed, Butterworth–Heinemann, Oxford.

Poole, W.J., Saeter.S., Waterloo.G., (2000), A Model for Predicting the Effect of Deformation after Solution Treatment on the Subsequent Artificial Ageing Behavior of AA7030 and AA7108 Alloys. Metallurgical and Materials Transactions, A 31A, 2327-2338.

Prior, A. M. (1994), Applications of Implicit and Explicit Finite Element Techniques to Metal Forming. Journal of Materials Processing Technology, 45, 649-656.

Raj, R., Ashby, M. F., (1975), Intergranular fracture at elevated temperature, Original Research Article Acta Metallurgica, 23(6), 653-666

Ree, J. H., (2003), Grain boundary sliding and development of grain boundary openings in experimentally deformed octachloropropane, *Journal of Structural Geology*, 16 (3), 403-418.

RICE, J. R. & TRACEY, D. M. (1969) On the ductile enlargement of voids in triaxiality stress fields. J. Mech. Phys. Solids, 17, 201-217.

Richard K. Boger, M.S., (2006), Non-monotonic strain hardening and its constitutive representation. *Materials Science and Engineering*, Ohio, Ohio State University, *Degree Doctor of Philosophy*: 1-171.

Serra, D., (2009), Superplastic forming applications on AFERO engines, A review of ITP manufacturing processes. *EuroSPF08*, Carcassonne, France 1.

Shercliff, H. R., and Ashby, M. F., (1990), A process model for age hardening of aluminium alloys-II, The model. *Acta Metallurgica et Materialia*, 38(10), 1789-1802.

Smerd, R., Winkler, S., Salisbury, C., Worswick, M., Lloydb, D., and Finnb, M., (2005), High strain rate tensile testing of automotive aluminum alloy sheet. *International Journal of Impact Engineering*, 32, 541–560

Stearns, J., T. S. Srivatsan, et al. (2004), Modeling the mechanical response of an aluminum alloy automotive rim. *Materials Science and Engineering*, A 366(2), 262-268.

Sulaiman, A. S., (2005), Finite Element Modelling and Characterisation of Springback and Drawability in Aluminum-Based Alloy. Department of Metallurgy and Materials, Birmingham, University of Birmingham. *Degree Doctor of Philosophy*, 1-184.

Tauzer, P., (2006), Tube hydroforming for expanded design options. www.thefabricator.com.

Toros, S., Ozturk, F., Ilyas, K., (2008), Review of warm forming of aluminum-magnesium alloys. *Journal of Materials Processing Technology*, 207(1-3), 1-12.

Tvergaard, V. & Needleman, A. (2001), The modified Gurson model. IN LEMAITRE, J. (Ed.) Handbook of Materials Behavior Models. London, Academic Press.

www.autoaluminum.org. Development of Aluminum Application Technologies for Automotive Components.

www.app.eng.ubu.ac.th/~edocs/ f20061122Suriya104.pdf. Lecture 17: Heat treatable aluminum alloys, MMat380.

Wang, L., Strangwood, M., Balint, D., Lin, J., and Dean, T.A., (2010), Formability and failure mechanisms of AA2024 under hot forming conditions. *Materials Science & Engineering A*, (paper accepted).

Wilhelm, M. (1993), Materials used in automobile manufacture - current state and perspectives. *Journal of Physics*. IV France 03(C7), 31-40.

Zhu, Z., and Starink, M. J., (2008), Age hardening and softening in cold-rolled Al-Mg-Mn alloys with up to 0.4 wt% Cu. *Materials Science and Engineering*, A 489(1-2), 138-149.

Zhou, M., Dunne, F. P. E., (1996), Mechanisms-based constitutive equations for the superplastic behaviour of a titanium alloy. *Journal of strain analysis*, 31(3), 187-196.

Appendix 1. List of publications

Published

1- Mohamed, M.S., Foster, A.D., Lin, J., (2008) Solution heat treatment in HFQ process. *Steel Research International*, Vol. 79, No 11, VII, pp160-167. ISBN: 978-3-514-00754-3.

2- Mohamed, M., Foster, A.D., Lin. J., 2008, "An Investigation of Hot Forming Quenching (HFQ) process for 6xxx aluminium alloys", Proceedings of 9th international conference on production Engineering, Alexandria, Egypt. 1-7.

3- Foster, A., Mohamed, M., Lin, J., Dean, T., (2008) An investigation of lubrication and heat transfer for a sheet aluminum Heat, Form-Quench (HFQ) process. *Steel Research International*, 79 (11), VII, 133-140.

4- Mohamed M., Foster, A., Wang, L., Lin, J., Dean, T., (2010) Formability for Hot Stamping process of AA6082 Aluminium Alloys. *Steel Research International*, Vol. 81(9).

In Press

5- Mohamed, M.S., Foster, A.D., Lin, J., Dean, T. A., (2009) A set of unified viscoplastic damage constitutive equations for hot forming of AA6082. (In press).

6- Mohamed, M.S., Foster, A.D., Lin, J., Dean, T. A., (2009) Investigation of deformation and failure features in hot stamping of AA6082: Experimentation and Modelling. (In press).

7- Mohamed, M.S., Lin, J., Wang, L., (2010) Hybrid forming processes for the production of lightweight high-strength automotive panel parts. International heat treatment Journal (IHT186) (submitted).

8- Li, N., Mohamed, M.S., Lin, J., (2010) Experimental and numerical studies on the formability of materials in hot stamping and cold die quenching processes.